

HIROSHIMA UNIVERSITY

DOCTORAL THESIS

**Study on Energy Harvesting from Wave
and Flow Energy Using Triboelectric
Generator and Piezoelectric Generator**

Author:
Xinru DU

Supervisor:
Prof. Hidemi MUTSUDA

*A thesis submitted in fulfillment of the requirements
for the degree of Doctor of Philosophy*

in the

Transportation and Environmental Systems Program
Graduate School of Advanced Science and Engineering

January 18, 2024

Declaration of Authorship

I, Xinru DU, declare that this thesis titled, “Study on Energy Harvesting from Wave and Flow Energy Using Triboelectric Generator and Piezoelectric Generator” and the work presented in it are my own. I confirm that:

- This work was done wholly or mainly while in candidature for a research degree at this University.
- Where any part of this thesis has previously been submitted for a degree or any other qualification at this University or any other institution, this has been clearly stated.
- Where I have consulted the published work of others, this is always clearly attributed.
- Where I have quoted from the work of others, the source is always given. With the exception of such quotations, this thesis is entirely my own work.
- I have acknowledged all main sources of help.
- Where the thesis is based on work done by myself jointly with others, I have made clear exactly what was done by others and what I have contributed myself.

Signed:

Date:

Abstract

The energy crisis has a significant impact on the economy, politics, and environment of both developed and developing countries. Therefore, utilization of renewable energy is one of the most promising methods to deal with the energy crisis. Considering the reliable, robust, and desirable characteristics of ocean energy, utilizing of it is one promising method. Among it, ocean wave and flow energy are ubiquitous. The aim of the thesis is to propose suitable wave and flow energy harvesting devices for isolated islands, sensors on fish aggregating device (FAD), and wave information monitoring for various weather environment and low-frequency wave conditions. This means structure of devices based on piezoelectric nanogenerators (PENGs)/triboelectric nanogenerators (TENGs), which are suitable medium for energy harvesting, should be designed to perform both sensing wave parameters and powering other sensors. To test and improve the efficiency of wave energy harvesting based on PENGs/TENGs, indoor and real-sea test experiments for optimization should be conducted and complete experimental process of optimization should be clarified. Simultaneously, when coupling wave with devices in numerical simulation, traditional grid methods often suffer from distortions due to the large motion. Therefore, suitable numerical algorithm needs to be selected to meet the challenges of the fluid-structure interaction. These can help us to predict the power generation of the developed devices. For flow energy harvesting with PENGs/TENGs, there are few numerical algorithms and mechanism about exploring the turbulent energy and flow control with local polymer coating. At the same time, previous numerical algorithms always choose the DNS method, demanding high spatial and temporal resolution. This approach proves computationally intensive, time-consuming, and heavily reliant on computer memory. Therefore, alternatives are needed when dealing with high Reynolds cases.

In the Chapter 2, to facilitate continuous and stable energy supply based on PENGs/TENGs for both FAD equipment and islands, we design a flexible piezoelectric device (FPED) based on PENGs used for ocean energy harvesting. Our approach involves the development of FPEDs coated with piezoelectric paint spray technology. Simultaneously, hemi-spherically spring origami triboelectric nanogenerators (HSO-TENGs) designed for self-powered ocean wave monitoring are developed based on TENGs technology.

In the Chapter 3, FPEDs are attached to the frame of a FAD to assess their performance characteristics in varying submerged depths and support types. Through examination under various wave conditions, we've identified the key parameters significantly impacting electrical performance. The maximum output voltage can be increased obviously with cantilever support, fully submerged depths, thickness 50 μm , and aspect ratio 1:2. Utilizing the experimental setup as a basis, we construct a theoretical model and further refine a computational model employing the immersed boundary method to analyze FPED-wave interactions. The latter is found to be a better predictor of power generation from FPEDs than the former. In addition, a field test conducted in real sea conditions, supported by a remote data monitoring system for the painted FPEDs, demonstrate exceptional performance even under extreme bending, weathering, and fatigue.

In the Chapter 4, HSO-TENGs are designed for self-powered ocean wave monitoring, driven by two optimization approaches. (1) Swing machine experiments are employed to assess the HSO-TENGs' monitoring capabilities concerning wave height and period, showing satisfactory accuracy. Three structural parameters, the weight of magnet mass, the height of the hammer, and the length of the external

swing arm, are found to increase average voltage generation by 33%, 62%, and 50%. (2) Numerical simulations utilizing the smoothed particle hydrodynamics (SPH) method can find the most suitable fixed condition for HSO-TENGs to effectively sense wave changes. Then, no-submergence that can fully compress and stretch SO-TENGs is selected from three fixed conditions. Subsequent wave tank experiments aim to evaluate their proficiency in detecting wave height, period, frequency, and direction. The maximum voltage can reach 15v. When the four spring origami triboelectric nanogenerators (SO-TENGs) are connected in parallel, the output voltage can supply the temperature and humidity sensor continually. Finally, we investigate the HSO-TENG's ability to monitor wave direction and spreading parameters through numerical SPH circular wave tank simulations. And the SPH method is found to simulate the motion of HSO-TENG and similar energy harvesting devices in waves well, thereby guiding device design and predicting device performance.

In the Chapter 5, we develop a novel numerical model to control turbulent flow filed and drag reduction performance with polymer coating. This model merges mesoscopic methods with computational fluid dynamics (CFD) techniques, addressing the underexplored area of non-uniform polymer drag reduction in external flows. This model integrates direct numerical simulation (DNS) and large eddy simulation (LES) methods within the CFD framework. Both of them are in good agreement with the previous reference results, which proves the reliability of the model. Our approach initially couples the mesoscopic dissipative particle dynamics (DPD) method with DNS and LES methods, validating the results through the finitely extensible nonlinear elastic approach. Subsequently, we utilize the model to discuss the impact of varying polymer region heights on non-uniform polymer drag reduction. Particularly noteworthy is the efficiency highlighted by the LES method, offering computational efficiency, especially at higher Reynolds numbers. Then, the mean velocity, the root-mean-square velocity fluctuations and the Reynolds shear stress presents a monotonous trend to the particle energy density. Furthermore, releasing polymer particles close to the wall is also found to achieve drag reduction, and the drag reduction efficiency of releasing polymer particles in half of the region is very high. The new vortex grows again above the polymer region. Our model illuminates that significant polymer drag reduction efficiency persists even when the polymer region doesn't span the entire fluid area, as observed in conditions like the application of polymer coatings. And high energy dissipation gradually changes from dispersion to concentration during the process of the drag reduction. Lastly, for different Reynolds numbers, the model can be widely used and has a good prospect.

Contents

| | |
|---------------------------------------------------------------------------------------|------------|
| Declaration of Authorship | iii |
| Abstract | v |
| 1 Introduction | 1 |
| 1.1 Background | 1 |
| 1.1.1 Methods to deal with the energy crisis | 1 |
| 1.1.2 Utilization of ocean energy | 3 |
| 1.1.3 Previous ocean energy harvesting technologies | 5 |
| 1.1.4 Research on turbulent energy around the ocean applications | 10 |
| 1.1.5 Previous studies on numerical method | 13 |
| 1.2 Motivation | 14 |
| 1.3 Thesis Overview | 14 |
| 2 Development of ocean energy harvesting device | 17 |
| 2.1 Overview of piezoelectric-painted-based ocean energy harvester | 17 |
| 2.2 Structure design of hemi-spherically spring origami triboelectric nano-generators | 20 |
| 3 Working parameter selections of FPED | 23 |
| 3.1 Experimental work | 23 |
| 3.2 Theoretical model | 24 |
| 3.3 Computational model | 26 |
| 3.3.1 Overview of IBM | 26 |
| 3.3.2 Governing equations for IBM-based computational model | 27 |
| 3.3.3 Initial and boundary conditions | 29 |
| 3.4 Results and discussion | 29 |
| 3.4.1 Validation of theoretical and computational models | 29 |
| 3.4.2 Effect of the support type and submerged depth | 33 |
| 3.4.3 Effect of the paint thickness and AR of the painted FPED | 33 |
| 3.5 Preliminary field test | 37 |
| 3.6 Conclusions | 42 |
| 4 Experimental and numerical optimization of HSO-TENGs | 47 |
| 4.1 Structure Optimization | 47 |
| 4.1.1 Experiment setup of swinging experiment | 47 |
| 4.1.2 Results and discussion | 47 |
| 4.2 Performance of HSO-TENG in uni-direction wave tank | 50 |
| 4.2.1 Experiment setup of uni-direction wave tank | 50 |
| 4.2.2 Numerical conditions in uni-direction wave tank based on SPH method | 53 |
| 4.2.3 Selection of fixed conditions based on numerical model | 56 |
| 4.2.4 Validation of numerical model | 56 |

| | | |
|----------|----------------------------------------------------------------------------------------------------------------|------------|
| 4.2.5 | Experimental results and discussion | 58 |
| 4.3 | Numerical simulation in mul-direction circular wave tank | 59 |
| 4.3.1 | Introduction of numerical mul-direction circular wave tank | 59 |
| 4.3.2 | Numerical results in sensing wave directions and parameters | 59 |
| 4.4 | Conclusions | 66 |
| 5 | Numerical study on drag reduction and turbulence energy based on polymer coating | 67 |
| 5.1 | Numerical method based on DNS/LES-DPD | 67 |
| 5.1.1 | Governing equations | 67 |
| | DNS method | 67 |
| | LES method | 68 |
| | DPD method | 68 |
| 5.1.2 | Coupling method | 69 |
| | Re-transformation between two parts | 69 |
| | Shear velocity transformation between two parts | 70 |
| 5.1.3 | Numerical algorithm | 72 |
| 5.2 | Results and discussion | 74 |
| 5.2.1 | Numerical domain and initial condition | 74 |
| 5.2.2 | Validation and comparison | 76 |
| 5.2.3 | Effect of Reynolds number | 81 |
| 5.2.4 | Effect of polymer layer | 83 |
| 5.2.5 | Estimation and harvesting of turbulent energy | 85 |
| 5.3 | Conclusions | 93 |
| 6 | Conclusions and future works | 97 |
| 6.1 | Conclusions | 97 |
| 6.1.1 | Experimental and numerical research about the selection of working parameter of FPED attached to FAD | 97 |
| 6.1.2 | Experimental and numerical studies on the optimization of HSO-TENGs | 98 |
| 6.1.3 | Numerical study on drag reduction and turbulence energy based on polymer coating | 98 |
| 6.2 | Recommended future work | 99 |
| | Bibliography | 101 |
| | Acknowledgements | 109 |

List of Figures

| | | |
|------|-------------------------------------------------------------------------------------------------------------------------------------------------------------------------------------------------------------------------------------------------------------------------------------------------------------------------|----|
| 1.1 | World energy consumption from 1990 to 2040 (Conti et al., 2016) | 2 |
| 1.2 | Spatial distributions during 1979-2020 of averaged total (A) Yearly-averaged significant wave height (m), (B) wave energy period (s), and (C) wave power (kW/m) fields. (Cao et al., 2022) | 4 |
| 1.3 | The working process of PENG to harvest ocean energy (Liu et al., 2023) | 5 |
| 1.4 | Working principle of direct coupling PENG (Baghbani Kordmahale et al., 2021). | 6 |
| 1.5 | Working principle of frequency-increasing PENG (Chen et al., 2021). . | 6 |
| 1.6 | Working principle of fluid-induced vibration PENG (Zhao et al., 2021). | 6 |
| 1.7 | Working principle of multi-mechanism PENG (Qi et al., 2021). | 7 |
| 1.8 | The research topics, sub-topics, and their relationship of TENG research (Song et al., 2022) | 8 |
| 1.9 | Liquid-solid contact TENG using Nanostructured Hydrophobic Thin-Film Surface (Zhu et al., 2014). | 8 |
| 1.10 | Liquid-solid contact TENG using a networked integrated triboelectric nanogenerator (Zhao et al., 2018). | 9 |
| 1.11 | Fully enclosed TENGs with spherical structure (Cheng et al., 2019). . . | 9 |
| 1.12 | Fully enclosed TENGs with spring-assisted structure (Liang et al., 2021). | 10 |
| 1.13 | Fully enclosed TENGs with multilayer structure (Liu et al., 2021). . . . | 11 |
| 1.14 | The schematic diagram of Waterbomb-origami-inspired TENGs (Pang et al., 2022). | 11 |
| 1.15 | The schematic diagram of elastic origami-structured TENGs harvesting wave energy (Tao et al., 2020b). | 12 |
| 1.16 | The schematic diagram of elastic origami-structured TENGs monitoring bridge health (Xia et al., 2023). | 12 |
| 2.1 | Illustration of the spray coating technique implemented for the painted FPED; The piezoelectric paint ejecting from the nozzle can be covered on the electrode with the substrate | 18 |
| 2.2 | A unimorph type of the laminated structure of the painted FPED; The piezoelectric paint area is put between the upper electrode and the bottom one covered by the waterproof coating. | 18 |
| 2.3 | One example of an electric circuit for the painted FPED with the resistance. | 18 |
| 2.4 | Overview of the FAD in real sea condition and an ocean energy harvester using the painted FPED attached to the FAD. The painted FPED can be vertically and horizontally set on the FAD metal frame near the sea surface; Several painted FPEDs with different AR and thickness are installed in the field test. | 19 |
| 2.5 | Schematic diagram of HSO-TENG array in ocean and the distribution of components in one disassembled HSO-TENG. | 20 |
| 2.6 | Schematic diagram of the preparation process of the SO-TENG. | 20 |

| | | |
|------|---------------------------------------------------------------------------------------------------------------------------------------------------------------------------------------------------------------------------------------------------------------------------------------------------------------------------------------------------------------------------------------|----|
| 2.7 | The structure and working mechanism of the rotatable hammer. | 21 |
| 2.8 | The working mechanism, charge distribution map and fabrication of the SO-TENG. (The width and the length of the strips is 7.5cm and 100cm. The basis weight of paper is 104g/m ² , the thickness of PVC is 0.25mm, the thickness of aluminum tape is 0.08mm, and the thickness of PTFE is 0.1mm.They are connected with double-sided tape with a width of 15mm.) | 21 |
| 3.1 | Experimental setup in a towing tank. The painted FPED is positioned near the water surface at the centre of the tank. Regular waves are generated by the wave paddle on the upstream side, and the absorbing beach is set on the downstream side of the tank. | 23 |
| 3.2 | Several support types for painted FPED, with different submerged depths. The support type was selected considering practical applications under real sea conditions. The painted FPED can be fixed by cantilever support or both-end-support. SWL: standing water level. d : the distance between the SWL and the underwater end. | 24 |
| 3.3 | Example of the measured output voltage of the painted FPED. The maximum and average output data are calculated from the measured raw data; Fast Fourier transform (FFT) is employed to determine the peak value and dominant frequency. | 25 |
| 3.4 | Parameter settings for a unimorph-type painted FPED in the theoretical model. The painted FPED can be deformed by external forces, such as waves and currents; This model is based on the prototype of the painted FPED shown in Fig. 2.2 and 2.4. The second element (x_2) indicates the piezoelectric paint area. | 25 |
| 3.5 | Model of immersed boundary method. The red Lagrangian points: the boundaries of solids. The surrounding black Euler grids: fluids. The left figure is the 2D side view of the computational model and the right one is the corresponding 3D view | 27 |
| 3.6 | Schematic of the immersed boundary method | 29 |
| 3.7 | Effect of wave crests and troughs on the motion of FPEDs fixed by vertical cantilever support. Comp. is the computational result. Exp. is the experimental result | 30 |
| 3.8 | Effect of wave height on the motion of FPEDs fixed by vertical cantilever support | 31 |
| 3.9 | Effect of wave period on the motion of FPEDs fixed by vertical cantilever support | 32 |
| 3.10 | Time history of output voltage due to the motion of FPED 1 over 10 s under wave conditions with difference steepness. | 32 |
| 3.11 | Comparison between computational, theoretical and experimental voltage per square meter. The red circle: the experimental results. The blue asterisks: the results of the IBM-based computational model. The green dots: the results of the theoretical models. The lines: the corresponding univariate linear regression lines. | 34 |
| 3.12 | Relationship between the type of support for the painted FPED and the maximum output voltage. The three different support types, cantilever, both-end-support and horizontal setting, are compared for FPED1, 2, and 3. H/λ is the wave height normalised by the wave period, λ | 35 |

| | | |
|------|-------------------------------------------------------------------------------------------------------------------------------------------------------------------------------------------------------------------------------------------------------------------------------------------------------------------------------------------------------------------------------------------|----|
| 3.13 | Relationship between the submerged depth of the painted FPED and the maximum output voltage. d/L indicates the submerged depth, d normalized by the length, L of the painted FPED. | 36 |
| 3.14 | Relationship between paint thickness, t_2 (the value shown in figure 3) of the painted FPED and maximum output voltage. The output voltage at the same AR is compared between FPEDs 1 and 4, 2 and 5, 3 and 6. | 38 |
| 3.15 | Relationship between the AR of the painted FPED and maximum output voltage. The support type is a vertical setting with full- and half-submerged depth. | 39 |
| 3.16 | Location of the field test: 30 m water depth, 2 km offshore, off of the northern part of Okinawa Island, Japan. The output voltage of the painted FPED is recorded by a remote data monitoring system consisting of the data logger (A/D converter) some WiFi access devices and a battery. The remote operation station is located on land, 20 km away from the field test site. | 40 |
| 3.17 | Dominant frequency of flow velocity due to waves determined by FFT. The velocity (m/s) was measured using a current metre in the field test. The flow direction is divided into north-south and east-west components. | 41 |
| 3.18 | Average output voltage measured by the remote data monitoring system. The measuring time was 5 min with a sampling frequency of 1.0 Hz for the raw output voltage. The time interval was set to 30 min. The period of the field test was two days considering the restriction of the remote system. | 42 |
| 3.19 | Dominant frequency of the output voltage due to waves, analyzed by FFT. | 43 |
| 3.20 | Relationship between the average output voltage and acceleration caused by the motion of the painted FPED. A acceleration was calculated using the instantaneous output voltage due to each wave. | 44 |
| 3.21 | Comparison of the estimated power of the painted FPED based on the measured data in the field test | 45 |
| 4.1 | Swinging experimental setup, flow chart(i) and three Snapshots during experiments(ii-iv). | 48 |
| 4.2 | Schematic of Parameters selected for optimization.(The SO-TENGs, Part C and Part D, are positioned along the direction of swing) | 48 |
| 4.3 | Output voltage versus time curve under different swinging frequencies. | 49 |
| 4.4 | Absolute average voltage versus frequencies under varying maximum swing angles. | 49 |
| 4.5 | Absolute average voltage versus frequencies under varying lengths of swing arm. | 50 |
| 4.6 | Absolute average voltage versus frequencies under varying weights of magnet mass. | 51 |
| 4.7 | Absolute average voltage versus frequencies under varying heights of the hammer. | 51 |
| 4.8 | Charging curves using different capacitances. | 52 |
| 4.9 | Overview of experimental uni-direction wave tank. | 52 |
| 4.10 | The connection part between the device and the support shelf. | 53 |

| | | |
|------|------------------------------------------------------------------------------------------------------------------------------------------------------------------------------------------------------------------------------------------------------------------------------------------------------------------------------------------------------------------------------------------------------------------------------------------------------------------------------------------------------------------------------------------------------------------------------------------------------------------|----|
| 4.11 | Illustration of four parts in one HSO-TENG device and its working details in wave tank. (Part C and D stretch and compress along the direction of the wave while Part A and B move perpendicular to the direction of the wave). | 54 |
| 4.12 | Top view and side view of numerical wave tank (including flap-type generator, water domain and damping zone). | 54 |
| 4.13 | Bird view of numerical wave tank and side view of the HSO-TENG. | 55 |
| 4.14 | Comparison between the motions of the HSO-TENG and the change in length(Δl) of the springs under the three fixed conditions.(Non-submergence: the bottom of the hemisphere is flush with the horizontal level and the whole device can rotate around the fixed bottom of the cylinder. Half-submergence: half of the hemisphere is submerged in water and the whole device can rotate around the fixed bottom of the cylinder. Mooring-connection: the bottom of the hemisphere is flush with the horizontal level and its bottom is connected to the bottom of the wave tank through mooring. | 55 |
| 4.15 | Validation points in experiment. | 57 |
| 4.16 | Validation points in numerical simulation. | 57 |
| 4.17 | Comparison between the experimental and numerical moving distance of HSO-TENG. | 57 |
| 4.18 | The relationship between numerical average changes in length and experimental average voltage(U : experimental average voltage (v), Δl : numerical average changes in Length (m)). | 58 |
| 4.19 | Four stages of output voltage and motion of HSO-TENG in one experimental wave period. | 59 |
| 4.20 | The relationships between the voltage domain frequency and wave frequencies. | 60 |
| 4.21 | The relationships between the voltage domain frequency and wave periods. | 60 |
| 4.22 | The average absolute voltage under different wave heights. | 61 |
| 4.23 | The average maximum voltage under different wave heights. | 61 |
| 4.24 | The test of supplying the temperature and humidity sensor continuously(The power of the sensor is 0.15mW). | 62 |
| 4.25 | Overview of Numerical circular wave tank and the HSO-TENG. | 63 |
| 4.26 | The voltage of HSO-TENG in circular wave tank. (i)Numerical simulation of HSO-TENG in circular wave tank and the voltage with four spreading parameters: $s=5,10,25$ and ∞ (mean wave direction angle= 0°). (ii)Numerical simulation of HSO-TENG in circular wave tank and the voltage with four mean wave direction angles: Angle= $0^\circ,15^\circ,30^\circ$ and 45° (spreading parameter= 5). | 64 |
| 4.27 | The predicted average voltage of the four SO-TENG parts. (i)The predicted average voltage of the four SO-TENG parts under different spreading parameters. (ii)The predicted average voltage of the four SO-TENG parts under different mean wave direction angles. | 65 |
| 5.1 | Schematic of the transformation from the DPD Reynolds number to the DNS/LES value | 71 |
| 5.2 | Schematic of the transformation from the DNS/LES shear velocity to the DPD one | 71 |
| 5.3 | Schematic of the DNS/LES-DPD model | 73 |
| 5.4 | Schematic of the numerical domain | 73 |

| | | |
|------|----------------------------------------------------------------------------------------------------------------------------------------------------------------------------------------------------------------------------------------------------------------------------------------------------------------------------------------------------------------------------------------------------------------------------------------------------------------------------------------------------------------------------------------------------------------------------|----|
| 5.5 | Comparison between results with $Re_\tau=180$ using DNS/LES method in this study with the reference (Moser, Kim, and Mansour, 1999)(DNS) | 78 |
| 5.6 | Comparison between results with $Re_\tau=395$ using DNS/LES method in this study with the reference (Moser, Kim, and Mansour, 1999)(DNS) | 79 |
| 5.7 | Comparison between results with $Re_\tau=590$ using DNS/LES method in this study with the reference (Moser, Kim, and Mansour, 1999)(DNS) | 80 |
| 5.8 | Comparison between Cases 1 and 7's profiles in wall coordinates of the streamwise mean velocity. Open blue circle: the polymer solution using LES-DPD method in the lower region of Case 1. Open red square: the polymer solution using DNS-DPD method in the lower region of Case 7. Solid black dot: the Newtonian fluid using LES method in the upper region of Case 1. Black asterisk: the Newtonian fluid using DNS method in the upper region of Case 7. | 81 |
| 5.9 | Comparison between the curves for Cases 1 and 7 in wall coordinates. Open blue circle: the polymer solution using LES-DPD method in the lower region of Case 1. Open red square: the polymer solution using DNS-DPD method in the lower region of Case 7. Solid black dot: the Newtonian fluid using LES method in the upper region of Case 1. Black asterisk: the Newtonian fluid using DNS method in the upper region of Case 7. | 82 |
| 5.10 | Comparison between Cases 1, 2 and 3's profiles of the streamwise mean velocity. Open blue circle: the polymer solution using LES-DPD method in the lower region of Case 1. Open red square: the polymer solution using LES-DPD method in the lower region of Case 2. Open green star: the polymer solution using LES-DPD method in the lower region of Case 3. Solid black dot: the Newtonian fluid using LES method in the upper region of Cases 1, 2 and 3. Details about Case N2, A and B can be seen in Table 5.4 and (Dallas, Vassilicos, and Hewitt, 2010) | 83 |
| 5.11 | Comparison of turbulent intensity and Reynolds stress among Case 1, 2 and 3. Open blue circle: the polymer solution using LES-DPD method in the lower region of Case 1. Open red square: the polymer solution using LES-DPD method in the lower region of Case 2. Open green star: the polymer solution using LES-DPD method in the lower region of Case 3. Solid black dot: the Newtonian fluid using LES method in the upper region of Case 1, 2 and 3. Details about Case N2, A and B can be seen in Table 5.4 and (Dallas, Vassilicos, and Hewitt, 2010) | 84 |
| 5.12 | Comparison of streamwise mean velocity in wall coordinates for Cases 2, 8 and 9. Open circle: the polymer solution with $Re_\tau=180$. Open square: the polymer solution with $Re_\tau=395$. Open diamond: the polymer solution with $Re_\tau=590$. Solid dot: Newtonian fluid using LES method in the upper region of Case 9. Dotted line: Linear viscous relation and logarithmic overlap layer. 'b' of cases 2, 8 and 9 is 4.8, 5.1 and 5.7, separately. | 85 |
| 5.13 | Q-criterion for vortex visualisation at different Reynolds numbers using LES-DPD | 86 |
| 5.14 | Q-criterion for vortex visualisation at different Reynolds numbers using LES | 87 |
| 5.15 | Distribution of DPD particles in Cases 4, 5 and 6 | 88 |

| | | |
|------|-----------------------------------------------------------------------------------------------------------------------------------------------------------------------------------------------|----|
| 5.16 | Comparison of the vertical distribution of streamwise mean velocity in wall coordinates in Cases 4, 5 and 6 | 89 |
| 5.17 | Comparison of RMS and Reynolds shear stress in Cases 4, 5 and 6 | 89 |
| 5.18 | Vortex of the Q criterion using the DNS-DPD method | 90 |
| 5.19 | Vortex of the Q criterion using the DNS method | 91 |
| 5.20 | Comparison of turbulence production and dissipation in Cases 4, 5, and 6 | 92 |
| 5.21 | Flow visualization of turbulent energy harvesting using a PENG (Goushcha et al., 2015). | 93 |
| 5.22 | Vortex of the Q criterion and turbulence dissipation using the DNS-DPD method. Red isosurface: the vortex ($Q=10$). Blue isosurface: turbulence dissipation ($\epsilon_t^+=0.3$). | 94 |
| 5.23 | Vortex of the Q criterion and turbulence dissipation using the DNS method. Red isosurface: the vortex ($Q=10$). Blue isosurface: turbulence dissipation ($\epsilon_t^+=0.3$). | 95 |

List of Tables

| | | |
|-----|-------------------------------------------------------------------------------------------------------------------------------------------------------------------------------------------------------------------------------------------------------------------------------------------------------------------------------------------------------------------------------------------------------------------------------------------------------------------------------------------------------------------------------------------------------------------------------------------------------------------------------------------------------------------------|----|
| 2.1 | Specifications of the painted FPEDs. The parameters correspond to those shown in Fig.2.2 | 19 |
| 4.1 | Parameters of the wave tank in the experiment | 53 |
| 4.2 | Setting parameters of the numerical uni-direction wave tank. | 56 |
| 4.3 | Setting parameters of the numerical mul-direction circular wave tank | 62 |
| 5.1 | Parameters of the nine cases in the lower region. Here H_{DPD} is the height of the DPD particles' region shown in Fig. 5.4, Re_b is the bulk Reynolds number based on the mean bulk velocity, Re_τ is the friction Reynolds number, Den is a particle density parameter calculated by Eq[5.28], and $DR(\%)$ is the rate of drag reduction calculated by Eq[5.29] | 75 |
| 5.2 | Parameters of the nine cases in the upper region. Here H_{DPD} is the height of the DPD particle region shown in Fig. 5.4, Re_b is the bulk Reynolds number based on the mean bulk velocity, Re_τ is the friction Reynolds number, Den is a particle density parameter calculated by Eq[5.28], and $DR(\%)$ is the rate of drag reduction calculated by Eq[5.29] | 75 |
| 5.3 | Characteristics of the grids in the current study and related literature. Re_τ is the friction Reynolds number, δ is the half height of the simulation domain, L_x, L_z, L_y are the length of the domain in the streamwise, spanwise, and wall-normal directions, respectively. $N_x, N_z,$ and N_y are the grid number in the streamwise, spanwise, and wall-normal directions, respectively. Notably, the grids in the x and z directions are uniformly distributed, but the grids in the y direction are exponentially distributed from dense to sparse from the wall outward. More details can be found in (Vuorinen and Keskinen, 2016) | 76 |
| 5.4 | Parameters for the cases using FENE method from reference (Dallas, Vassilicos, and Hewitt, 2010). Here, Re_τ is the friction Reynolds number, We_c is the Weissenberg number, We_{τ_0} is the friction Weissenberg number, and $DR(\%)$ is calculated by Eq[5.29] | 77 |

Chapter 1

Introduction

1.1 Background

The term "energy crisis" has been ingrained in the public consciousness as early as 1970 (Pimentel et al., 1973; Nef, 1977). From the long-term aspects, the global campaign to reduce carbon emission, the growing population and the gradual depletion of non-renewable energy are all the root causes of the energy crisis (Coyle and Simmons, 2014; Awan and Khan, 2014). Notably, from 2021 to 2023, the new global energy crisis was exacerbated due to are short-term reasons such as COVID-19, war, and international policy (Fazelianov, 2022; Von Homeyer, Oberthür, and Dupont, 2022; Ozili and Ozen, 2023).

In turn, the energy crisis has a significant impact on the economy, politics, and environment of both developed and developing countries. In economical aspect, a surge in energy prices affects the industries reliant on energy and further leads to inflation. The reduced production and defunct companies resulted in high energy cost also leads to unemployment and decreased economic output (Richardson, 1975). In political aspect, international relations are impacted while countries compete for limited resources or negotiate trade deals to secure energy supplies. For nations heavily reliant on energy exports, this could threaten political stability if revenues decline sharply (Turner, 1974). In environmental aspect, a shift towards using more polluting or less sustainable energy sources to meet immediate demands may happen, which can lead to environmental degradation and habitat destruction (Sthel, Tostes, and Tavares, 2013). With the development of the discussion and exploration, these impacts have made more and more energy consumers aware of the necessity of energy transformation and the responsibilities they must take in energy consumption (Gârdan et al., 2023).

1.1.1 Methods to deal with the energy crisis

The recent strategies of dealing with the energy crisis is summarized based on previous researches (Farghali et al., 2023). Among them, utilization of renewable energy is one of the most promising methods. From the report of International Energy Agency (IEA) 2022c, the renewable energy only accounts for 5.21% of total energy supply (Browser, 2022). However, more and more nations are adopting policies to increase this share to achieve long-term sustainable solutions (Pietrosemoli and Rodrguez-Monroy, 2019; Omer, 2012). This bodes well for the potential of renewable energy. Fig. 1.1 shows the booming trend in renewable energy development from 1990 to 2040, the output of which is estimated to reach 29.2% of global electrical power at 2040 (Conti et al., 2016).

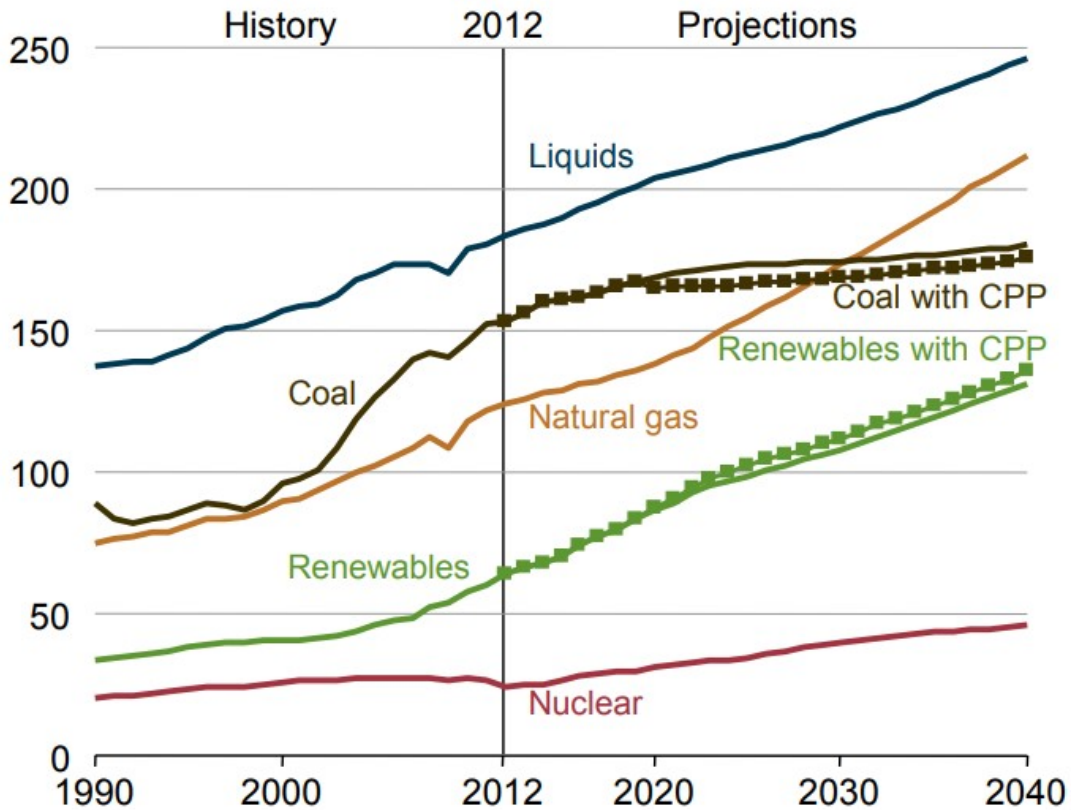


FIGURE 1.1: World energy consumption from 1990 to 2040 (Conti et al., 2016)

Among them, ocean wave are ubiquitous and changing all the time, making them very suitable as media for energy harvesting. For example, the residents of islands face challenges like fuel shortages and environmental pollution, pushing them to seek local renewable energy sources for sustainable electricity. Fortunately, many islands are rich in renewable energy resources, presenting many opportunities for development and utilization (Kuang et al., 2016). Especially, ocean energy stands out as a crucial and highly promising renewable energy source, uniquely resilient against the performance decline caused by sea salt particles. Unlike solar and wind energy, it isn't contingent on specific radiation and sea wind speeds to operate effectively. Therefore, ocean energy research is extremely promising.

Another fluid energy that holds great promise for harvesting is the turbulent energy around vehicles. According to reports, transportation constitutes 26.18% of total energy consumption, primarily through fossil fuel combustion in vehicles, accounting for over 33% of CO₂ emissions and 26% of all greenhouse gas emissions according to the United States Environmental Protection Agency (U.Epa, 2020). Within transportation, the marine industry accounts for 95% of global goods transportation (J. Carlton and Anderson, 2013). During vessel movement, aquatic resistance significantly impacts energy consumption, contributing to 85% of the total consumption (Ahmadzadehtalatapeh and Mousavi, 2015). Previous studies extensively detail how reducing frictional drag can drastically save fuel in ship propulsion systems (Ahmadzadehtalatapeh and Mousavi, 2015; Yang et al., 2014; Wang, Wang, and Liu, 2022; Zhao and Zong, 2022). Lowering resistance encountered by vessels in water diminishes the energy needed to maintain desired speeds and concurrently enhances the efficiency and responsiveness of hydraulic systems. This becomes particularly

vital given escalating fuel costs and environmental apprehensions surrounding its combustion. Numerous studies have concentrated on drag reduction (*DR*) across various ocean applications, spanning from marine vessels (Yang et al., 2014; Wang, Wang, and Liu, 2022; Zhao and Zong, 2022) to submarine pipelines (de Leeuw et al., 2022; Gu et al., 2014) and submarines. Those mean the promising value of research on reduction of transportation consumption and harvesting turbulent energy to energy crisis. In this study, both aspects of utilization of ocean wave and flow energy are discussed.

1.1.2 Utilization of ocean energy

The slow progression in harnessing ocean energy can be attributed to ongoing developmental stages in ocean energy technologies. Ocean energy, characterized by its broad spectrum and varying energy scales across time and space, presents challenges in integrating devices into large-scale ocean energy farms. Additionally, several hurdles, including effectiveness, reliability, competitiveness, costs, and environmental sustainability, hinder the sector's advancement towards commercial viability (Andres et al., 2017).

Furthermore, owing to the immense value of oceans in ecosystems, energy resources, and societal aspects, coastal regions often meet intense human activities and high population density (Ramos and Rouboa, 2022; Small and Nicholls, 2003; McGranahan, Balk, and Anderson, 2007; Neumann et al., 2015). Hence, there's a pressing need to establish reliable, sustainable, and environmentally friendly monitoring sensors capable of tracking marine disasters (e.g., high-speed winds, waves, storm surges, flooding, and tsunamis) and pollution indicators (e.g., temperature, pH, salinity, eutrophication, metals) (Soleimani, Ketabdari, and Khorasani, 2015; Bergsma et al., 2022). These devices are typically designed to monitor multiple ocean parameters, prioritize ease of production, ensure low energy consumption, and maintain stable power generation (Xu et al., 2019; Cao et al., 2021; Cao et al., 2023).

According to the IEA, five distinct technologies enable ocean power generation, including tidal rise and fall (barrages), tidal/ocean currents, waves, temperature gradients and salinity gradients (Biol, 2017). Among these, wave energy have garnered greater attention due to its wide distribution and no limitation by time and space. Fig. 1.2 shows global wave height, wave energy periods and wave power fields. The tendency that wave is becoming stronger has been proved because of global warming, which demonstrates the potential value of wave energy (Reguero, Losada, and Méndez, 2019).

Compared with the other methods for ocean power generation, the output of wave energy devices remains unpredictable, which brings challenges for energy utilization. Considering these effects, future research on wave energy devices should not solely emphasize the quantity of power generated but also focus on understanding the fluctuations and forecasting of electrical output. There are now a variety of wave prediction techniques (Lai et al., 2020; Wang et al., 2019). Hence, this study places emphasis on devices that can both harness energy and monitor sea parameters based on wave energy. Experimental optimization and numerical estimation to build the relationship between wave and devices become crucial in this pursuit.

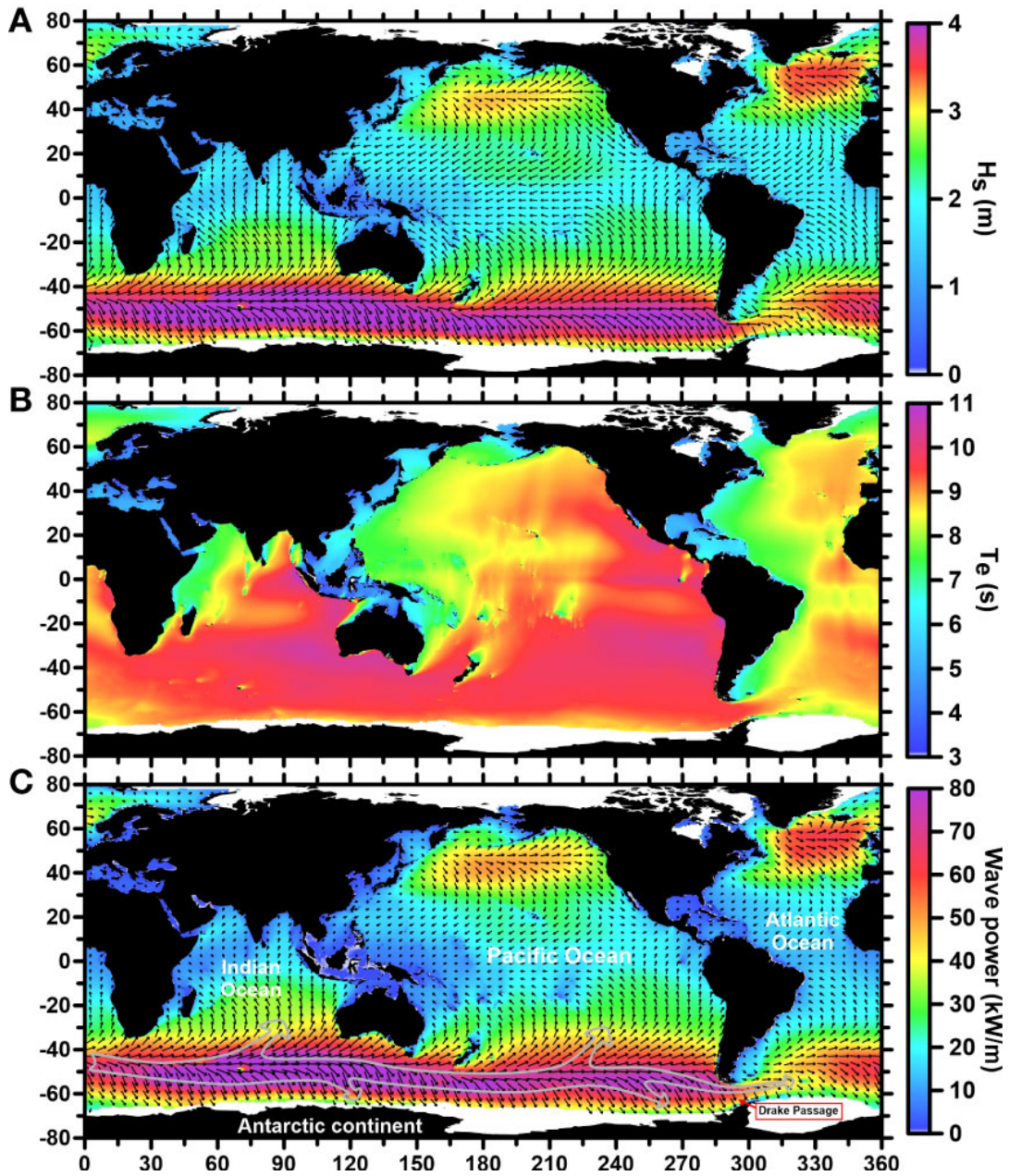


FIGURE 1.2: Spatial distributions during 1979-2020 of averaged total (A) Yearly-averaged significant wave height (m), (B) wave energy period (s), and (C) wave power (kW/m) fields. (Cao et al., 2022)

1.1.3 Previous ocean energy harvesting technologies

Recently, there has been significant development in ocean energy harvesting technologies utilizing specialized materials. The size-density dynamics of these systems stand out as crucial factors in current ocean energy technology. Among these innovations, the Piezoelectric Nanogenerator (PENG) emerges as a choice solution. Nabavi et al. introduced a novel low-volume piezoelectric beam-column energy harvesting system, leveraging breaking force (Nabavi et al., 2019). Similarly, Wu et al. presented a straightforward piezoelectric spring design based on an ordinary binder clip structure. Their harvester, featuring a pendulum spring, efficiently converts dynamic mass energy into electrical power via the piezoelectric transducer (Plaza Bonilla et al., 2019).

The working process of PENG to harvest ocean energy is shown in Fig. 1.3. The main application scenarios can be divided into bouy sensor, underwater vehicle, and wireless sensor. Considering different coupling types with fluid, types of PENG includes direct coupling, frequency-increasing, flow-induced vibration, and multi-mechanism composite (Liu et al., 2023). The simplest type is the direct coupling, which utilizes the periodicity of waves directly. Therefore, the fixed condition is one important parameter. Fig. 1.4 shows one horizontal fixed condition. The device is parallel to the still water surface and performs repeated bending motions with at the peaks and troughs of the waves (Liu et al., 2023). However, ocean wave always show low frequency, which bring difficulty to energy harvesters. Therefore, frequency-increasing types are necessary. One example in Fig. 1.5 uses the gear train frequency up-conversion mechanism to improve power generation efficiency (Baghbani Kordmahale et al., 2021). In addition, flow-induced vibration is a major research hotspot, which is based on vortex induced vibration. One example is show in Fig. 1.6 (Zhao et al., 2021). Lastly, for multi-mechanism type, Fig. 1.7 shows one example: a wave energy harvester with piezoelectric-electromagnetic components. It is used for self-powered devices around sea-crossing bridges (Qi et al., 2021).

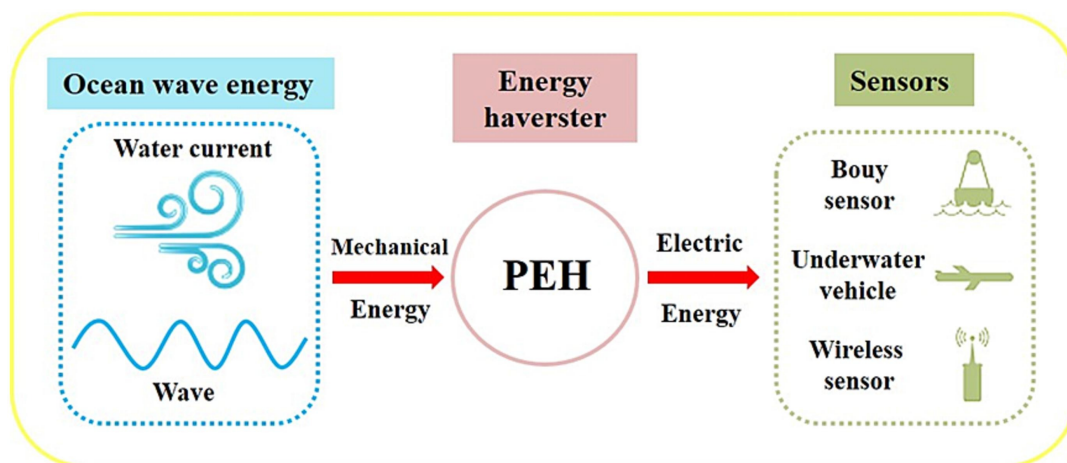


FIGURE 1.3: The working process of PENG to harvest ocean energy (Liu et al., 2023)

Triboelectric Nanogenerators (TENGs) have also demonstrated immense potential in energy harvesting and sensing (Song et al., 2022). For instance, a TENG combined with PENG monitors various parameters such as initial distance, acceleration amplitude, and vibration amplitude (Wardhana et al., 2020; Wardhana et al., 2022). Additionally, a double-float structured TENG was developed for wave hydrological

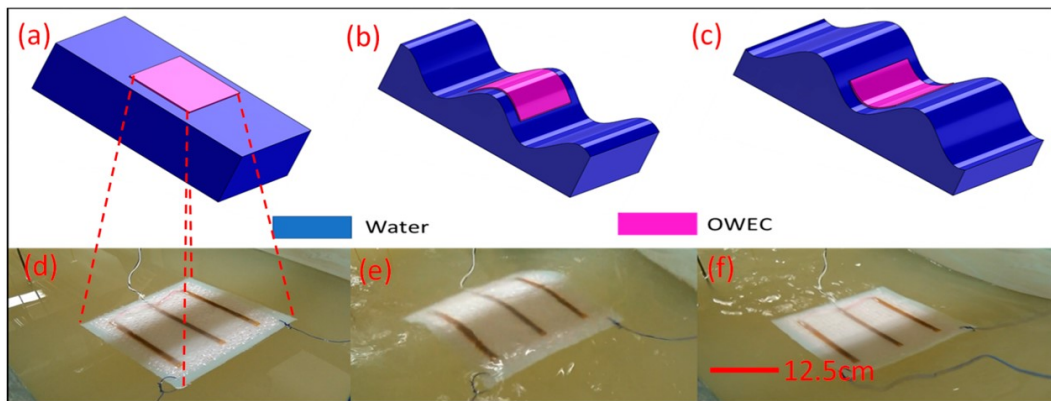


FIGURE 1.4: Working principle of direct coupling PENG (Baghbani Kordmahale et al., 2021).

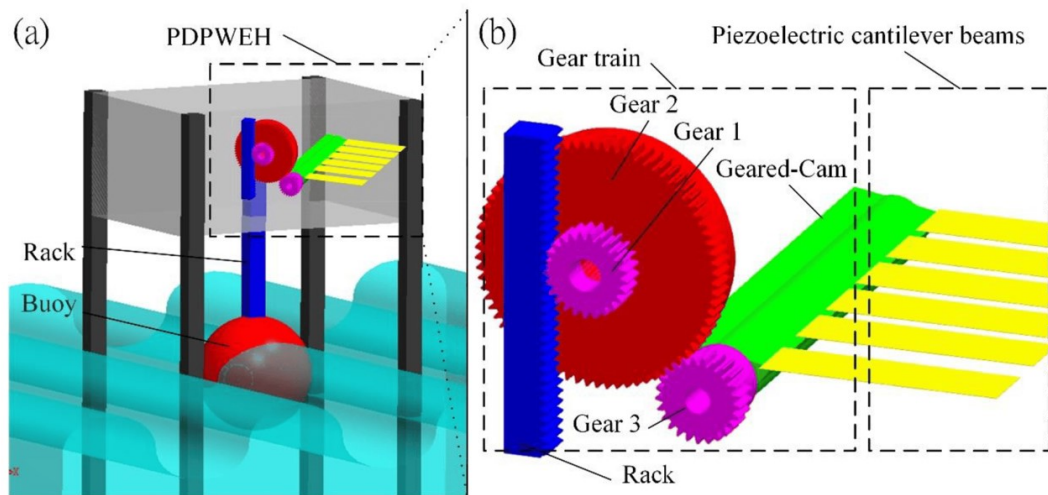


FIGURE 1.5: Working principle of frequency-increasing PENG (Chen et al., 2021).

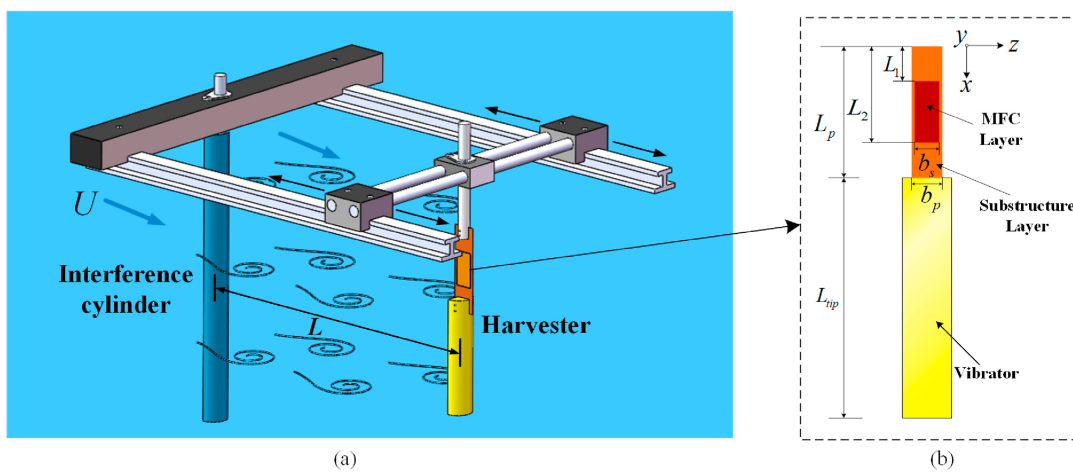


FIGURE 1.6: Working principle of fluid-induced vibration PENG (Zhao et al., 2021).

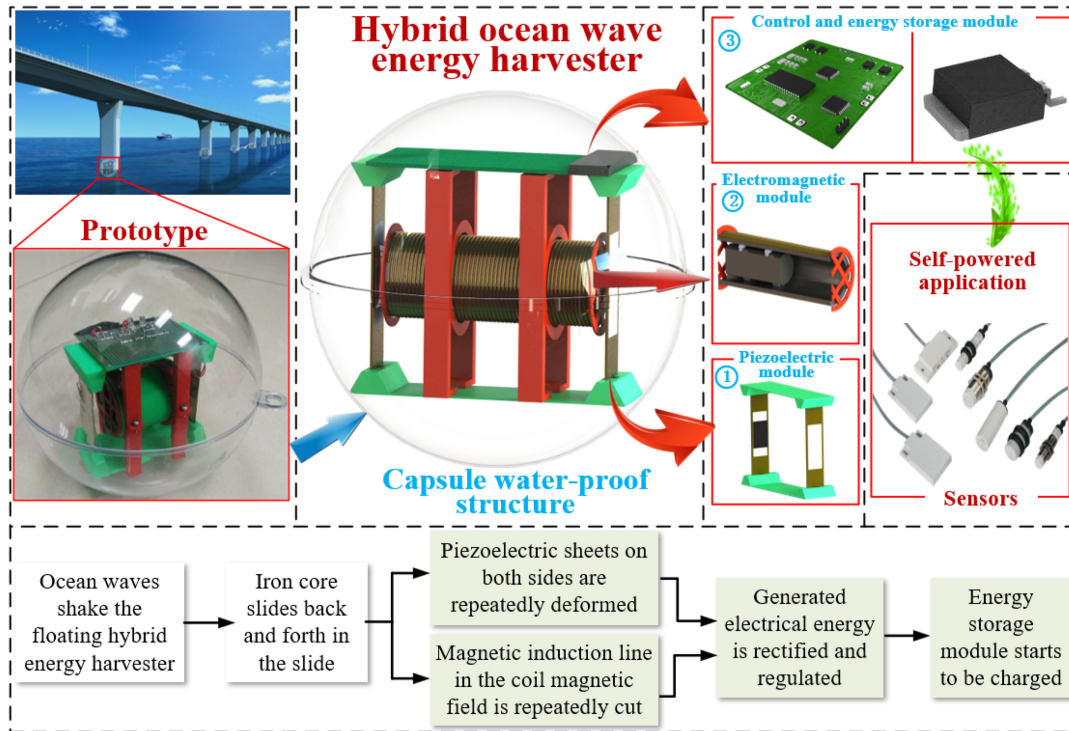


FIGURE 1.7: Working principle of multi-mechanism PENG (Qi et al., 2021).

monitoring (Wang et al., 2022). Moreover, an innovative magnetically circular layers TENG serves as a self-powered speed sensor for vehicles and a crack detector (Jiao et al., 2022). Tao et al. proposed an origami-inspired TENG integrated with folded thin-film electret, demonstrating promising potential for biomechanical and ocean wave energy harvesting (Tao et al., 2020b).

Due to the diversity of TENGs, their fabrication, application and enhancement are mainly focused on when conducting TENG research (Song et al., 2022). The relationship and sub-topics are shown in Fig. 1.8. Depending on whether there is direct contact with water, the types of TENGs can be divided into liquid-solid contact TENG and fully enclosed TENG. Fig. 1.9-1.10 show the liquid-solid contact TENG. Their advantage is that there is no need to consider waterproofing measures, simple structure and low cost. However, it is easily affected by seawater ions and the power generation is unstable (Zhu et al., 2014; Zhao et al., 2018). For the fully enclosed TENGs, the mechanical structures are needed to be designed to response to wave positively. Fig. 1.11, 1.12, and 1.13 show three popular examples with spherical structure, spring-assisted structure, and multilayer structure. Their design purpose is to be able to be stimulated by waves of various directions and types to the greatest extent (Cheng et al., 2019; Liang et al., 2021; Liu et al., 2021).

To improve stimulation by waves, some special structures are needed to be considered. Origami TENGs, leveraging the advantages of origami metamaterials such as self-weight, cost-effectiveness, fabrication flexibility, and tunable performance, have found widespread use in self-powered monitoring. Examples include Miura-origami-inspired and Kresling origami TENGs for self-powered sensing of gait, palm-grasp state, and strength (Huang et al., 2022; Tao et al., 2020a; Lu et al., 2023). Waterbomb-origami-inspired TENGs are developed for traffic monitoring, showing excellent deformability and flexibility (Pang et al., 2022). The schematic diagram is shown in Fig. 1.14. In addition, elastic origami-structured TENGs are reported for

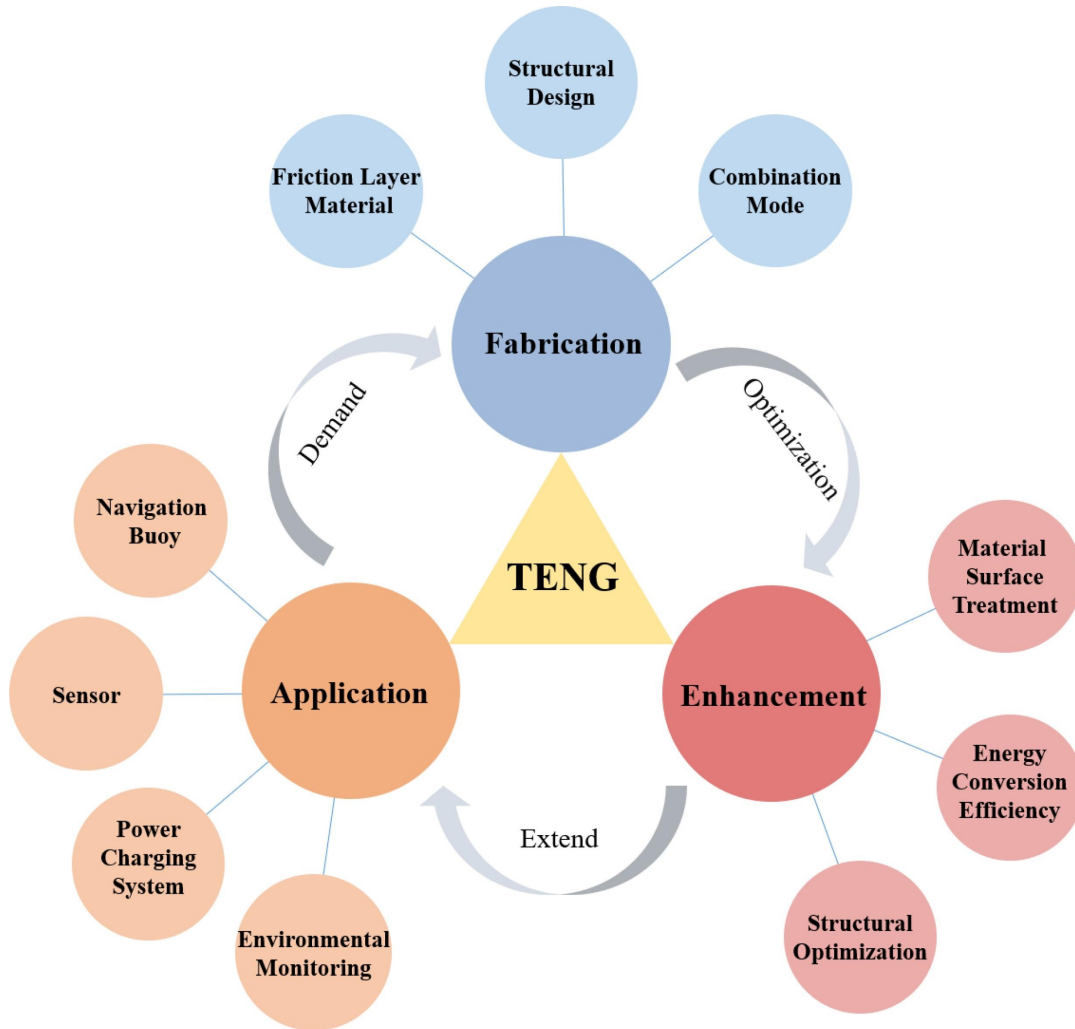


FIGURE 1.8: The research topics, sub-topics, and their relationship of TENG research (Song et al., 2022)

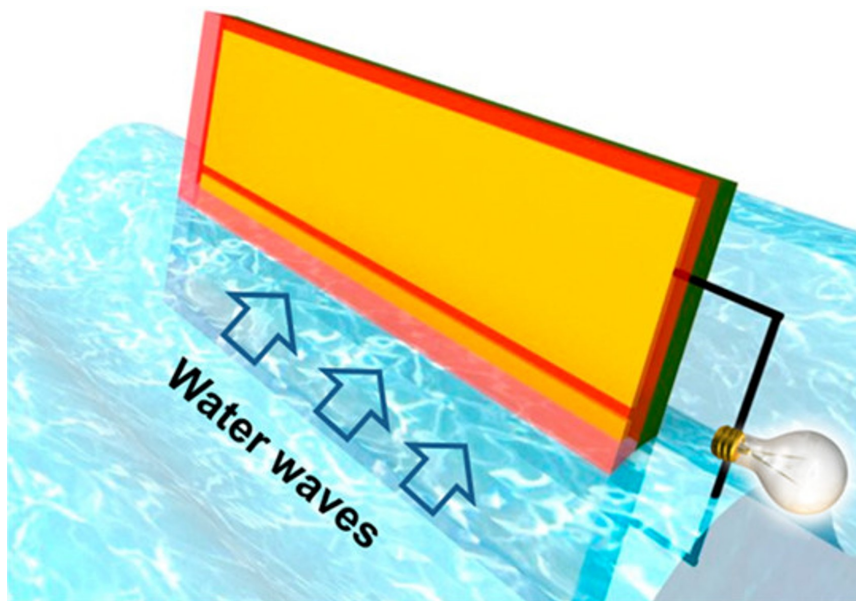


FIGURE 1.9: Liquid-solid contact TENG using Nanostructured Hydrophobic Thin-Film Surface (Zhu et al., 2014).

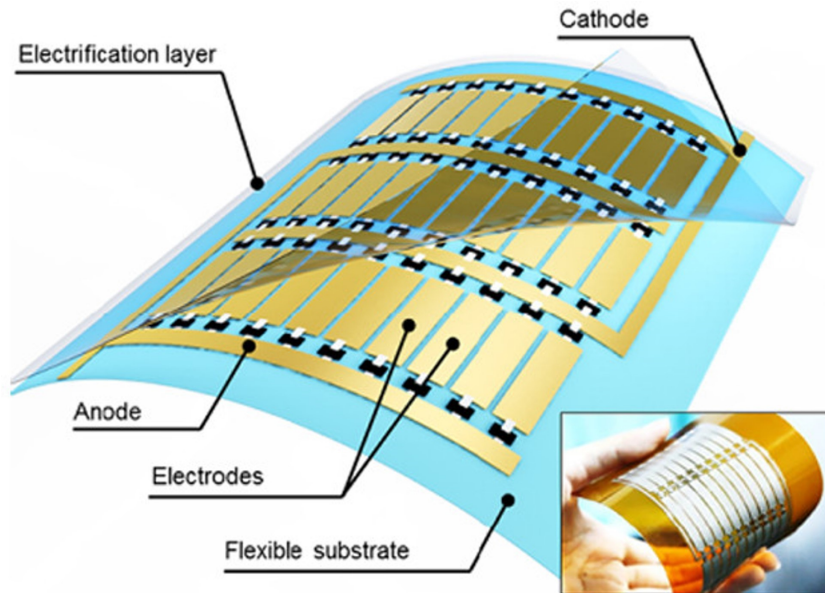


FIGURE 1.10: Liquid-solid contact TENG using a networked integrated triboelectric nanogenerator (Zhao et al., 2018).

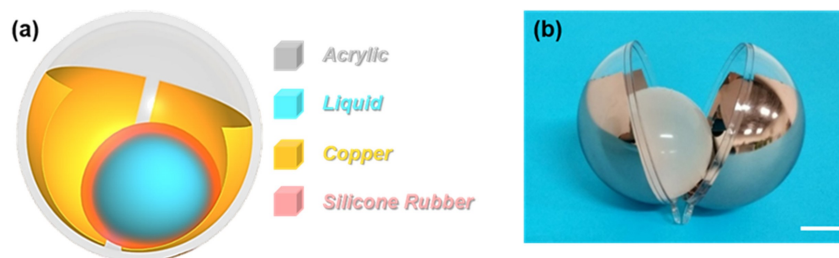


FIGURE 1.11: Fully enclosed TENGs with spherical structure (Cheng et al., 2019).

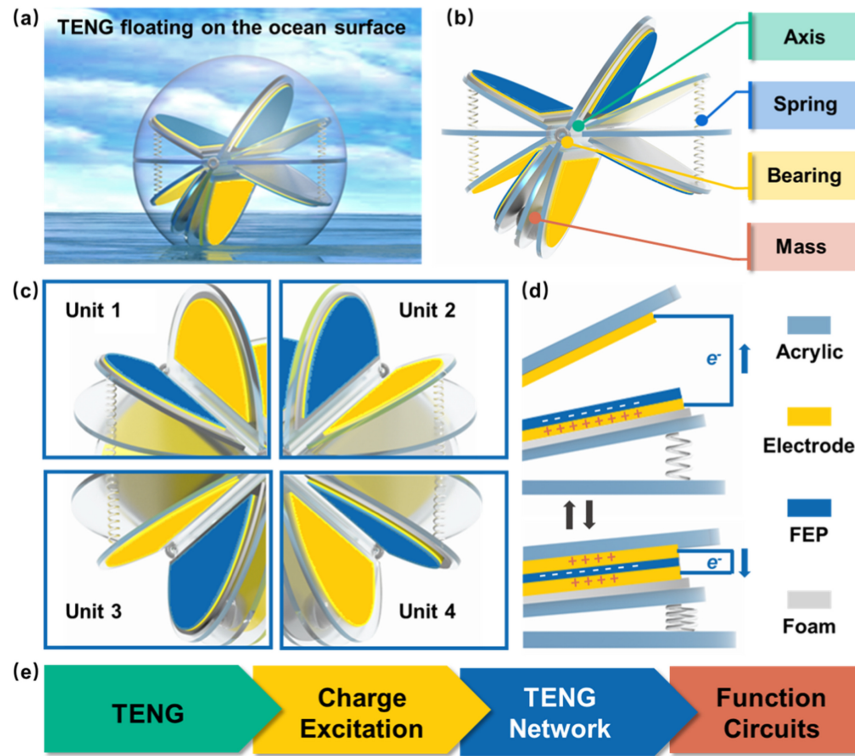


FIGURE 1.12: Fully enclosed TENGs with spring-assisted structure (Liang et al., 2021).

ocean energy harvesting and bridge health monitoring, effectively converting low frequencies into high frequencies (Tao et al., 2020b; Xia et al., 2023). Their schematic diagrams are shown in Fig. 1.15 and 1.16.

However, existing studies predominantly utilize PENGs or TENGs as power sources to charge independent monitoring systems rather than achieving simultaneous powering and sensing through a single device.

1.1.4 Research on turbulent energy around the ocean applications

More and more research focus on the turbulent energy recycle around marine vehicles. The principle of utilizing turbulent energy is to make the turbulent flow field suitable for the natural operating frequency of PENG/TENGs. Therefore, flow field control methods are particularly important. The most mature application on flow field control methods is used for *DR*. Therefore, this study simultaneously analyze feasible solutions and numerical methods from the aspects of *DR* and flow control.

Depending on whether there is a requirement of an external energy supply, control methods for marine transport equipment broadly are categorised to two categories: active control and passive control techniques. For instance, air-injection represents an active control method employed for ship *DR* (Zhao and Zong, 2022). On the other hand, passive control techniques include injecting polymer additives into turbulent boundary layers of liquid flows (Yang et al., 2014), utilizing biomimetic sharkskin riblets in underwater applications (Mawignon et al., 2023), and employing hydrophobic surfaces on marine vehicles (Du et al., 2017) (Altaf, Omar, and Asrar, 2014).

Among these methods, the use of polymer additives has emerged as the most widely employed technique over the seven decades (Toms, 1949; Ptasinski et al.,

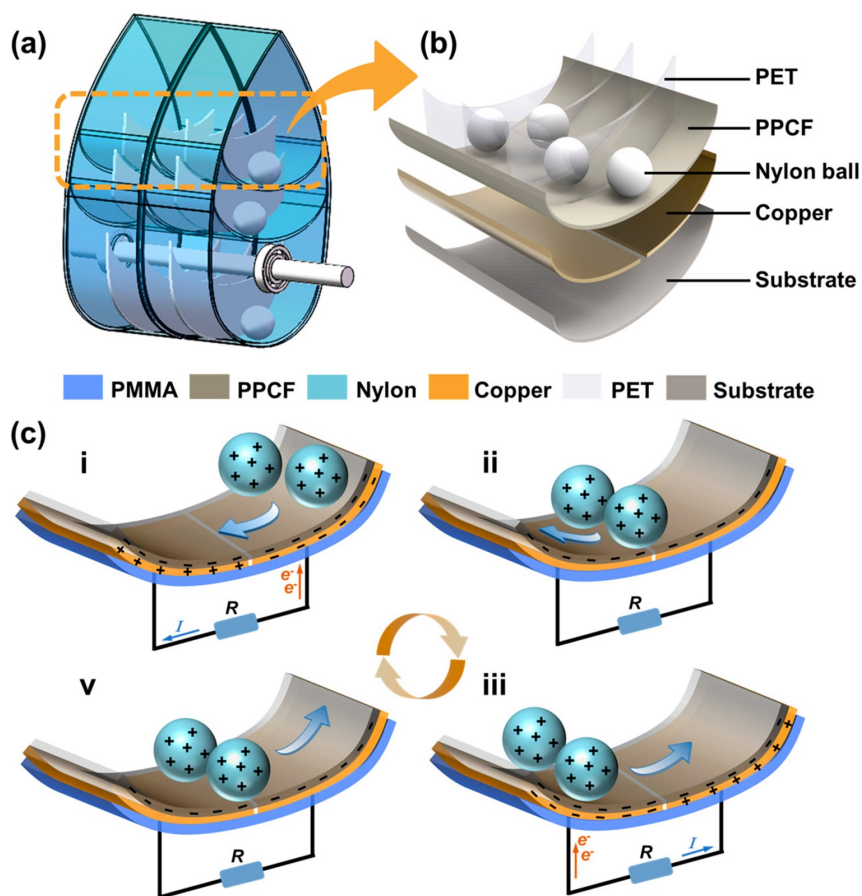


FIGURE 1.13: Fully enclosed TENGs with multilayer structure (Liu et al., 2021).



FIGURE 1.14: The schematic diagram of Waterbomb-origami-inspired TENGs (Pang et al., 2022).

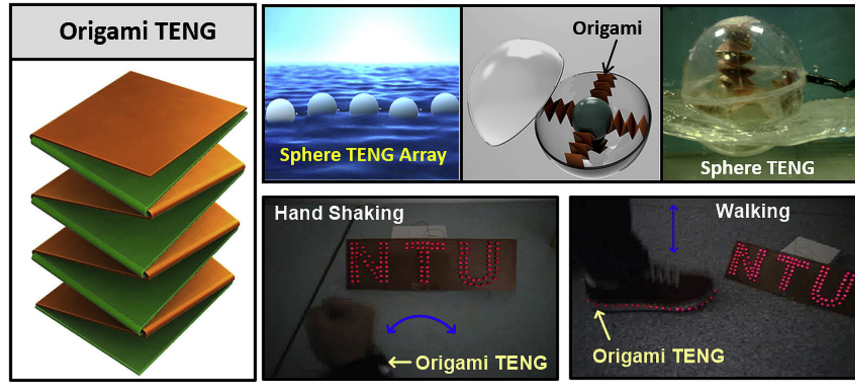


FIGURE 1.15: The schematic diagram of elastic origami-structured TENGs harvesting wave energy (Tao et al., 2020b).

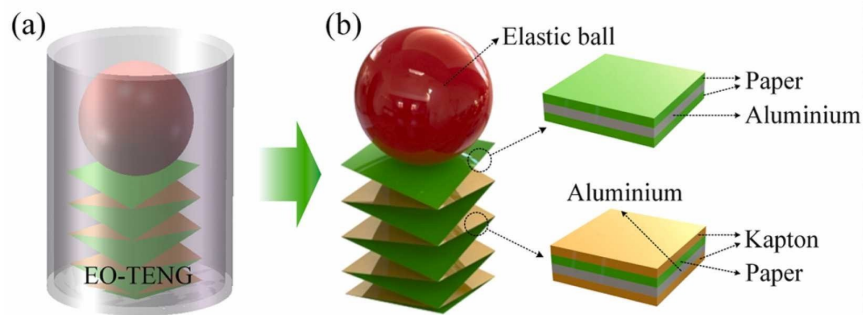


FIGURE 1.16: The schematic diagram of elastic origami-structured TENGs monitoring bridge health (Xia et al., 2023).

2001; White and Mungal, 2008). Even in minute quantities, polymer additives in turbulent flows are acknowledged as effective agents in reducing drag, with reported *DR* rates reaching as high as 70% (Xi, 2019; Benzi and Ching, 2018; Escudier, Nickson, and Poole, 2009; Ptasinski et al., 2001). In most laboratory and industrial-scale tests, the drag-reducing polymer blends with the entire fluid to establish a homogeneous internal flow, often within pipes.

When it comes to drag reduction for marine vehicles, directly injecting a polymer solution into external flows isn't a viable approach. Instead, the polymer material is either injected or allowed to infiltrate the turbulent layer surrounding the surface (BERMAN, 1986; Hoyer and Gyr, 1996; Tiederman, Luchik, and Bogard, 1985; Semenov, 1991). While these methods have marked significant breakthroughs in research, designing universal jets or penetrating layers for every traffic type remains unfeasible, and injection orifices may compromise the vehicle's structural integrity.

Advancements in coating material technology have led to the use of various high-molecular polymers as coatings or additives in paint. For instance, Polyethylene oxide (PEO), a drag-reducing polymer, was incorporated into conventional antifouling (AF) paint by Motozawa et al. (Motozawa et al., 2010). This facilitated a significant drag reduction by continuously releasing polymer molecules around the ship hull surface. Although the Reynolds shear stress gradually increased as the polymer dissipated over 42 hours, the stress near the wall consistently remained lower than that without the added polymers. Additionally, the effectiveness of drag reduction depends on surface roughness. To address this, J.W. Yang et al. developed a novel marine paint with fine PEO powder with self-polishing copolymer (SPC)-AF (Yang et al., 2014). Compared to conventional AF paint with PEO, which achieves a

maximum 20% reduction, the PEO mixed with SPC-AF attains up to a 33% reduction in skin friction. Subsequently, Rowin et al. proposed the polymer coating without AF paint to solve the issue that residual rough AF paint causing increased drag after the drag-reducing polymer depletes (Rowin et al., 2021). This coating comprises two layers of commercial anionic polyacrylamide and polydopamine.

Although those experiments have been conducted initially, the mechanism behind, especially the drag-reducing properties of non-homogeneous polymer solutions in polymer coatings, is still unclear.

1.1.5 Previous studies on numerical method

limited research has focused on the non-uniform behavior of polymer Drag Reduction (*DR*) in external flows, particularly in the cases like polymer coatings on vehicle surfaces. Most theoretical models are about the mechanisms of polymer additive solutions.

The Direct Numerical Simulation (DNS) has integrated control techniques such as suboptimal control and reduced-order linear feedback control to compute turbulent channel flow *DR* (Lee, Kim, and Choi, 1998; Lee et al., 2001; Endo, Kasagi, and Suzuki, 2000; Iwamoto, Suzuki, and Kasagi, 2002). Another prevalent model approximates polymer molecules as elastic dumbbells using a spring force (Sureshkumar, Beris, and Handler, 1997; Bird et al., 1987; Yu and Kawaguchi, 2004; Tamano et al., 2007). Among these, the Finitely Extensible Nonlinear Elastic (FENE) model with a viscoelastic constitutive equation stands as the most widely adopted, accounting for polymer stress contributions to momentum balance (Sureshkumar, Beris, and Handler, 1997; Bird et al., 1987).

Despite diverse theoretical explanations based on elastic or viscous polymer molecule effects on flow phenomena, no universally accepted theory exists. However, these theories primarily are developed for polymer solutions in internal flows, overlooking specific conditions like local polymer effects, polymer coatings, and heterogeneous polymer solutions in numerical simulations. Moreover, DNS demands high spatial and temporal resolution, resulting in computational intensity, time consumption, and memory dependency.

Recognizing this research gap, there's a pressing need for a novel method to rapidly depict the characteristics of non-uniform polymer solutions. Specifically, in simulating the free distribution of polymer coatings over surfaces, the polymer model and flow remain independent, linked only through certain parameter interactions.

In fluid simulation, employing a low-pass filter within Navier-Stokes equations via Large Eddy Simulation (LES) reduces calculation time by neglecting the tiniest length scales, while turbulence models in Computational Fluid Dynamics (CFD) disregard these scales (Muhammad, Lashin, and Alkhatib, 2022). Computational models for polymeric systems can be categorized into atomistic, mesoscopic, and continuum, based on length and time scales (Liu et al., 2015). Continuum simulation falls short for systems like proteins, membranes, and polymers, as it lacks representation of microscopic-level details. Atomistic and mesoscopic models, encompassing fluctuating hydrodynamics and microscopic phenomena like shear thinning or thickening, viscoelasticity, jamming, and flow-induced phase transition, prove suitable (Espanol and Warren, 2017; Yasuda and Yamamoto, 2008).

Yasuda introduced a model for multiscale hybrid simulations, likening cells in Molecular Dynamics (MD) to CFD's mesh. In this approach, CFD provides data on a "local flow field" to MD in each time step, while MD generates a "local stress" input

to CFD (Yasuda and Yamamoto, 2008; Muhammad et al., 2022; Ahmed, Muhammad, and Zaman, 2022; Muhammad, Ullah, and Khan, 2022; Muhammad, Zaman, and Mustafa, 2022). Yasuda categorized methods for combining these models into parameter concatenation, domain decomposition, and local sampling methods. While the atomistic model provides detailed microscopic insight, its computational expense due to small size makes the mesoscopic model more practical.

Dissipative Particle Dynamics (DPD) stands as a representative mesoscopic simulation method initially proposed by Hoogerbrugge and Koelman (Hoogerbrugge and Koelman, 1992; Koelman and Hoogerbrugge, 1993). Compared to MD and Lattice Gas Automata (LGA), DPD combines their advantages with higher simulation speed and flexibility. In polymeric systems, DPD particles represent solvent particles, enabling more realistic simulations than conventional theories (Moeendarbary, Ng, and Zangeneh, 2010). DPD's application primarily revolves around exploring rheological properties of polymers, block copolymers, and mesophase separation. The method allows for easy manipulation of polymeric systems by arbitrarily adjusting conservative forces between dissipative particles, aided by DPD's symmetrical structure expression, facilitating the exploration of generic or universal system features (Espanol and Warren, 2017).

1.2 Motivation

As mentioned above, renewable energy development plays a very important role in coping with the energy crisis. In previous studies, the necessity of utilization of ocean wave and flow energy, has been proposed. However, several research gaps remain:

- It is difficult for energy harvesting devices to perform both sensing wave parameters and powering other sensors at the same time.
- There are few studies on the design of energy harvesting devices and how to maximize the power generation when coupling with waves. In addition, there is no complete process.
- During numerical simulation, traditional grid methods often suffer from distortions due to the large motions of energy harvesting devices in waves. Its numerical algorithm development meets challenges.
- There are few numerical algorithms and mechanism about exploring the turbulence energy and flow control with local polymer coating. This research can be applied to improve power generation of turbulent energy harvesters using PENG/TENGs.
- The majority of algorithms choose the DNS method, demanding high spatial and temporal resolution. This approach proves computationally intensive, time-consuming, and heavily reliant on computer memory. Therefore, alternatives are needed when dealing with high Reynolds cases.

This study propose corresponding solutions to the above research gaps one by one.

1.3 Thesis Overview

This study focuses on the energy harvesting of fluid. Firstly, two kinds of wave energy harvesters based on PENGs and TENGs are developed and optimized based

on experimental and numerical researches. Subsequently, numerical algorithms of polymer coating DR are developed to implement flow control and estimate the turbulence energy. Prospects of using optimized flow to improve turbulence energy harvesting using PENGs/TENGs are proposed.

In chapter 2, the design process of the two energy harvesters based on PENGs and TENGs are introduced respectively.

In chapter 3, working parameter selections of the energy harvesters based on PENGs mentioned in chapter 2 are carried out. Experiments for the test of the dominant characteristics including submerged depth, aspect ratio (AR), and thickness of the painting material under different support types and wave conditions are conducted. Then, a field test was conducted to evaluate the practical application of the device in real ocean conditions. The support type indicates how the device are fixed onto the frame. Additionally, we proposed a theoretical model to assess the device, considering crucial parameters. To compensate for the limitations of the theoretical model, which couldn't perform specific coupling operations, we developed a computational model based on IBM. Subsequently, we validated this computational model using both experimental and theoretical data.

In chapter 4, we try to improve the power generation of the energy harvesters based on TENGs mentioned in chapter 2 step by step. To simply simulate wave environment, swing machine experiments are conducted in uni-direction and multi-direction numerical wave tank with SPH method. Then, the test of optimized device is under large-scale wave tank experiments.

In chapter 5, we focus on recycling turbulent energy using TENGs/PENGs. Firstly, a new theoretical model combining DNS/LES with DPD methods should be proposed to estimate the turbulent energy and control flow field with polymer coating. In Section 5.1, the governing equations and the coupling scheme for this hybrid method are introduced. Then, the Section 5.2.2 presents some comparisons, including that between our results with the reference ones, that between the results using DNS-DPD and LES-DPD methods, and that between our results with the ones using FENE method. Furthermore, the Section 5.2.3 demonstrate it is possible to use the LES-DPD approach under different Reynolds numbers. Subsequently, the Section 5.2.4 shows the influence of the polymer region height. At last, the Section 5.2.5 shows the estimation of turbulent energy and flow field control. Simultaneously, the possibility of flow control using polymer coating to improve energy harvesting ability of PENGs/TENGs.

Chapter 2

Development of ocean energy harvesting device

2.1 Overview of piezoelectric-painted-based ocean energy harvester

Firstly, flexible piezoelectrical energy harvester devices (FPEDS) are developed. The FPEDs are composed of piezo-material and elastomer such as rubber and silicone. They are designed to efficiently convert ambient kinetic energy from sources like currents, waves, and wind into electrical power. In the previous study, these FPEDs are optimized by selecting their AR, initial tension, support system, and incorporating a bluff body for flow-induced vibration (Mutsuda et al., 2017b). Subsequently, in our another work, one piezoelectric material was directly coated onto the FPED and electrode substrate, addressing issues of durability against bending and weathering caused by forces in waves and currents (Mutsuda et al., 2017a). Fig. 2.1 illustrates the spray coating process used for the painted FPED, where a gun nozzle deposits the piezoelectric paint onto the substrate surface, integrated with an elastic material. The techniques and process for coating were developed as proposed in (MUNEKATA Co., 2019b; MUNEKATA Co., 2019a).

As Fig. 2.2 demonstrated, the painted FPED features a laminated structure. The structure of the painted FPED are refined based on those key parameters including the AR, painting material thickness, and the base substrate material. The dimensions of the painted FPED are characterized by its length (L_1), width (B_1), and thickness (t_1). The area covered by the piezoelectric paint is represented by dimensions L_2 , B_2 , and t_2 . This piezoelectric paint is layered and positioned between upper and lower electrodes made of polyphenylene sulphide (PPS) coated with copper paint. To ensure connectivity, a coaxial cable links both electrodes, establishing a connection with a data logger device via a laptop computer. Additionally, a waterproof coating is applied to both the front and back sides of the device for enhanced protection.

Fig. 2.3 illustrates the open electric circuit, including a $1\text{ M}\Omega$ resistor, which serves as the internal resistance for the data logger. The measurement of the output voltage produced by the painted FPED involves a data logger, A/D converter, and a laptop computer. Based on Ohm's law, electrical power can be calculated. To ensure efficient power transfer and functionality in practical applications, impedance matching was essential, prompting optimization in the design of the electric circuit.

Then, we design six painted FPEDs using the specifications outlined in Fig. 2.2 and parameter values summarized in Table 2.1. Our investigation includes different ARs (B_2/L_2) of 1:2, 1:3, and 1:5 to assess their impact on their output voltage. For

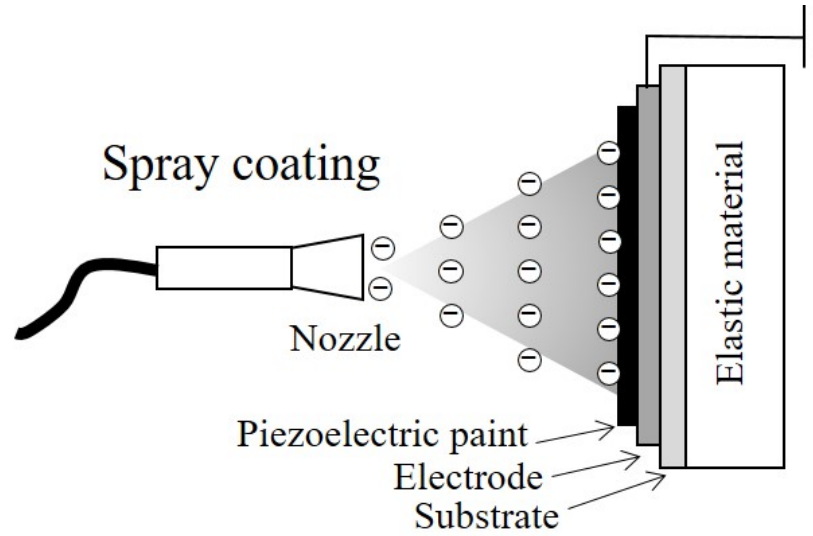


FIGURE 2.1: Illustration of the spray coating technique implemented for the painted FPED; The piezoelectric paint ejecting from the nozzle can be covered on the electrode with the substrate .

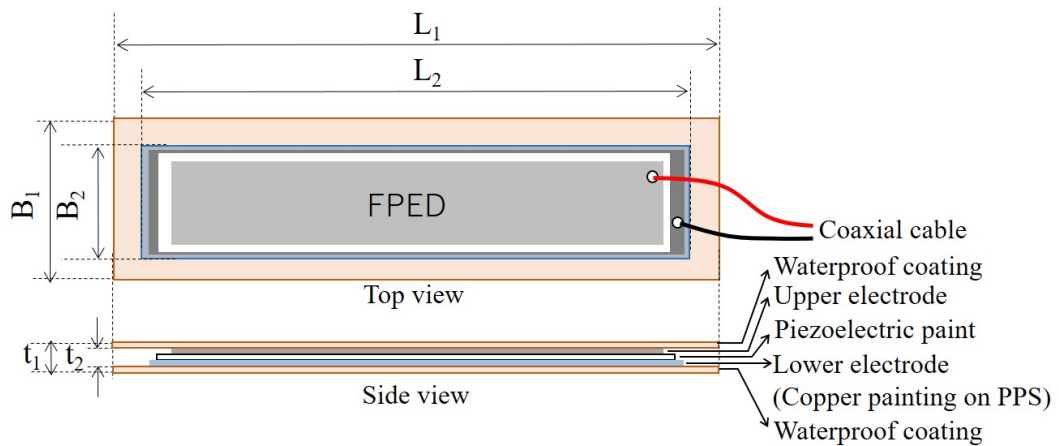


FIGURE 2.2: A unimorph type of the laminated structure of the painted FPED; The piezoelectric paint area is put between the upper electrode and the bottom one covered by the waterproof coating.

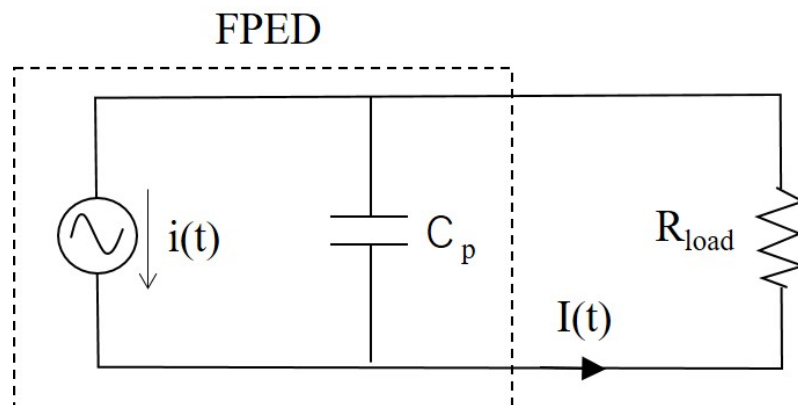


FIGURE 2.3: One example of an electric circuit for the painted FPED with the resistance.

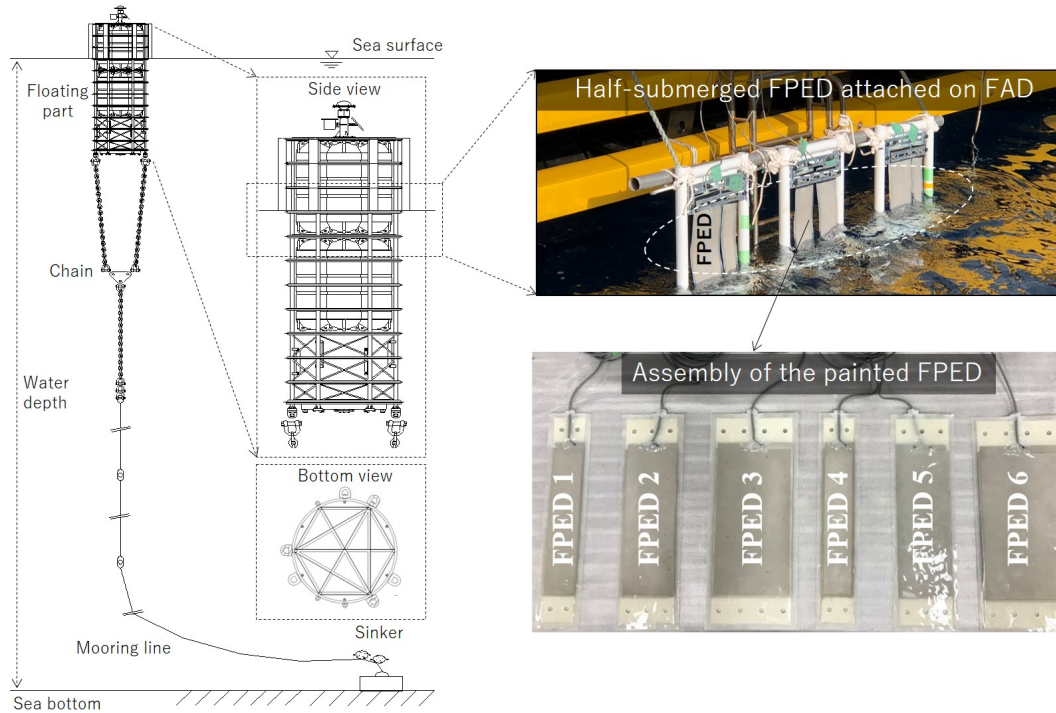


FIGURE 2.4: Overview of the FAD in real sea condition and an ocean energy harvester using the painted FPED attached to the FAD. The painted FPED can be vertically and horizontally set on the FAD metal frame near the sea surface; Several painted FPEDs with different AR and thickness are installed in the field test.

the thickness of the PPS substrate, We optimized it to 0.8 mm based on preliminary studies (Mutsuda et al., 2017a).

TABLE 2.1: Specifications of the painted FPEDs. The parameters correspond to those shown in Fig.2.2

| Name | L_2 (mm) | B_2 (mm) | t_2 (μ m) | AR ($B_2 : L_2$) |
|--------|------------|------------|------------------|--------------------|
| FPED 1 | 300 | 60 | 50 | 1:5 |
| FPED 2 | 300 | 100 | 50 | 1:3 |
| FPED 3 | 300 | 150 | 50 | 1:2 |
| FPED 4 | 300 | 60 | 100 | 1:5 |
| FPED 5 | 300 | 100 | 100 | 1:3 |
| FPED 6 | 300 | 150 | 100 | 1:2 |

Under real sea environment, the painted FPEDs are connected to the fish aggregating device (FAD). As Fig. 2.4 shows, the painted FPED offers versatility in its setup of vertical or horizontal positioning through either a cantilever or support at both ends on the FAD frame. Factors like water depth and the mooring line determine the submerged depth near the water surface.

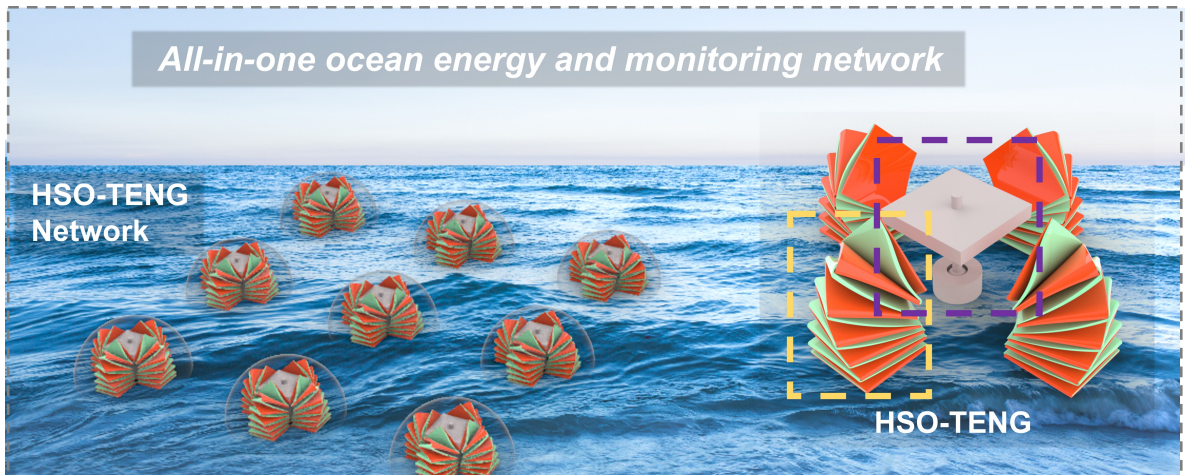


FIGURE 2.5: Schematic diagram of HSO-TENG array in ocean and the distribution of components in one disassembled HSO-TENG.

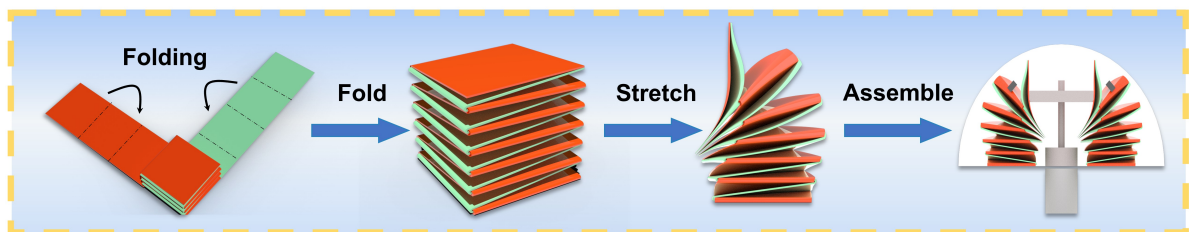


FIGURE 2.6: Schematic diagram of the preparation process of the SO-TENG.

2.2 Structure design of hemi-spherically spring origami triboelectric nanogenerators

In Fig. 2.5, the schematic diagram of the HSO-TENGs network, showcasing their array within the ocean, is illustrated. Each HSO-TENG unit comprises a circular bottom plate, a transparent hemispherical shell, a rotatable hammer, and four Spring Origami (SO) TENGs.

Fig. 2.6 shows the preparation process of the SO-TENG. Initially, the SO-TENGs are folded from two long strips and become a helical elastic structure. Subsequently, they are bent, with one end connected to the hammer and the other end connected to the hemisphere base. Prior research has proved the effectiveness of SO-TENGs in both ocean energy harvesting and bridge monitoring (Tao et al., 2020b; Xia et al., 2023).

Fig. 2.7 provides a detailed perspective of the rotatable hammer. In Fig. 2.7(i), two parts are displayed: the first consists of the hammer head, the stick, and a tail sphere, while the second component is a cylinder with a hollow center, slightly larger than the sphere in the first part. Fig. 2.7(ii) demonstrates that this hammer configuration permits a 30-degree swinging motion perpendicular to the XY plane, ensuring omnidirectional energy harvesting capabilities for the HSO-TENG.

In Fig. 2.5d, the working mechanism and charge distribution map during the slapping motion are depicted. Notably, the two strips within the SO-TENG are constructed as four-layer and five-layer structures, respectively, securely fastened using 1cm wide double-sided tape. Polytetrafluoroethylene (PTFE) and polyvinyl chloride

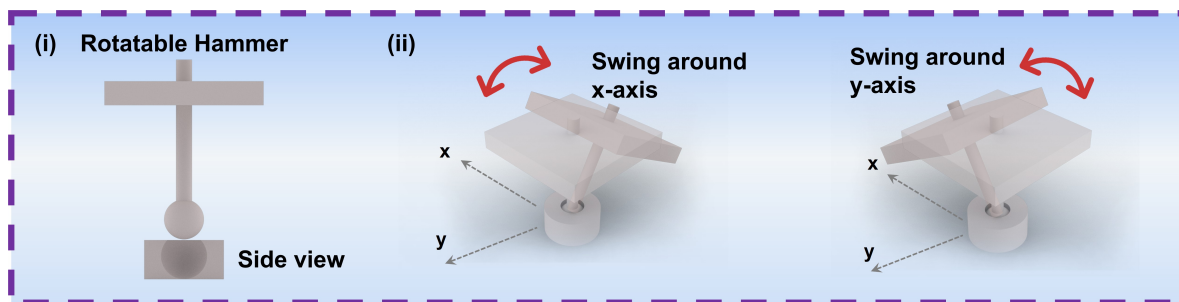


FIGURE 2.7: The structure and working mechanism of the rotatable hammer.

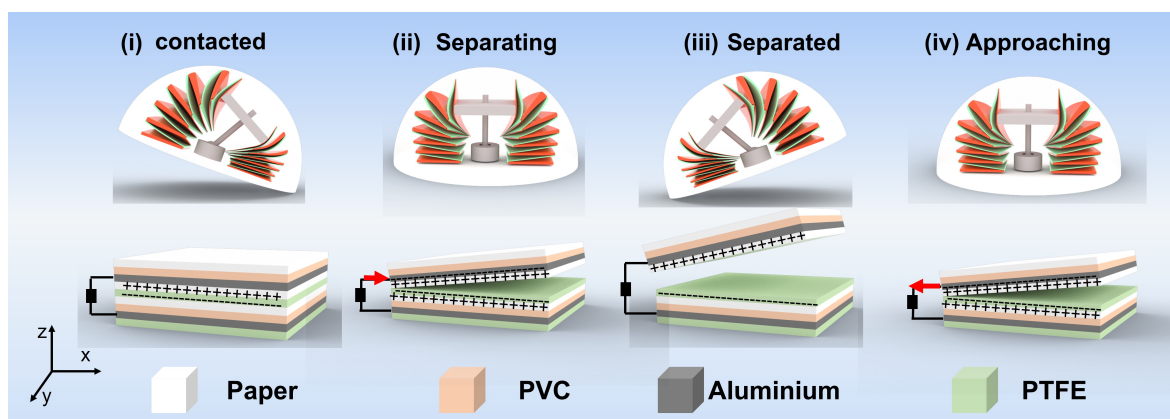


FIGURE 2.8: The working mechanism, charge distribution map and fabrication of the SO-TENG. (The width and the length of the strips is 7.5cm and 100cm. The basis weight of paper is 104g/m², the thickness of PVC is 0.25mm, the thickness of aluminum tape is 0.08mm, and the thickness of PTFE is 0.1mm. They are connected with double-sided tape with a width of 15mm.)

(PVC) are chosen as materials due to their good electron transfer properties. The utilization of soft PVC enhances the overall self-recovering ability of the SO-TENG. In the diagram, only the two SO-TENGs along the x-axis are displayed, concealing the two along the y-axis. As observed, when the HSO-TENG undergoes a swinging motion around the y-axis, the internal pendulum compresses and stretches the SO-TENGs aligned along the x-axis. For instance, the two strips of the SO-TENG on the right make contact and separate during compression and stretching, leading to charge exchange between paper and PTFE. The spring origami structure ensures effective charge generation on both strip sides, optimizing the device's energy conversion capacity. An essential aspect is that the SO-TENGs exhibit distinct left-handed and right-handed rotation states upon stretching, contingent on the stacking directions (Yoneda, Matsumoto, and Wada, 2019). To ensure symmetry, each set of SO-TENGs is deliberately designed as both left-handed and right-handed structures.

Chapter 3

Working parameter selections of FPED

3.1 Experimental work

In this section, wave-coupling experiments are conducted in wave tank. During the experiments, various wave conditions are set to assess the wave-generated electrical performance of the painted FPEDs. In Fig. 3.1, the experimental setup of a towing tank sized at 100 m × 8 m × 3.5 m is depicted. A wave paddle generates regular waves on the tank's upstream side, while an absorbing beach is positioned downstream to minimize wave reflection and scattering. Additionally, the incident wave elevation is measured on the upstream side. The wave conditions includes a wave height, H , ranging from 50 to 150 mm, and a wave period, T , varying from 1.0 to 1.5 s. The wave steepness, H/λ (where λ represents the wavelength), varying from 0.015 to 0.096.

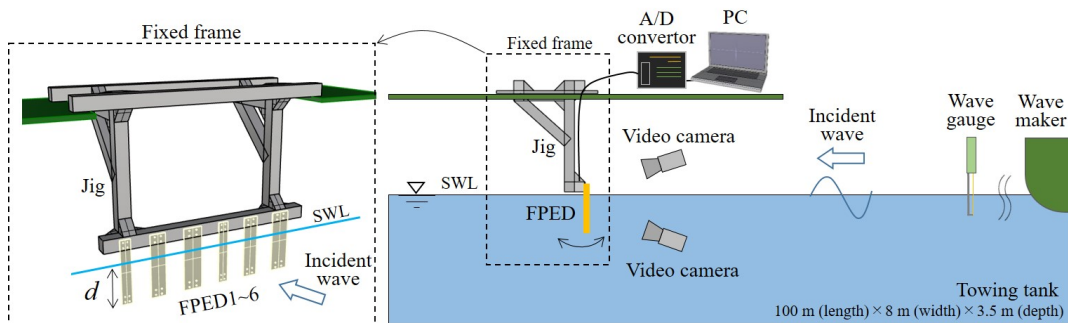


FIGURE 3.1: Experimental setup in a towing tank. The painted FPED is positioned near the water surface at the centre of the tank. Regular waves are generated by the wave paddle on the upstream side, and the absorbing beach is set on the downstream side of the tank.

Then, tests of various support types position on a fixed frame are conducted. We compare three support configurations—vertical both-end-support, vertical cantilever, and horizontal cantilever (Fig. 3.2)—to understand their impact on output voltage. In the case of vertical both-end-support, both upper and lower ends of the painted FPEDs are fixed vertically. Vertical cantilever configuration involves one end being free, while horizontal cantilever needs the painted FPEDs being fixed horizontally with one end fixed and the other free. The blue line marked as SWL represents the standing water level, while d indicates the distance between the SWL and the submerged end, serving to examine depth's influence on output voltage. We measure the output voltage generated by the painted FPEDs using an A/D converter. To

capture the motion of the painted FPEDs, two video cameras—one above and one underwater—were used.

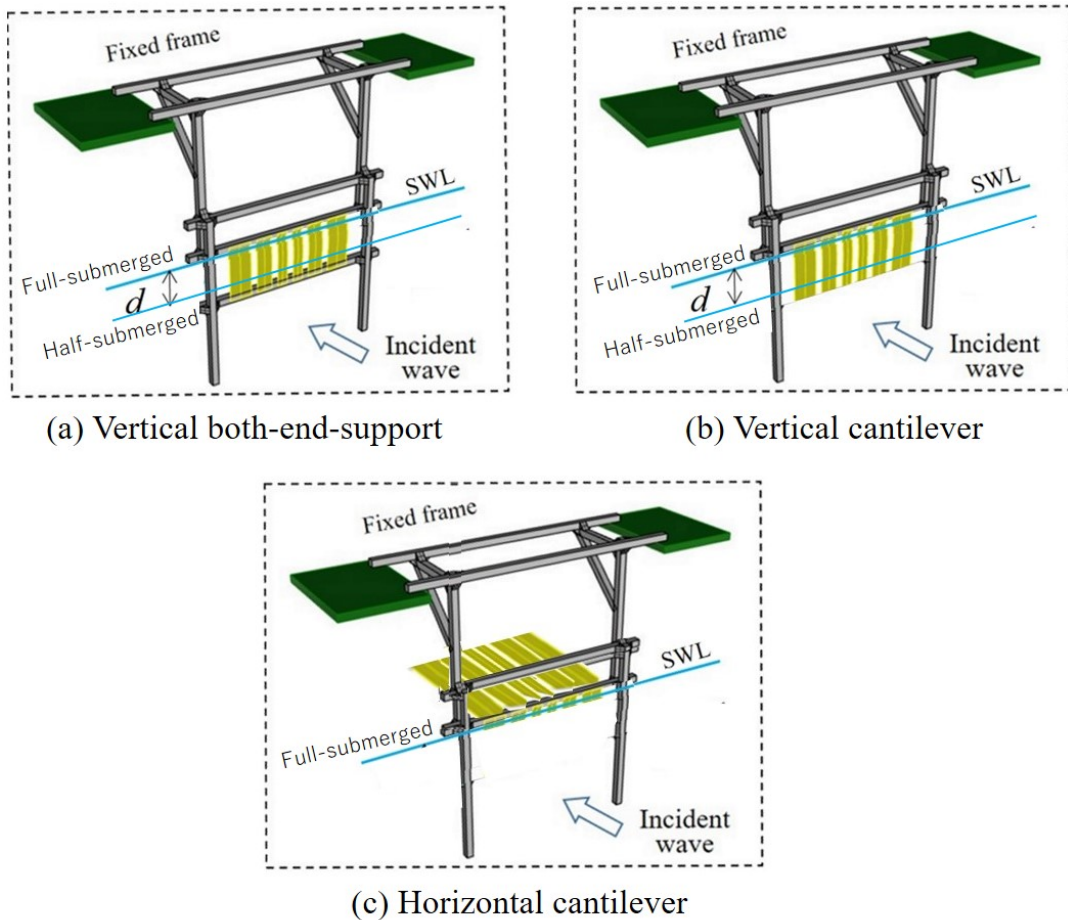
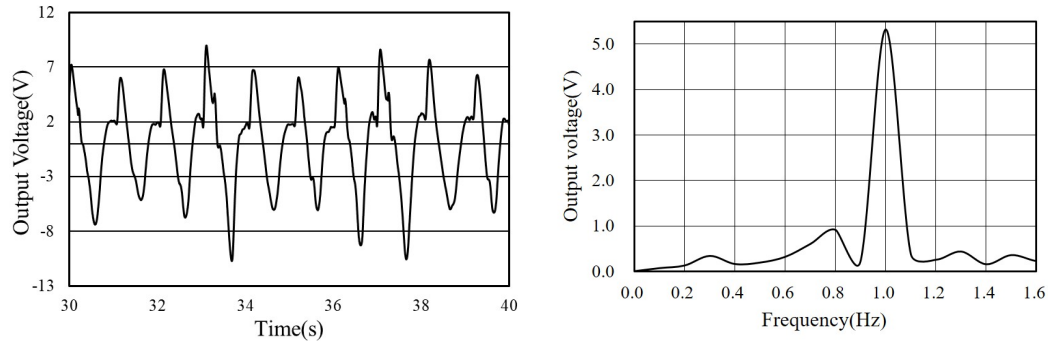


FIGURE 3.2: Several support types for painted FPED, with different submerged depths. The support type was selected considering practical applications under real sea conditions. The painted FPED can be fixed by cantilever support or both-end-support. SWL: standing water level. d : the distance between the SWL and the underwater end.

In Fig. 3.3, an illustrative example displays the time histories of the painted FPEDs' output voltage corresponding to the incident regular wave with a period of $T=1.0$ s, along with its spectral distribution in the frequency domain. Under the influence of regular wave conditions, the painted FPED exhibited periodic measurements of the output voltage without any electrical noise. Notably, the velocity amplitude attain its peak at a frequency of 1.0 Hz (equivalent to a period of 1.0 s). The maximum output voltage was derived by calculating the average of the half amplitude observed across the time history of the output voltage

3.2 Theoretical model

The foundational theoretical model (Patel, McWilliam, and Popov, 2014), slightly modified, was utilized to forecast the electrical power generated by the painted FPED across various support types and depths. This theoretical model accommodates both vertical and horizontal support configurations, encompassing cantilever support and both-end support. This is the same as the experimental setup.



(A) Time history of the measured output voltage (B) FFT result of the measured output voltage

FIGURE 3.3: Example of the measured output voltage of the painted FPED. The maximum and average output data are calculated from the measured raw data; Fast Fourier transform (FFT) is employed to determine the peak value and dominant frequency.

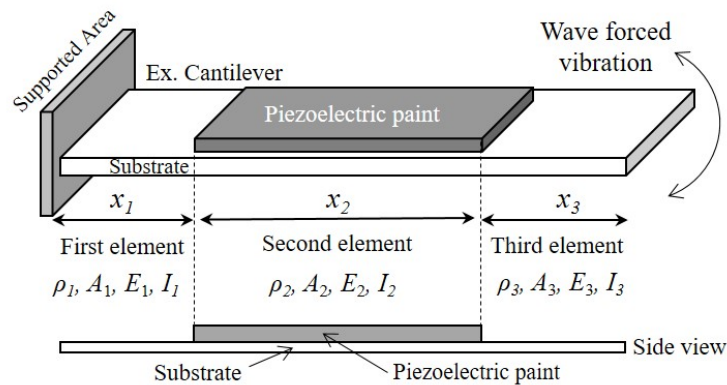


FIGURE 3.4: Parameter settings for a unimorph-type painted FPED in the theoretical model. The painted FPED can be deformed by external forces, such as waves and currents; This model is based on the prototype of the painted FPED shown in Fig. 2.2 and 2.4. The second element (x_2) indicates the piezoelectric paint area.

Fig. 3.4 illustrates the theoretical model devised for the painted FPED, showing a representation of unimorph-type cantilevers supported by a jig on one side, while the external force induces deformation on the opposing side. In Fig. (Morison, Johnson, and Schaaf, 1950), the notation x_1 denotes the length from the supported area to the left side of the piezoelectric paint, x_2 signifies the length of the painted piezo material, and x_3 represents the length from the right side of the piezoelectric paint to the free side. The painted piezoelectric materials were applied from x_1 to x_3 on the PPS substrate, where x_2 denotes the length of the painted piezo material. Drawing insights from previous experimental studies, we postulated that the painted FPED would be stimulated by a typical harmonic motion, specifically in the first deformation mode. The transverse displacement was computed as follows:

$$w(x, t) = w_{rel}(x, t) + w_b(x, t), \quad (3.1)$$

The displacement of the painted FPED, denoted as $w_{rel}(x, t)$, is influenced by the excitation of the base $w_b(x, t)$ with specific amplitude and frequency. Utilizing this data, the external force F_e can be computed based on fundamental water-wave theory (Patel, McWilliam, and Popov, 2014). The mechanical characteristics of the painted FPED were derived from Equation (3.2).

$$\frac{\partial}{\partial x^2} \left[EI(x) \frac{\partial^2 w_{rel}(x, t)}{\partial x^2} + \epsilon V(x, t) \right] + m(x) \frac{\partial^2 w_{rel}(x, t)}{\partial t^2} = F_e \quad (3.2)$$

Here, $EI(x)$ represents the flexural rigidity, $V(x, t)$ denotes the output voltage of the painted FPED, ϵ signifies the permittivity at constant strain, and $m(x)$ stands for the mass per unit length.

The equation governing the output voltage of the painted FPED can be expressed as follows:

$$C_p \frac{\partial V(t)}{\partial t} + \frac{V(t)}{R_{load}} = \sum_{q=1}^{\infty} -E_p d_{31} t_{pc} b_p \left[\frac{\partial W_q(x)}{\partial x} \right]_{x_1}^{x_1+x_2} \eta_q(t), \quad (3.3)$$

In these equations, C_p represents the piezoelectric internal capacitance, R_{load} stands for the load resistance, q denotes the mode number, E_p is the Young's modulus of the piezoelectric material, d_{31} indicates the piezoelectric material constant predominantly in the transverse direction, t_{pc} represents to the distance between the neutral axis and the center of the piezoelectric material, b_p represents the width of the piezoelectric layer, and η symbolizes the modal amplitude.

Both Equations (3.2) and (3.3) encompass electromechanical coupling modes, capturing the interplay between the painted FPED's deformation and its electrical performance. Further comprehensive details, including the numerical algorithm, are available in a previous publication (Patel, McWilliam, and Popov, 2014).

3.3 Computational model

3.3.1 Overview of IBM

The IBM method is utilized to construct a novel computational model in this study. Fig. 3.5 illustrates the IBM model, where the red Lagrangian points delineate solid boundaries, while the surrounding black Euler grids depict fluids. These two components interact by exchanging fluid velocity and momentum forces. Subsequently,

they extrapolate parameters from their nearest points and transfer parameters to their entire grids or nodes.

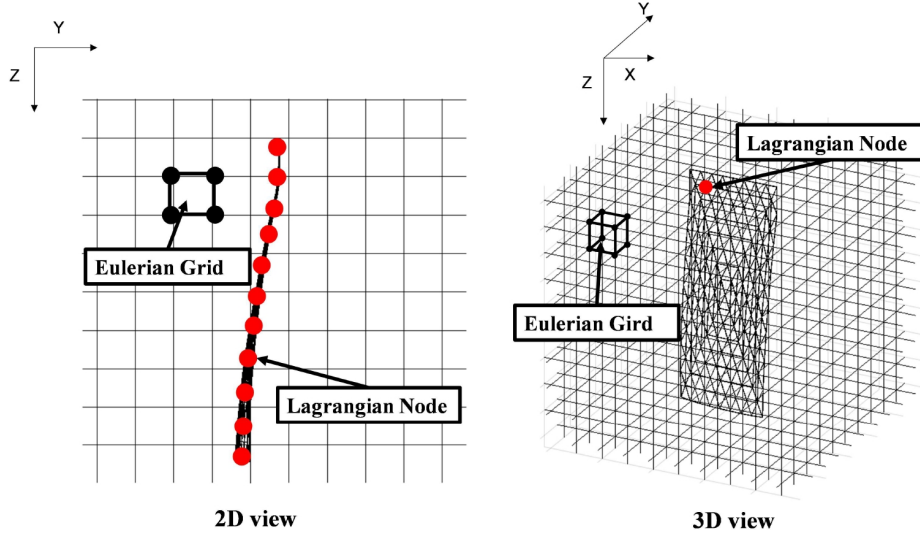


FIGURE 3.5: Model of immersed boundary method. The red Lagrangian points: the boundaries of solids. The surrounding black Euler grids: fluids. The left figure is the 2D side view of the computational model and the right one is the corresponding 3D view

3.3.2 Governing equations for IBM-based computational model

The key concept of IBM lies in converting the complex structure's boundary into forces through the application of the Navier-Stokes momentum equation, demonstrated in Equations (3.4)-(3.7).

$$\rho \left(\frac{\partial \mathbf{u}}{\partial t} + \mathbf{u} \cdot \nabla \mathbf{u} \right) = -\nabla p + \mu \Delta \mathbf{u} + \mathbf{f} \quad (3.4)$$

$$\nabla \cdot \mathbf{u} = 0 \quad (3.5)$$

Equations (3.4) and (3.5) represent the Navier-Stokes equations, where \mathbf{u} denotes velocity, ρ denotes density, μ denotes viscosity, p denotes pressure, and \mathbf{f} denotes the applied body force per unit volume of the fluid.

$$\mathbf{f} = \int_{\Gamma} \mathbf{F} \delta[\mathbf{x} - \mathbf{X}] ds \quad (3.6)$$

$$\frac{\partial \mathbf{x}}{\partial t} = \mathbf{u}[\mathbf{X}, t] = \int_{\Omega} \mathbf{u}(\mathbf{x}, t) \delta[\mathbf{x} - \mathbf{X}] d\mathbf{x} \quad (3.7)$$

Equations (3.6) and (3.7) represent the interaction equations, where \mathbf{F} denotes the force of the solid, s denotes the curvilinear coordinate attached to the solid, \mathbf{x} denotes the position of the Eulerian fluid grids, and \mathbf{X} denotes the position of the Lagrangian solid nodes. Γ and Ω are the solid and fluid domains, respectively. The delta function, $\delta(\mathbf{x}) = \delta(x)\delta(y)\delta(z)$, denotes the local character of the interaction, and x, y, z represent the positions of Eulerian fluid grids in x, y and z directions. It can be expressed as follows:

$$\delta(\mathbf{x}) = \frac{1}{h^2} \phi\left(\frac{x}{h}\right) \phi\left(\frac{y}{h}\right) \phi\left(\frac{z}{h}\right) \quad (3.8)$$

In this equation, h denotes the mesh size, and ϕ represents the four-point delta function introduced by Peskin (Peskin, 2002). Equation (3.9) delineates the boundary's force on the fluid, denoted as \mathbf{F} , expressing it as the aggregate of the elastic force \mathbf{F}_E and the bending force \mathbf{F}_B .

$$\mathbf{F} = \mathbf{F}_E + \mathbf{F}_B \quad (3.9)$$

To incorporate wave control into the immersed boundary conditions, the study introduces the Stokes wave theory. Fig. 3.6 depicts a diagram illustrating regular waves in two dimensions. The flow field's velocity can be determined through the velocity potential, accounting for the fluid point's position (y, z) . Calculations of the output voltage are performed at each time step, utilizing Equation (3.10). This equation represents the piezoelectric equation:

$$\mathbf{D} = \mathbf{d}\mathbf{T} + \varepsilon\mathbf{E} \quad (3.10)$$

Where \mathbf{D} represents the electric flux density, \mathbf{d} represents the piezoelectric stress constant, \mathbf{T} denotes stress, ε stands for permittivity, and \mathbf{E} indicates the electric field strength. Equation (3.11) denotes the correlation among charge, capacity, and voltage.

$$\mathbf{Q} = C\mathbf{V} = \frac{\varepsilon A}{t}\mathbf{V} \quad (3.11)$$

In this equation, \mathbf{Q} stands for charge, C represents capacity, \mathbf{V} denotes voltage, ε denotes permittivity, A denotes area, and t denotes thickness. Equation (3.12) depicts the association between charge and electric flux density.

$$\mathbf{Q} = \int \mathbf{D}dA \quad (3.12)$$

Given the absence of an externally applied electric field, the equation representing piezoelectric voltage in the numerical model, derived from Equations (3.10)-(3.12), can be expressed:

$$\mathbf{V} = \frac{t\mathbf{d}}{\varepsilon}\mathbf{P} \quad (3.13)$$

The pressure, denoted as P , is calculated using the force obtained from solid boundary nodes, aiding in determining the voltage at each time step with Equation (3.13).

The computational model in this research, as schematically depicted in Fig. 3.6, is segmented into six distinct parts, each with specific tasks designated by the subscript denoting the time step number. The computational sequence proceeds from part 1 through part 6, with part 1 restarting for the subsequent time step. In part 1, the process begins by interpolating the fluid velocity, \mathbf{u}_n , to the positions of solid boundary nodes, \mathbf{X}_n , using Equation (3.7). Subsequently, $\mathbf{X}_{n+\frac{1}{2}}$ is calculated. Moving to part 2, the forces acting on the solid boundary nodes, $\mathbf{F}_{n+\frac{1}{2}}$, are determined using the elastic force and bending force considering $\mathbf{X}_{n+\frac{1}{2}}$. This process aligns with Equation (3.9). Following this, Equation (3.6) is employed to extend $\mathbf{F}_{n+\frac{1}{2}}$ to compute the forces on the fluid grids, denoted as $\mathbf{f}_{n+\frac{1}{2}}$. Subsequently, in part 3,

the fluid velocity \mathbf{u}_{n+1} is calculated using $\mathbf{f}_{n+\frac{1}{2}}$ with the Navier-Stokes momentum equations (Equations (3.4)-(3.7)). Part 4 involves updating \mathbf{u}_{n+1} considering the wave velocity, defining the updated fluid velocity as \mathbf{u}^*_{n+1} , which is then interpolated to $\mathbf{X}_{n+\frac{1}{2}}$. Moving to part 5, similar to the procedures in parts 1 and 2, \mathbf{X}_{n+1} and \mathbf{F}_{n+1} are obtained. Finally, the output voltage \mathbf{V}_{n+1} is computed using \mathbf{F}_{n+1} in the final stage of the computational sequence.

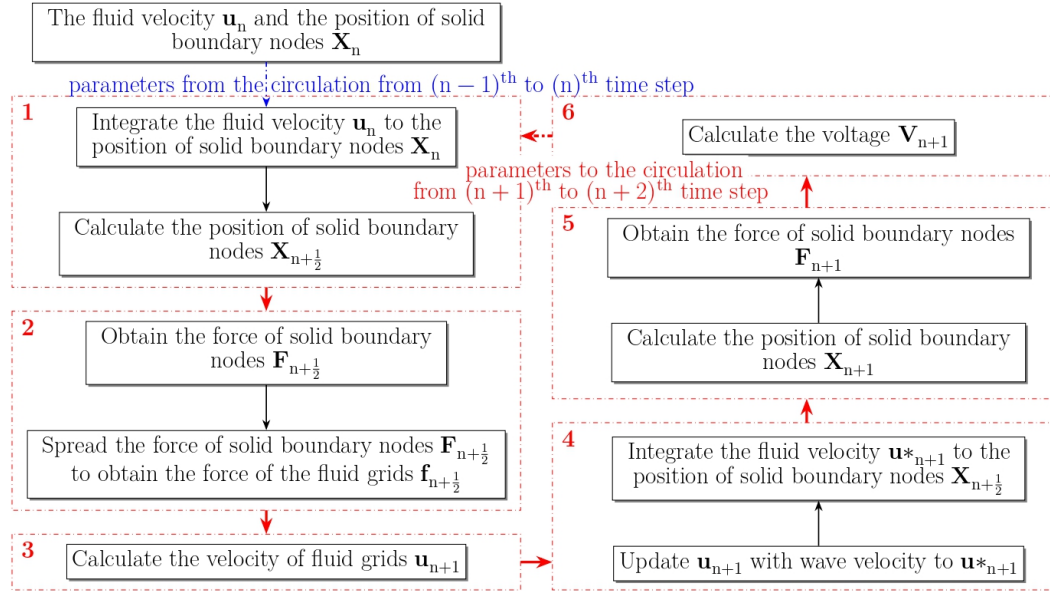


FIGURE 3.6: Schematic of the immersed boundary method

3.3.3 Initial and boundary conditions

The computational domain and initial conditions are introduced in this section. The domain size is set to $a \times a \times a$, with $a = 0.5\text{m}$. This resulted in a ratio of the domain length to the FPED length, denoted as a/L_2 , of 16.7. Waves propagated along the positive y-axis direction, while the FPED is centrally positioned within the domain. To simulate vertical waves, the device plane remain parallel to the xz plane. The solid structure is represented by 78 Lagrangian nodes for each Eulerian grid of the fluid domain.

Exploration of the wave effect is facilitated by varying the wave height and period, and the computational model allowed for adjustments to the size of the FPED device. Overall, the computational conditions are close to those observed in the experimental setup.

3.4 Results and discussion

3.4.1 Validation of theoretical and computational models

Detailed analysis is conducted on the output voltage and device positioning at a specific moment within one wave period in the section. Fig. 3.7 illustrates a case with a wave height of 0.1 m and a wave period of 0.15 s. The abscissa represents the time axis, where the left ordinate represents the output voltage, and the right ordinate denotes the wave height. In the figure, the blue and orange curves correspond to water elevation and output voltage, respectively. The dotted and solid

curves distinguish values obtained from experiments and IBM-based computations. The four diagrams from both experiments and computational simulations depict the device's position and movement at various time points. Upon the wave trough passing through the device, it moves in the opposite direction of the wave, resulting in a negative output voltage. Subsequently, around $\frac{1}{4}T$, the output voltage peaks. As the wave crest traversed the device, it moves in tandem with the wave, generating a positive output voltage. Around $\frac{3}{4}T$, the output voltage reaches its minimum value. Notably, throughout the period, the bias of the free end consistently opposed the wave direction.

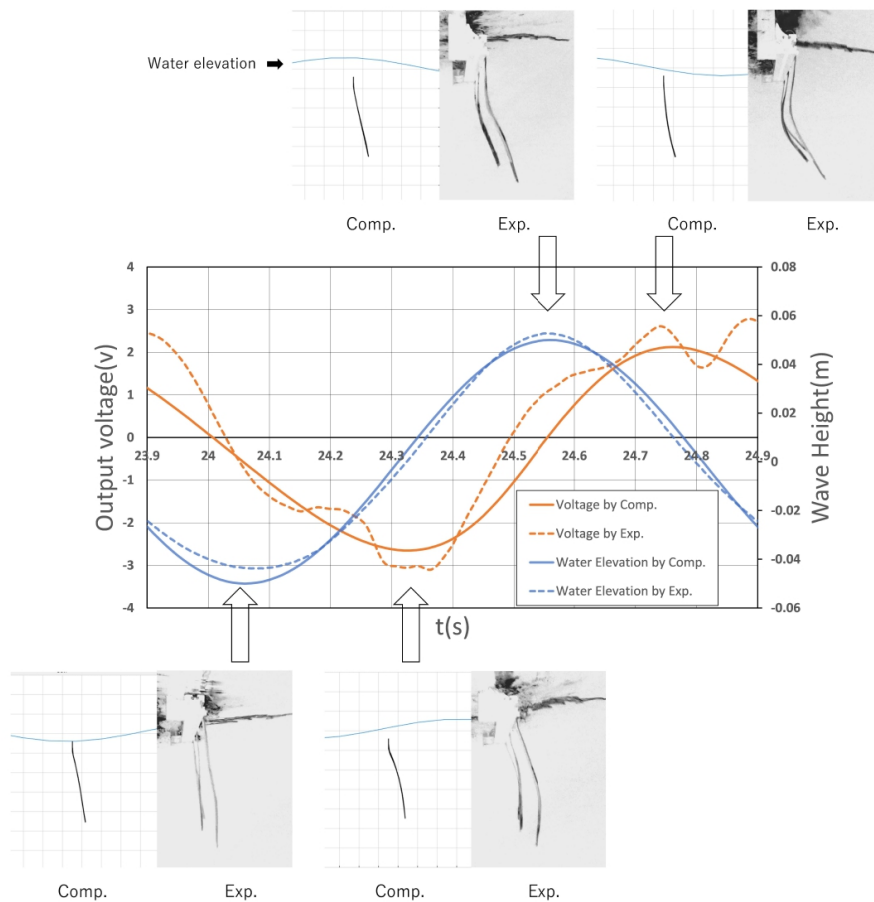


FIGURE 3.7: Effect of wave crests and troughs on the motion of FPEDs fixed by vertical cantilever support. Comp. is the computational result. Exp. is the experimental result

Comparisons were made between side views of the device's motion under varying wave heights and periods. Fig. 3.8 illustrates the impact of wave height on the device at a wave period of 1s, represented by five colors in two graphs spanning a quarter and three-quarters of a period. The dotted and solid lines distinguish the experimental and IBM-based computational results, respectively. Although exact replication of the bending shapes from experiments in computational models is challenging due to precision limitations, the trend in bending magnitudes is noticeably similar. Notably, the bending amplitude evidently escalates with increased wave steepness or height. Fig. 3.9 shows the influence of wave periods on the device

at a wave height of 0.1m, denoted by six colors across two graphs corresponding to a quarter and three-quarters of a period. The dotted and solid lines represent experimental and IBM-based computational results, respectively. While the experimental and computational motions exhibit similar trends, an exact match is hindered due to the current model's insufficient optimization for detailed spatial discretion. The trend in bending amplitude generally rises with an increasing period. However, a saturation or even a slight decrease in the bending trend occurs beyond a certain period, indicating a limiting period for substantial bending and enhanced voltage generation.

Finally, validation of the output voltage over time is presented in Fig. 3.10 at a wave period of 1s and wave height ranging from 0.05m to 0.15m. The abscissa denotes the time series with stable output voltage, while the ordinate represents the output voltage. The grey and blue curves represent the experimental and IBM-based computational results, respectively. Despite the computational model's limitations in capturing instantaneous high voltages at each wave crest, particularly in high wave steepness cases, the amplitude of the output voltage consistently rises with increasing wave steepness. While some deviation exists between computational and experimental results, the numerical modeling successfully replicates the bending tendency observed in experiments. This validates the computational model, which is instructive role in subsequent painted FPED designs.

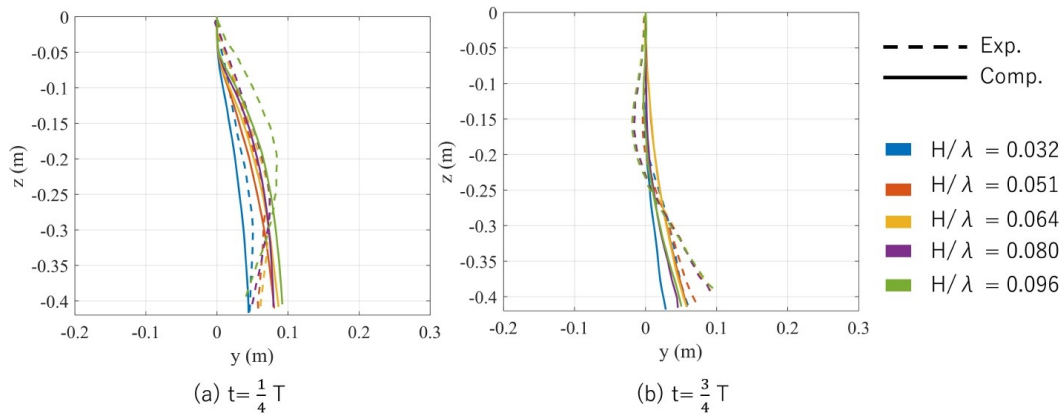


FIGURE 3.8: Effect of wave height on the motion of FPEDs fixed by vertical cantilever support

Fig. 3.11 illustrates the comparison between output voltages generated from the painted FPED using theoretical and computational methods. In Fig. 3.11a, the abscissa represents wave steepness, while the ordinate shows the maximum voltage, averaged over 10 stable continuous periods. Fig. 3.11b presents the absolute minimum voltage, averaged similarly over stable periods, and Fig. 3.11c displays the amplitude voltage, averaged over the differences between maximum and minimum values from these periods. Experimental results are denoted by red circles, IBM-based computational results by blue asterisks, and theoretical model results by green dots.

Typically, for steepness values ranging from 0.02 to 0.06, the theoretical results slightly underestimate the experimental values when $H/\lambda > 0.6$. This underestimation occurs due to the theoretical model's inability to accurately capture the strong interaction between wave motion and the deformation of the painted FPED, particularly when the maximum output voltage saturates, and strong vortices develop

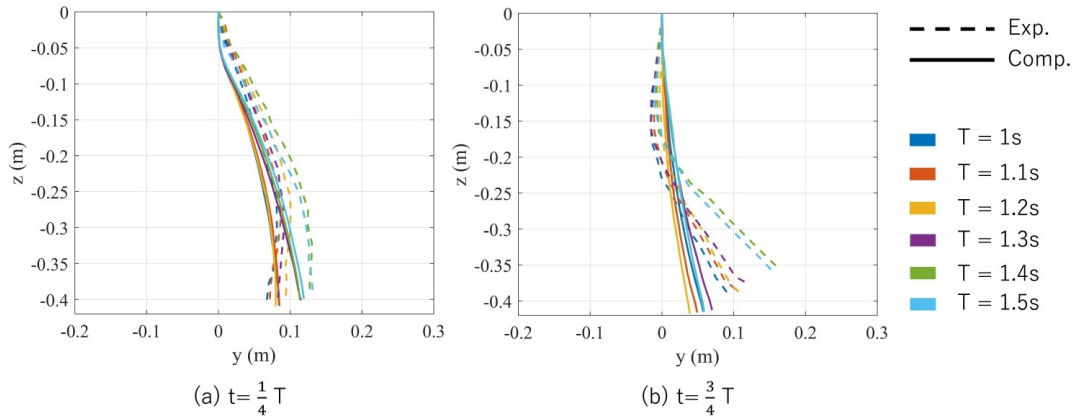


FIGURE 3.9: Effect of wave period on the motion of FPEDs fixed by vertical cantilever support

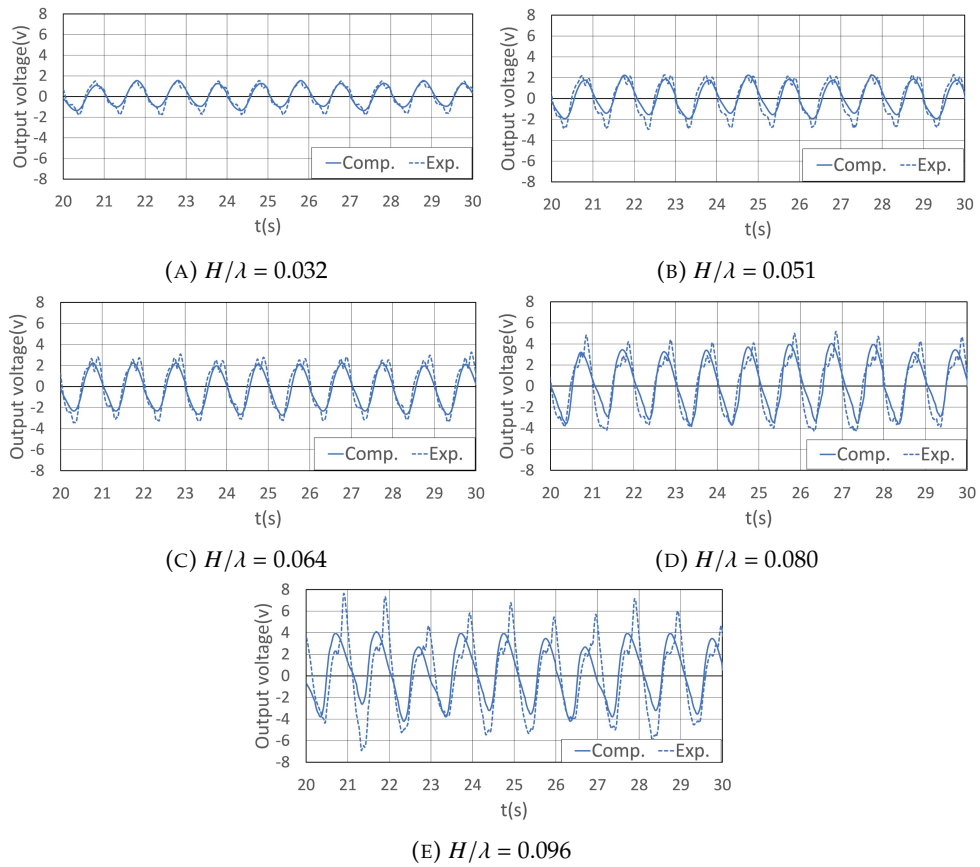


FIGURE 3.10: Time history of output voltage due to the motion of FPED 1 over 10 s under wave conditions with difference steepness.

behind the device. To analyze the theoretical model against computational and experimental values, a univariate linear regression model is employed. Although the theoretical results deviate from this regression model and intersect at the zero point, they provide insight despite the discrepancy. In contrast, the computational results align well overall with the experimental values, as depicted by the regression lines in Fig. 3.11. Hence, the computational model is a valuable and practical optimization tool to enhance the efficiency of the FPED.

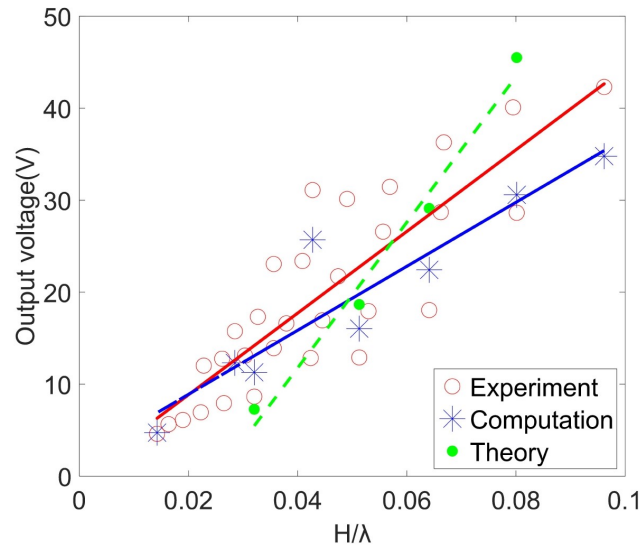
3.4.2 Effect of the support type and submerged depth

In this section, the impact of support types on the painted FPED is explored using experimental data. Fig. 3.12 presents the correlation between support type and the maximum output voltage. Notably, the maximum output voltage increases consistently with steepness across all cases, with a remarkable surge observed in the cantilever support cases compared to both-end-support and horizontal settings. In both-end-support cases, limited deformation and strain occur within the piezo material due to insufficient flexing of the entire flexible body in waves, resulting in the lowest maximum output voltage among the three support types. In contrast, the horizontal setting exhibits slightly lower output voltage compared to the cantilever, indicating that waves interact more effectively with horizontally arranged painted FPEDs than those set up vertically. Therefore, in real sea conditions, cantilever support stands out as the optimal choice due to its substantial influence on voltage output generated by waves. However, the horizontal arrangement could be considered if cantilever support is unfeasible.

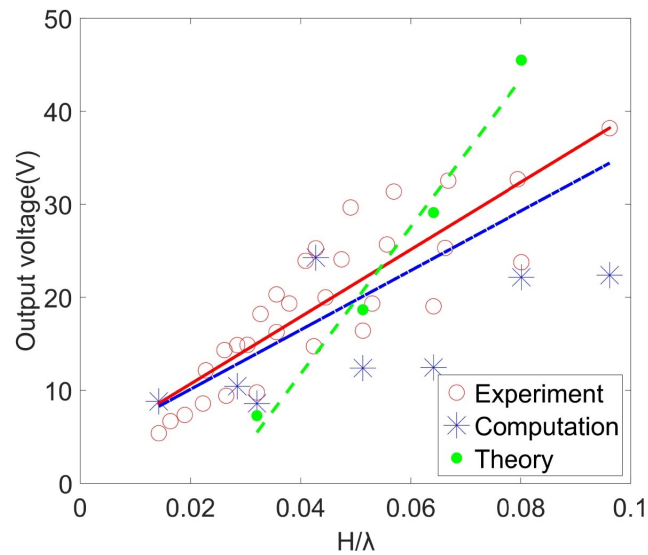
Further investigating cantilever support, the relationship between varying submerged depths of the painted FPED and maximum output voltage is explored, with d/L denoting the submerged depth normalized by the length of the painted FPED. At $d/L = 0.5$, the FPED is half submerged, while $d/L = 1.0$ indicates complete submersion. As depicted in Fig. 3.13, the maximum output voltages at $d/L = 1.0$ nearly double or triple those at $d/L = 0.5$, exhibiting an upward trend with steepness (H/λ). At full submersion ($d/L = 1.0$), substantial force prompts extensive deformation of the painted FPED. Conversely, in cases with $d/L = 0.5$, bigger deformation occurs in the lower half submerged in water compared to the upper half in the air. Hence, for real sea environments, the cantilever support with full submersion of the painted FPED is the preferable choice. Moreover, it's worth noting that the maximum output voltage might reach the maximum value and exhibit relatively scattered values around $H/\lambda = 0.6$ due to intensified wave-FPED interaction, potentially leading to wave breaking, splashing, and increased scattering around the FPED.

3.4.3 Effect of the paint thickness and AR of the painted FPED

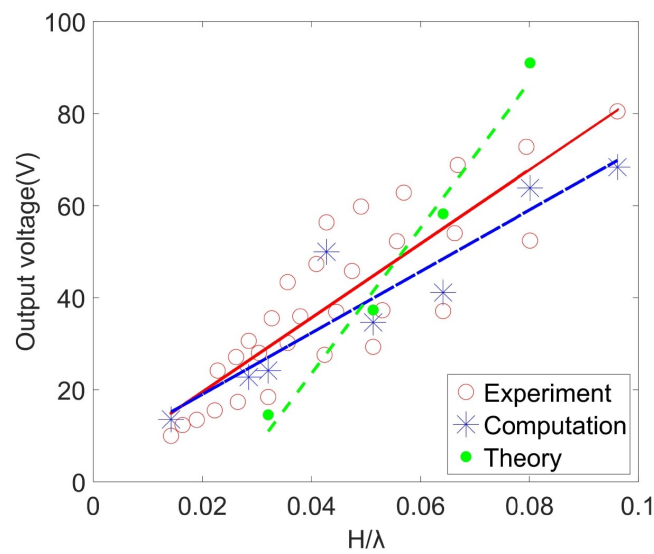
To explore the influence of the piezoelectric paint volume on the painted FPED's output voltage, Fig. 3.14 illustrates the relationship between the paint thickness and the maximum output voltage obtained from experimental analysis. The FPEDs are outfitted with piezo-material thicknesses of $50\mu\text{m}$ for FPEDs 1, 2, and 3, and $100\mu\text{m}$ for FPEDs 4, 5, and 6. A significant increase in the maximum output voltage is observed for FPEDs 1, 2, and 3 at the $50\mu\text{m}$ thickness due to a reduced rigidity of the FPEDs. This reduced rigidity allows easier deformation by wave forces. In contrast, at $100\mu\text{m}$ thickness, the maximum output voltage drops to 50% or less compared to the $50\mu\text{m}$ thickness. Consequently, determining the piezo material thickness should



(A) Maximum voltage

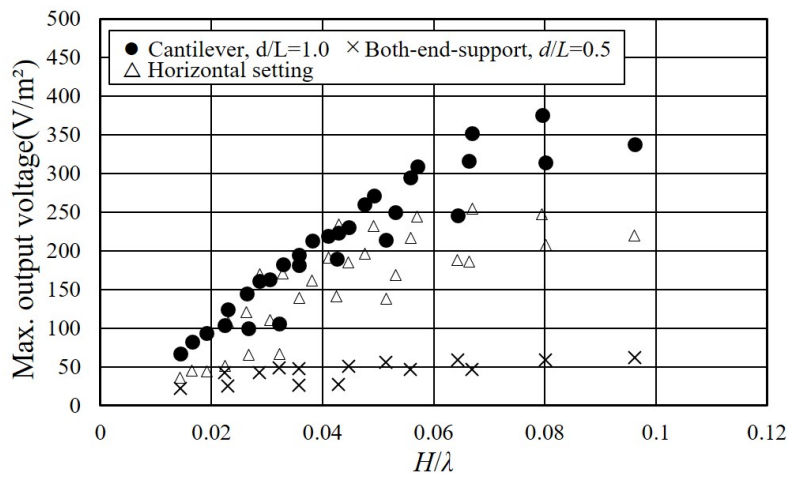


(B) Absolute minimum voltage

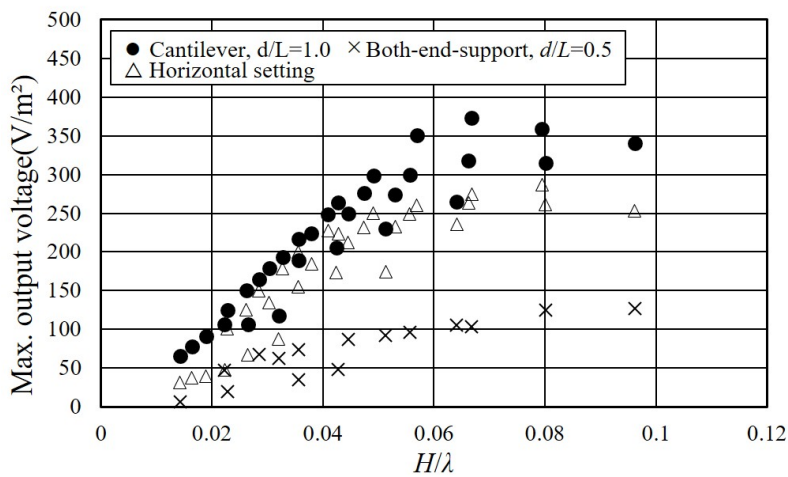


(C) Amplitude voltage

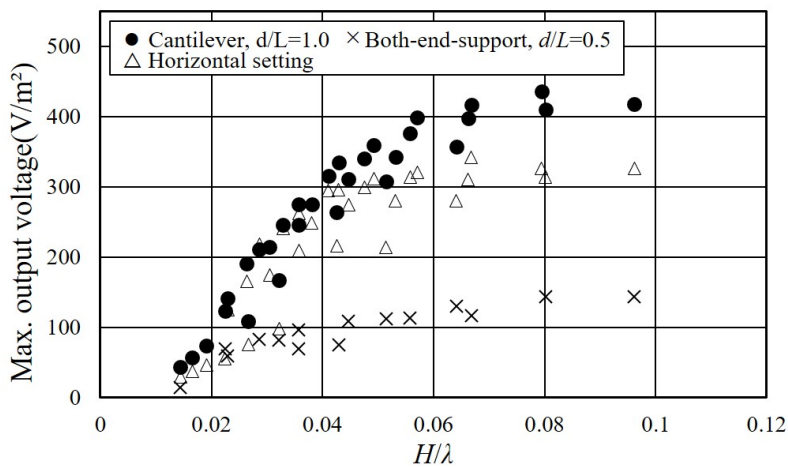
FIGURE 3.11: Comparison between computational, theoretical and experimental voltage per square meter. The red circle: the experimental results. The blue asterisks: the results of the IBM-based computational model. The green dots: the results of the theoretical models. The lines: the corresponding univariate linear regression lines.



(A) FPED1

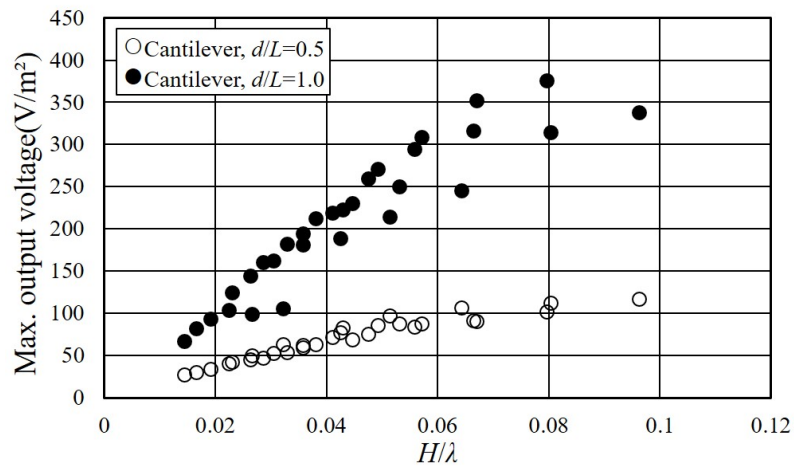


(B) FPED2

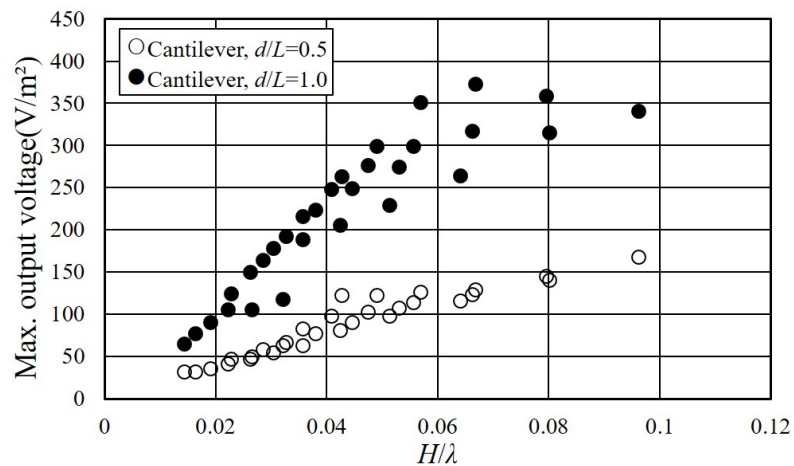


(C) FPED3

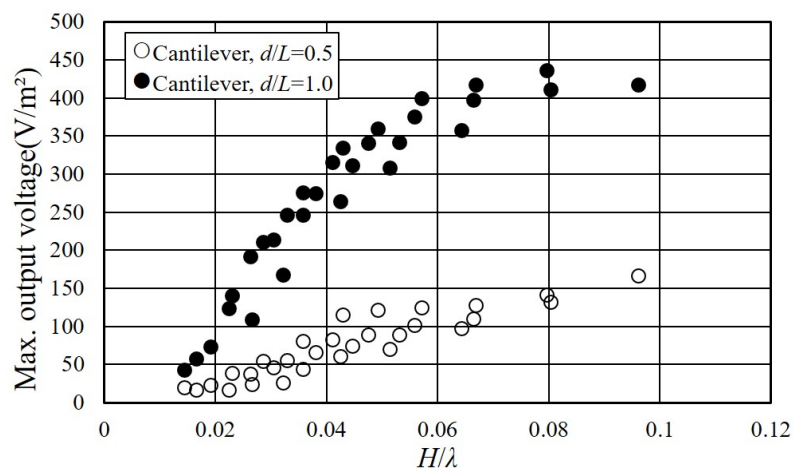
FIGURE 3.12: Relationship between the type of support for the painted FPED and the maximum output voltage. The three different support types, cantilever, both-end-support and horizontal setting, are compared for FPED1, 2, and 3. H/λ is the wave height normalised by the wave period, λ .



(A) FPED1



(B) FPED2



(C) FPED3

FIGURE 3.13: Relationship between the submerged depth of the painted FPED and the maximum output voltage. d/L indicates the submerged depth, d normalized by the length, L of the painted FPED.

consider its relative rigidity against wave forces, as higher paint thickness diminishes power generation potential due to increased rigidity.

Conversely, the AR plays a crucial role in affecting FPED output voltage. As depicted in Fig. 3.15, the relationship between the painted FPED's AR and maximum output voltage, observed through experimental measures, reveals intriguing trends. At full submersion, a relatively high maximum output voltage occurs with a smaller AR (e.g., AR=1:2). However, when the FPED is half-submerged, the maximum output voltage remains nearly constant across all ARs. This outcome suggests that the AR's impact on the maximum output voltage depends on the submerged depth (d/L). A larger AR intensifies wave forces acting on the painted FPED, leading to heightened vortex activity behind the device and increased pressure gradients between its front and back faces. Consequently, this results in amplified deformation and strain rates within the painted FPED.

3.5 Preliminary field test

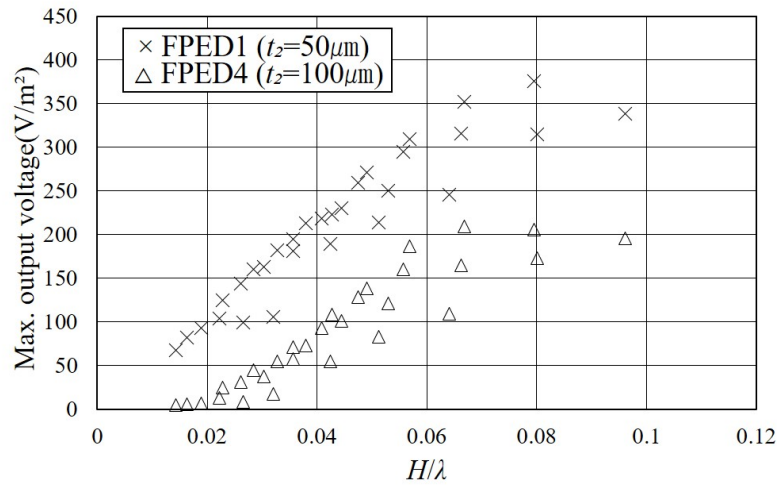
Drawing from theoretical, computational, and experimental insights obtained from the towing tank tests outlined in Section 3.1-3.3, we optimize the design of the painted FPED to prioritize reliability and durability against bending and weathering, essential attributes for real sea conditions.

In Fig. 3.16, we present the preliminary field test conducted at a site, which is located 2 km offshore in Okinawa Island. At a water depth of 30 m, a simple and provisional FAD with mooring was deployed. This operational field test span two days in January 2019. Positioned on the side frame of the FAD are the painted FPED devices including FPED1-3. The output voltage generated by these FPEDs is measured using a remote data monitoring system that comprised a data logger (A/D converter), several WiFi access devices, and a battery. The internal resistance of the data logger within the open circuit is calibrated to $1M\Omega$ for electrical power calculation using Ohm's law. Measurements are conducted over 5-minute intervals at a sampling frequency of 50 Hz for the output voltage, with a set time interval of 30 minutes. The field test span two days to accommodate the constraints pose by a battery-powered monitoring system in a marine environment.

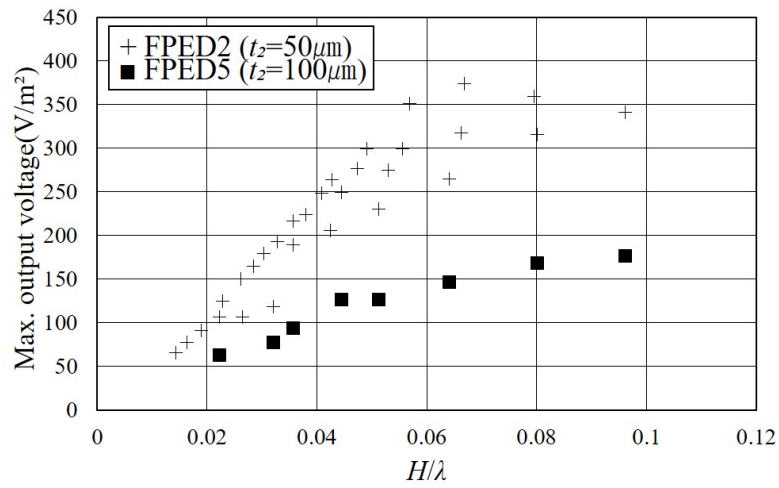
The remote data monitoring system is composed of several components: an Internet cloud-data-store, Wireless-logging-station, WiFi connecting devices (Gateway+SIM), A/D converter, Web app (GUI interface), batteries, and a monitoring laptop computer. The measured data, such as the output voltage from the FPED, are periodically uploaded to the Internet cloud-data-store at one-minute intervals. Subsequently, this data is downloaded onto the monitoring laptop computer situated on land, approximately 20 km away. Due to the constrained measurement conditions during the field test, a wave gauge couldn't be installed around the FAD. However, data on the current around the FAD was captured using a current meter, allowing for an understanding of the prevailing sea conditions in the area.

Fig. 3.17 illustrates the predominant frequency of flow velocity induced by waves in both the north-south and east-west directions, as recorded by the current meter. Notably, a peak velocity at approximately 0.25 Hz was observed, aligning with a wave period of 4.0 seconds during this particular field test.

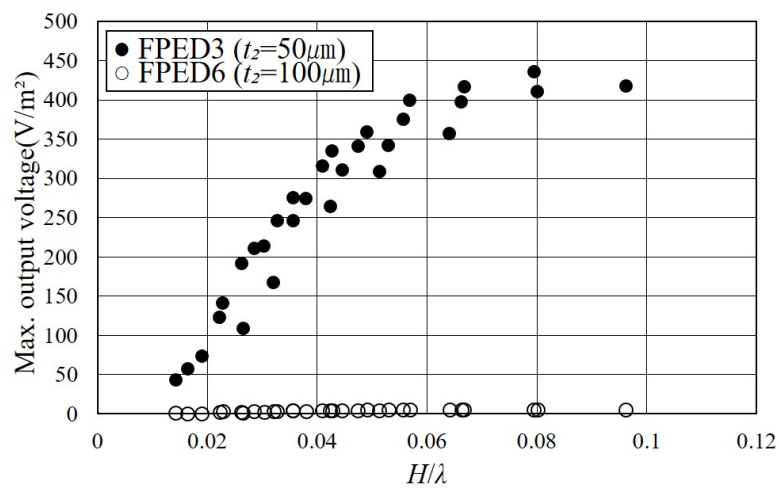
Next, the time histories of the output voltage generated by waves during the field experiment are presented in Fig. 3.18. The vertical axis represents the average output voltage calculated over 30-minute intervals from raw data. Variations in the



(A) FPED1 and FPED4

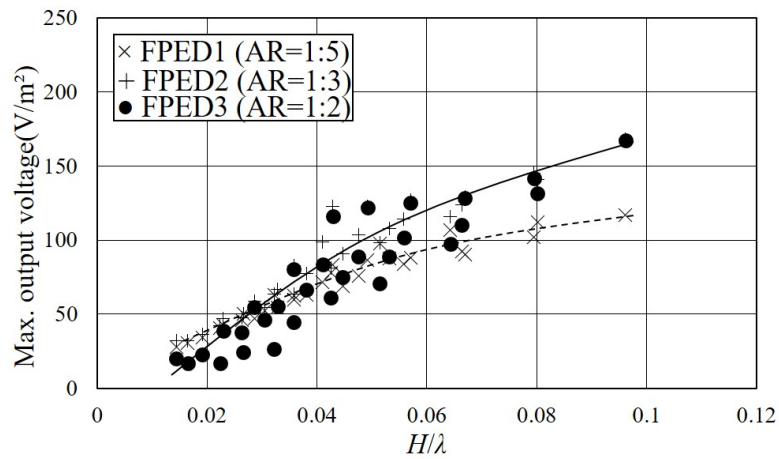


(B) FPED2 and FPED5

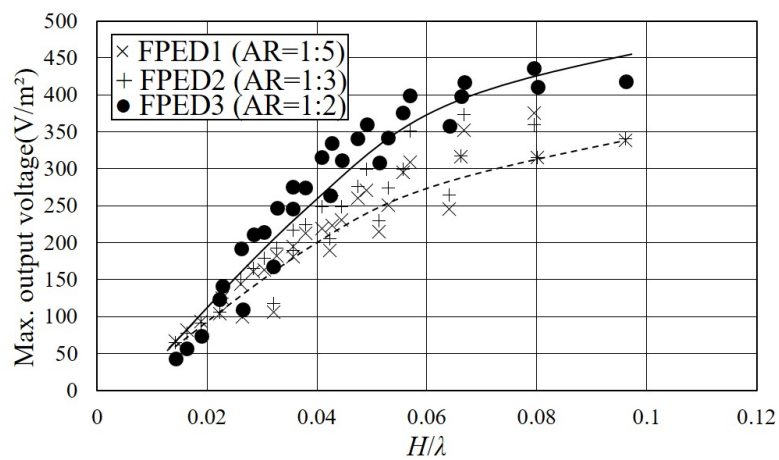


(C) FPED3 and FPED6

FIGURE 3.14: Relationship between paint thickness, t_2 (the value shown in figure 3) of the painted FPED and maximum output voltage. The output voltage at the same AR is compared between FPEDs 1 and 4, 2 and 5, 3 and 6.



(A) Half-submerged depth



(B) Full-submerged depth

FIGURE 3.15: Relationship between the AR of the painted FPED and maximum output voltage. The support type is a vertical setting with full- and half-submerged depth.

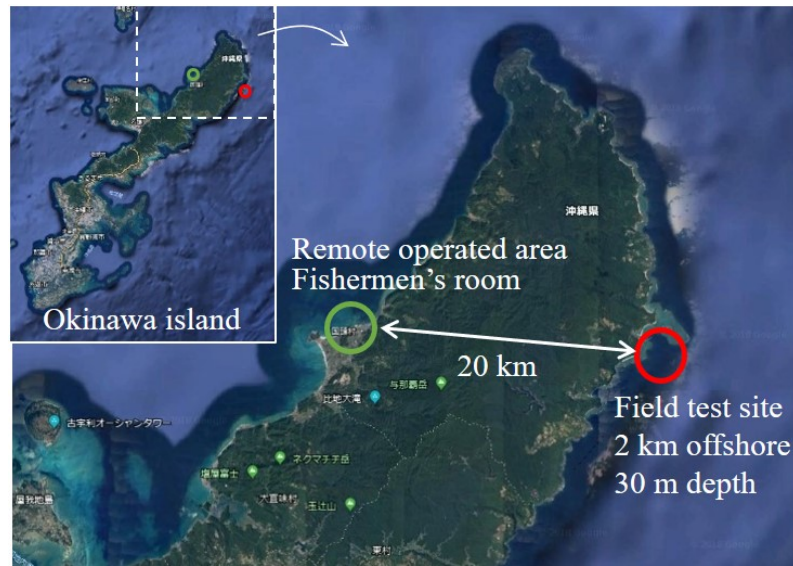
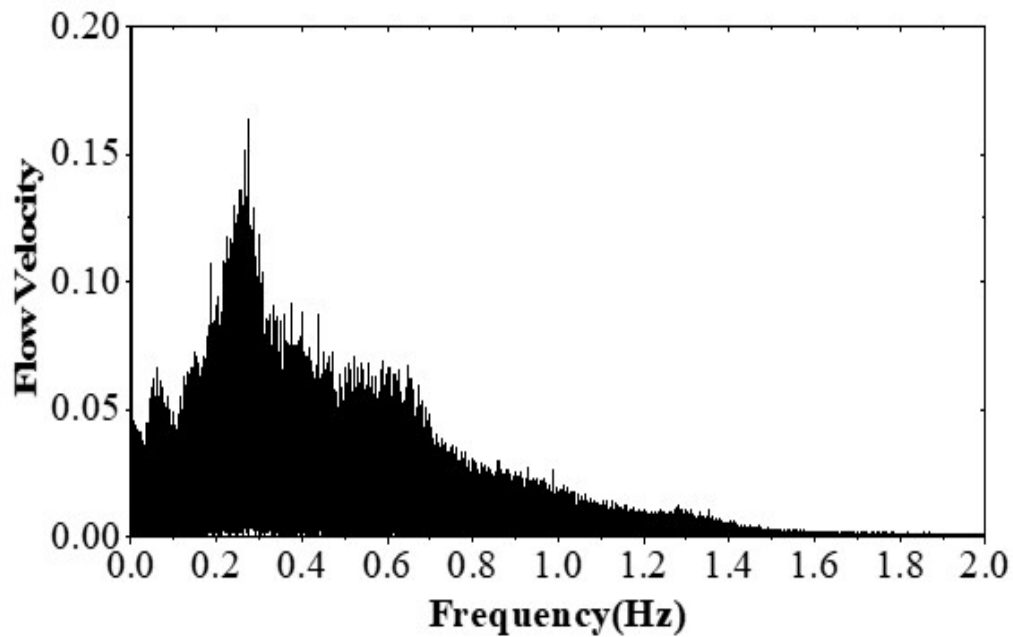


FIGURE 3.16: Location of the field test: 30 m water depth, 2 km offshore, off of the northern part of Okinawa Island, Japan. The output voltage of the painted FPED is recorded by a remote data monitoring system consisting of the data logger (A/D converter) some WiFi access devices and a battery. The remote operation station is located on land, 20 km away from the field test site.

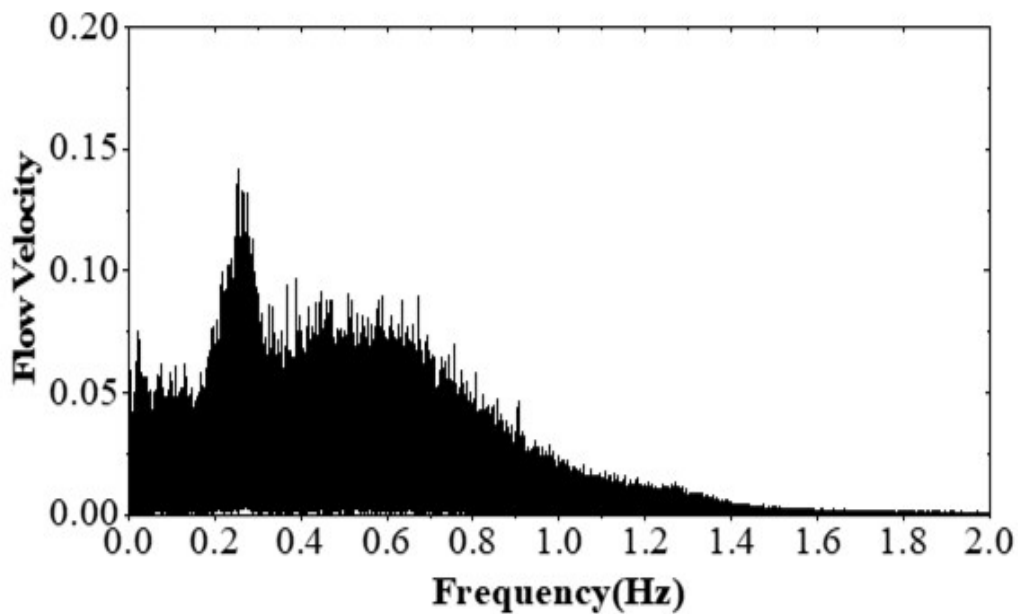
output voltage are evident throughout the entire duration of the field test. Specifically, larger wave heights on the initial day correspond to higher output voltages. In Fig. 3.19, the dominant frequency analysis of the output voltage using fast fourier transform is depicted. The peak dominant voltage occurred at approximately 0.5 Hz, corresponding to a period of 2.0 seconds. Notably, this frequency represents 50% of the wave period (4.0 seconds) observed during the field test. This periodicity aligns with the repetitive generation of output voltage triggered by the forward and backward flow induced by each wave.

Fig. 3.20 displays the correlation between the average output voltage of the painted FPED and its estimated acceleration as measured by the wave velocity meter. A notable increase in the average output voltage, particularly noticeable in FPED 3, corresponds to higher acceleration. This trend aligns consistently with the findings from controlled experiments, suggesting that larger AR result in increased deformation and strain rates for the painted FPED. In Fig. 3.21, a comparison of estimated power based on field test data is presented. The power values are standardized per unit square and hour ($w/m^2/h$). Notably, FPED 3 demonstrates the highest power output, showcasing remarkable agreement between estimated and actual values. This power output appears adequate for supporting various applications for devices on FADs and isolated islands.

For example, current studies have shown that FADs often comprise a variety of devices, which have many functions in multiple fields. Improvements in fish detection technology, such as bird radars and sonar for purse seine tuna fisheries, have increased the efficiency of fishing Torres-Irinea et al., 2014. Moreover, FADs with equipment such as remotely operated vehicles and time lapse cameras can work as automated observatories of the pelagic ecosystem and aid investigations of the distribution and characteristics of fishes G. Moreno, L. Dagorn, M. Capello, J. Lopez, J. Filmlalter, F. Forget, I. Sancristobal, K. Holland, 2016Takahashi et al., 2019Y. Baidai, L. Dagorn, M. J. Amande, D. Gaertner, M. Capello, 2020. Although FADs greatly



(A) North-South current



(B) East-West current

FIGURE 3.17: Dominant frequency of flow velocity due to waves determined by FFT. The velocity (m/s) was measured using a current metre in the field test. The flow direction is divided into north-south and east-west components.

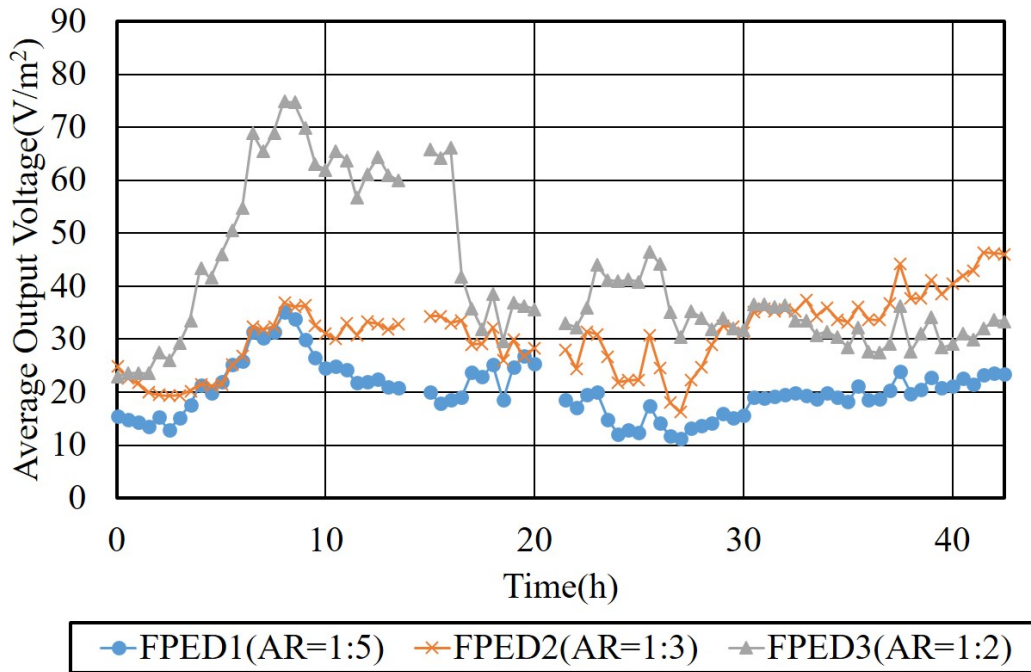
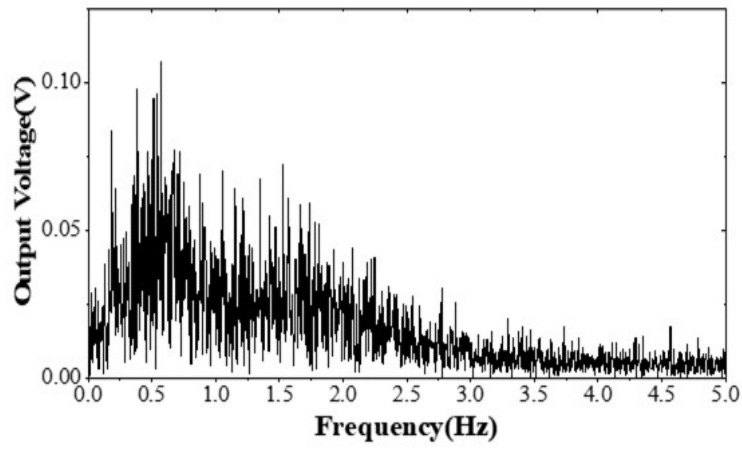


FIGURE 3.18: Average output voltage measured by the remote data monitoring system. The measuring time was 5 min with a sampling frequency of 1.0 Hz for the raw output voltage. The time interval was set to 30 min. The period of the field test was two days considering the restriction of the remote system.

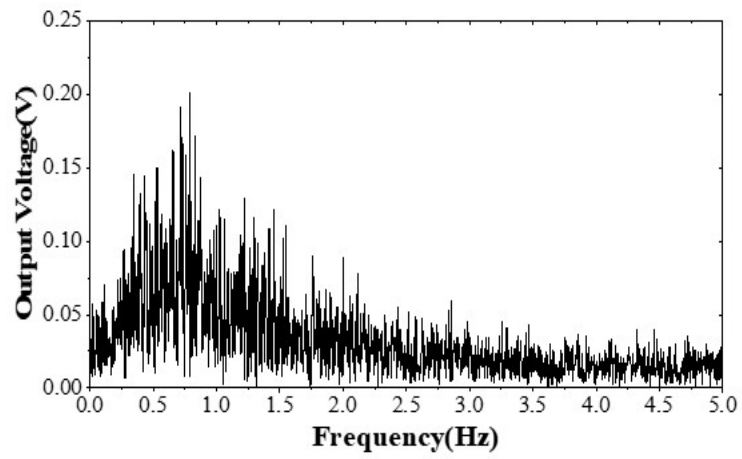
improves fishing capacity, their ecological impact is unknown. Information regarding how, where, and why FADs are used is required to assess their impact Davies, Mees, and Milner-Gulland, 2014. Banks et al. Banks and Zaharia, 2020 estimated that approximately 66% of all deployed FADs will sink over the next decade, resulting in serious ecological degradation affecting 270 km² of deep benthic habitats and 86 km² of coastal habitats. Therefore, it is necessary to use the vessel movement patterns elucidated by GPS technologies to monitor the use of anchored FADs Widyatmoko, Hardesty, and Wilcox, 2021. At the same time, equipping GPS-buoy to FADs can get remotely-sensed near-surface current data, which overcomes the high cost of the global ocean observing system and spatiotemporal coverage of GPS technologies in the tropics Imzilen et al., 2019.

3.6 Conclusions

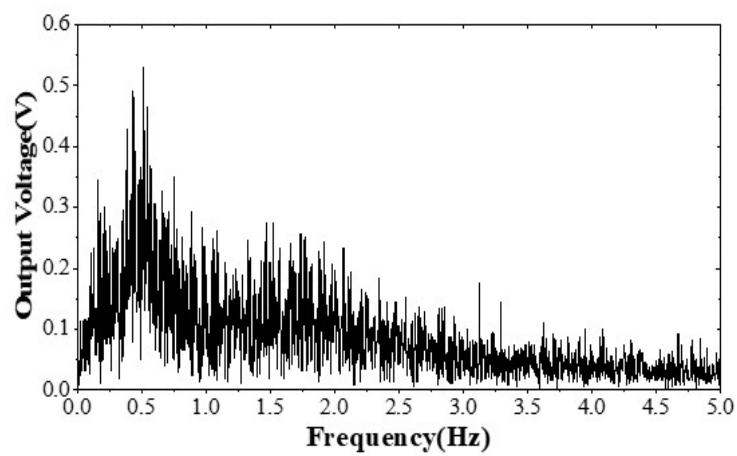
This study focuses on the development and evaluation of a piezoelectric-paint-based ocean energy harvester called FPED, integrated with FADs. Our investigation targeted key parameters influencing the electrical performance of this device under varied wave conditions. Subsequently, theoretical and computational models were developed to estimate the output voltage of the painted FPEDs and understand their interaction with oceanic waves. The selected painted FPEDs were affixed to the FAD framework to facilitate monitoring of oceanic environmental conditions, activate warning signal lights, and provide energy to both the FADs and isolated islands. Additionally, a field test conducted under authentic sea conditions involved a remote data monitoring system to evaluate extreme bending, weathering, and fatigue



(A) FPED1

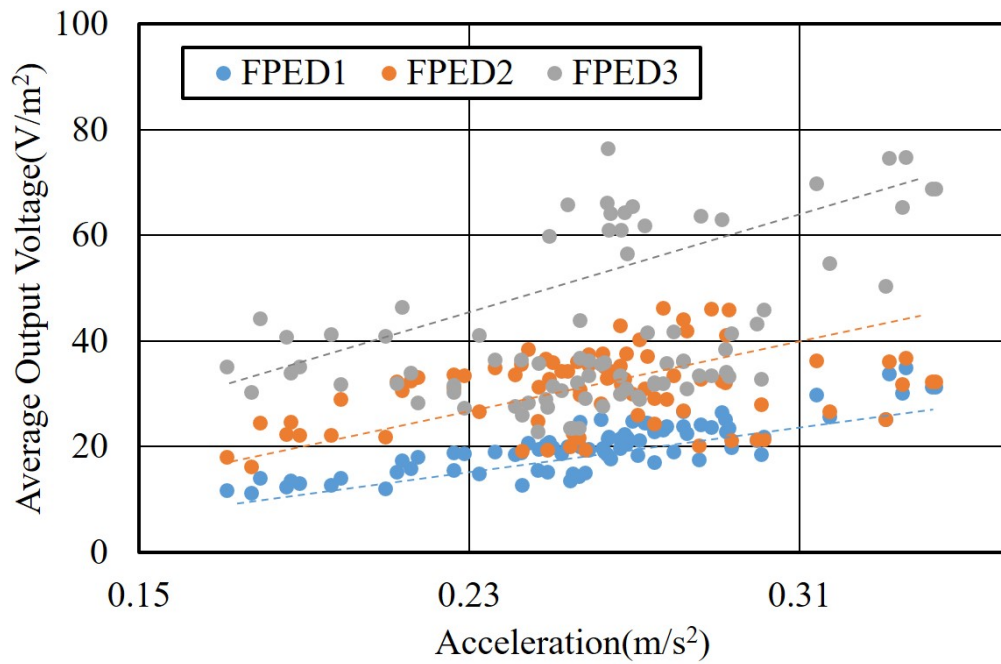


(B) FPED2

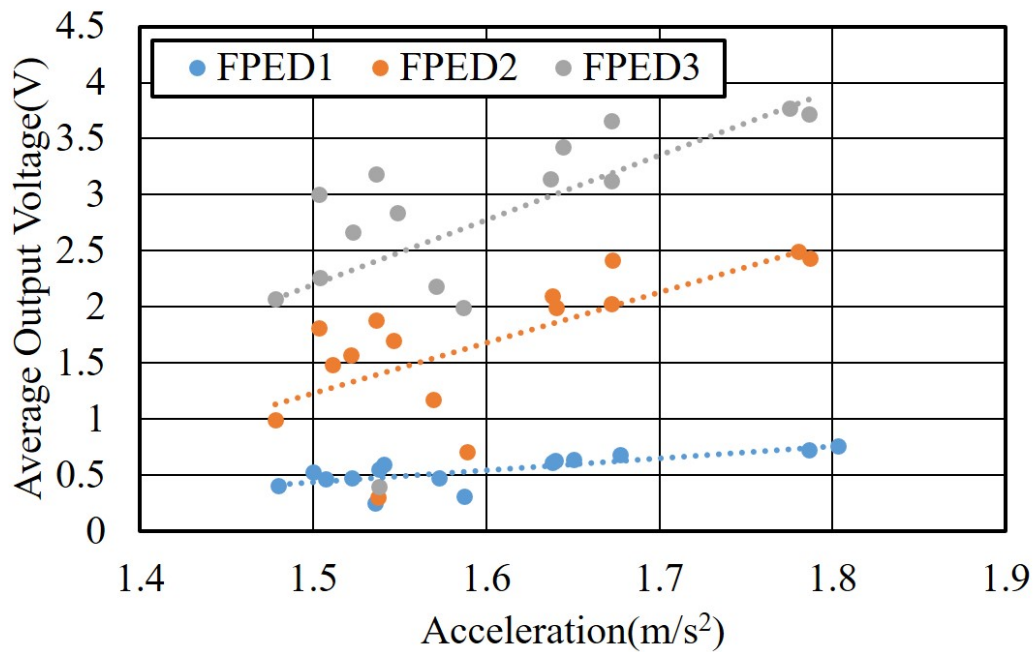


(C) FPED3

FIGURE 3.19: Dominant frequency of the output voltage due to waves, analyzed by FFT.



(A) Field test data



(B) Experimental data

FIGURE 3.20: Relationship between the average output voltage and acceleration caused by the motion of the painted FPED. A acceleration was calculated using the instantaneous output voltage due to each wave.

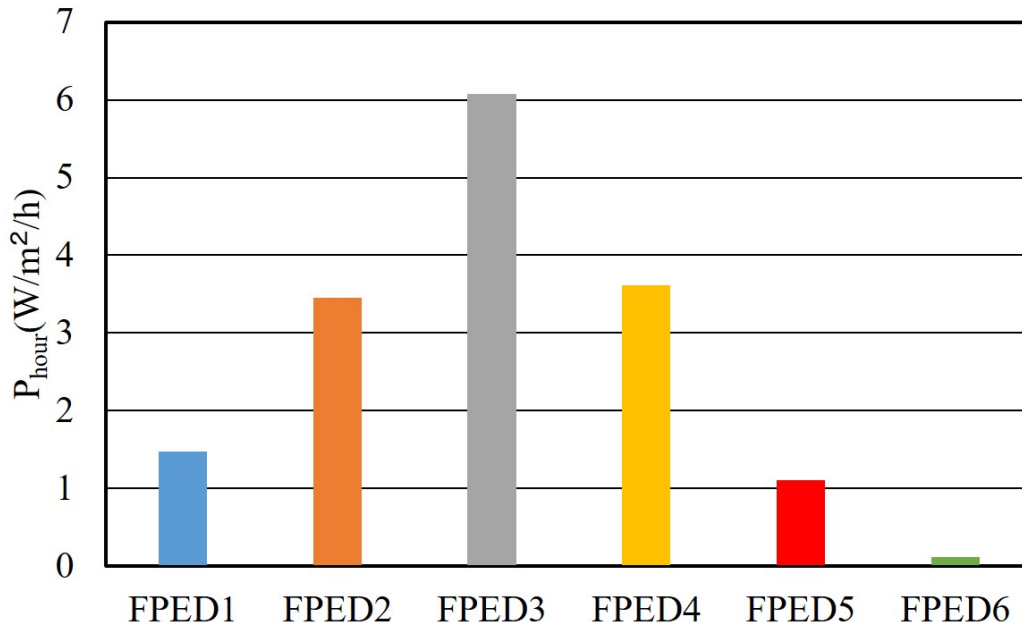


FIGURE 3.21: Comparison of the estimated power of the painted FPED based on the measured data in the field test

endurance of the painted FPED. This endeavor aimed to ensure a continuous and reliable energy supply for FAD equipment and isolated islands.

The primary findings and outcomes are outlined as follows:

- The maximum output voltage notably increases with the steepness, especially evident when utilizing cantilever support. This surge is attributed to substantial deformation and strain rates within the piezoelectric material inside the painted FPED, owing to the increased wave-induced moment.
- At a depth of $d/L = 1.0$, the maximum output voltages are nearly double or triple those observed at $d/L = 0.5$, correlating with higher wave steepness (H/λ). This substantial increase is due to pronounced deformation of the painted FPED at $d/L = 1.0$, experiencing a larger area of impact from wave forces.
- A thickness of $50 \mu\text{m}$ exhibits significantly higher maximum output voltage due to the relatively lower rigidity of the FPED. This facilitates easier deformation by waves. Hence, determining piezo material thickness should factor in its flexibility against wave-induced stresses.
- For fully submerged depths, maximum output voltage is notably high when the AR is small ($AR=1:2$).
- An IBM-based theoretical model is devised to compute Fluid-Structure Interaction directly between the FPED and waves using iterative coupled solutions. Computational results using IBM demonstrate improved accuracy compared to the theoretical model, which, although faster and more stable, aligns consistently with experimental outcomes. These methods serve as alternative tools for selecting working parameters in FPEDs and mutually complement their simulation results.

- The IBM-based computational model successfully predicts the electrical power generated by the painted FPED. Generally, computational outcomes align well with experimental results, showing an almost linear relationship between the maximum output voltage and wave steepness (H/λ).
- A customized painted FPED is designed, ensuring reliability and durability against significant bending and weathering in real sea conditions. A remote WiFi access monitoring system measures the painted FPED's output voltage, showing that the most substantial power obtained aligns with observations from experimental data.

Chapter 4

Experimental and numerical optimization of HSO-TENGs

4.1 Structure Optimization

4.1.1 Experiment setup of swinging experiment

In this section, we deeply explore the influence of various parameters on the output voltage of the HSO-TENG. Fig. 4.1 illustrates the experimental setup, depicted in Fig. 4.1(i), which can be divided into 'excitation' and 'monitor' segments. By manipulating the motor's speed, we control the swing frequency, thereby stretching and compressing the two SO-TENGs positioned on either side of the rotatable hammer. Fig. 4.1(ii), 4.1(iii), and 4.1(iv) present three snapshots capturing the movement of the SO-TENGs on the swing machine. Finally, both SO-TENGs are linked to the oscilloscope via separate wires, facilitating real-time electrical power transmission. The output voltage is recorded and monitored on a laptop.

4.1.2 Results and discussion

In Fig. 4.2, the parameters utilized for optimization are shown, with comprehensive results expounded in Fig. 4.3 through Fig. 4.7. Here, M signifies the weight of the magnet mass, L represents the hammer's height, D denotes the length of the swing arm, and θ represents the maximum swing angle. To simulate its performance along the wave direction, two symmetrical SO-TENGs, identified as Part C and Part D, are strategically positioned along the swing's trajectory on both sides of the hammer during the swinging experiment.

This section presents the filtered results. In Fig. 4.3, the output voltage versus time curve is depicted, encompassing a swinging frequency range from 0.275 to 1.45 Hz. The plot distinctly illustrates two waveform (Part C and D) showing ordered and opposing voltage data. Notably, their amplitudes consistently increase in consistent with the frequency. This trend illustrates the remarkable sensitivity of the HSO-TENG to swing frequency.

Fig. 4.4 displays the absolute average voltage plotted against varying frequencies, incorporating three different maximum swing angles. Clearly, there's a notable increase in output voltage with higher swing angles. The parameters highlighted in Fig. 4.3 and 4.4—swing frequency and maximum swing angle—correspond to wave frequency and wave height, respectively. This correlation shows the HSO-TENG's potential for wave monitoring applications.

Then, detailed investigations about the influence of internal inertia, factors D and L are based on the analysis mentioned above, while analyzing the impact of the

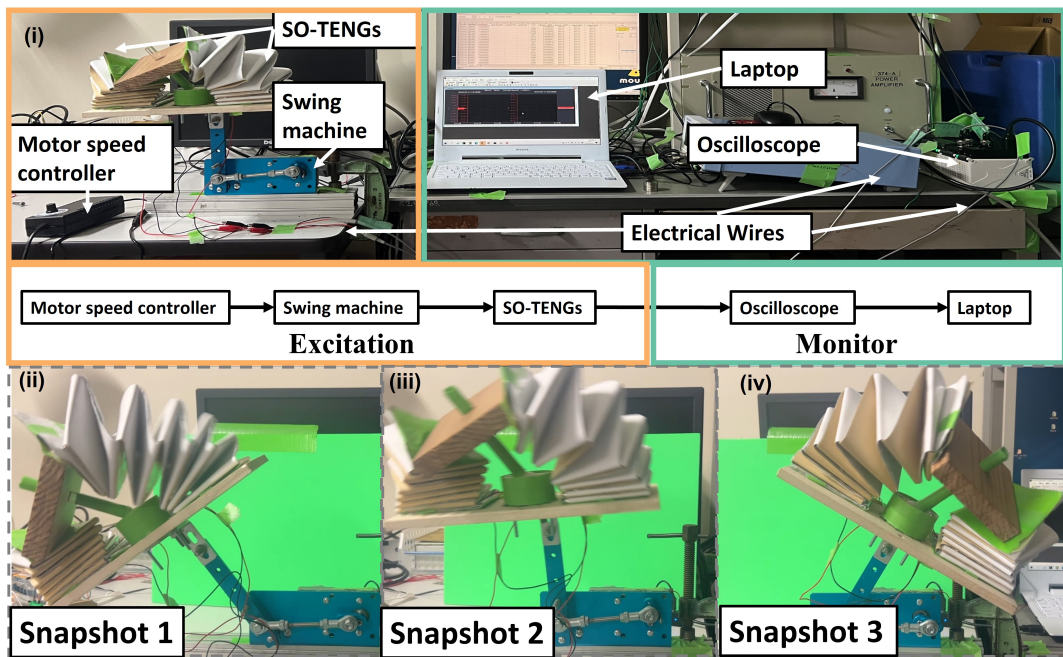


FIGURE 4.1: Swinging experimental setup, flow chart(i) and three Snapshots during experiments(ii-iv).

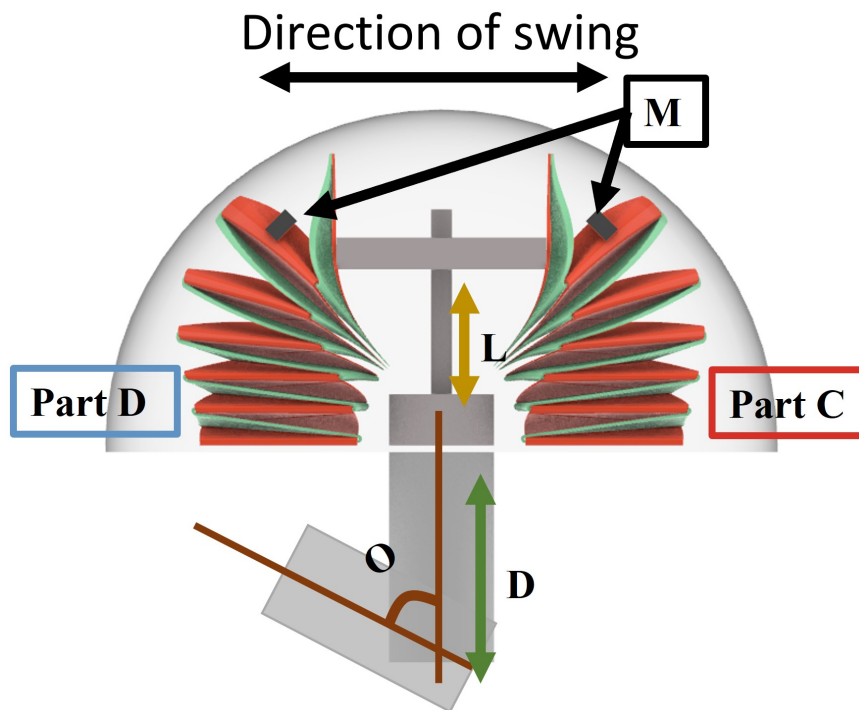


FIGURE 4.2: Schematic of Parameters selected for optimization. (The SO-TENGs, Part C and Part D, are positioned along the direction of swing)

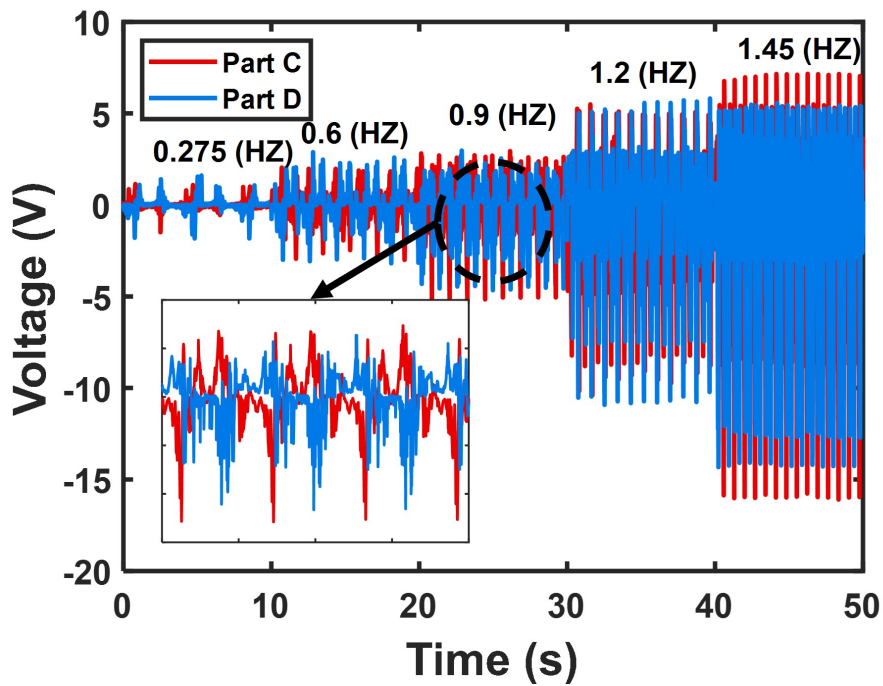


FIGURE 4.3: Output voltage versus time curve under different swing frequencies.

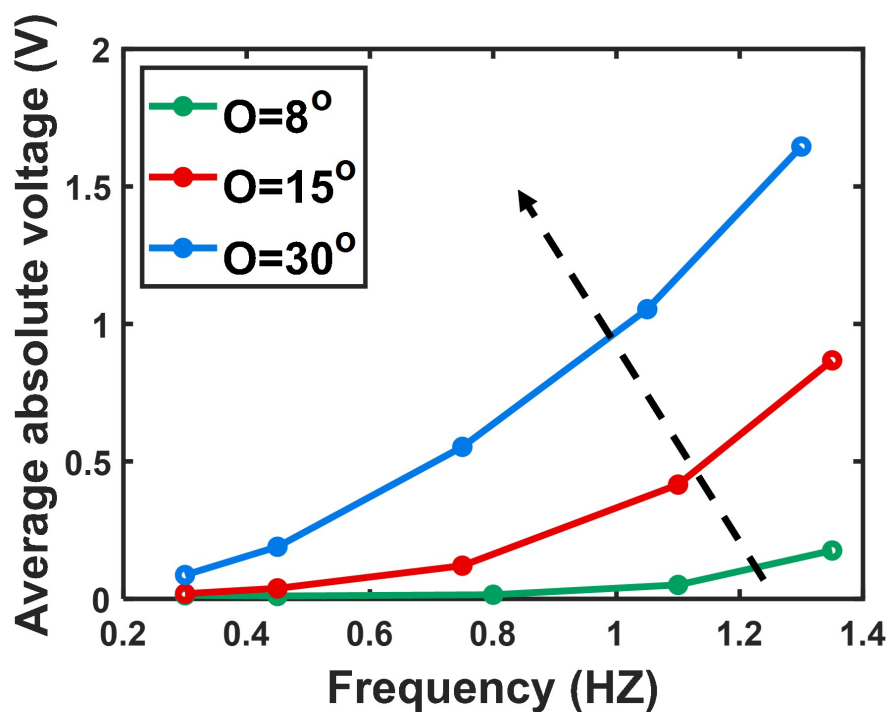


FIGURE 4.4: Absolute average voltage versus frequencies under varying maximum swing angles.

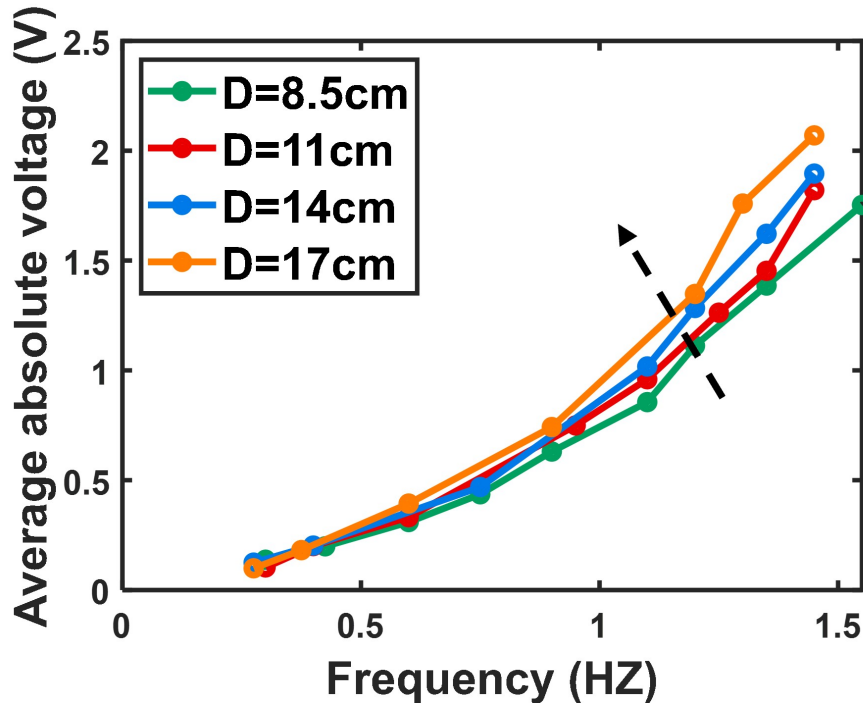


FIGURE 4.5: Absolute average voltage versus frequencies under varying lengths of swing arm.

external center of gravity using factor M . Figures 4.5 - 4.7 illustrate that augmenting D , M , and L can significantly boost power generation performance at a specific frequency.

To confirm the potential to power additional sensors, both SO-TENGs are rectified and connected in parallel on either side of the capacitor, as depicted in Fig. 4.8. The charging curve demonstrates that in just 100 seconds, a $47\mu F$ capacitor can be charged to 4V, offering compelling evidence of the HSO-TENG's capability to power supplementary sensors.

4.2 Performance of HSO-TENG in uni-direction wave tank

In this section, numerical models are built to find the suitable fixed conditions of the HSO-TENG when monitoring wave conditions. To validate the reliability of the numerical model, experimental setup and results are introduced at first, which is depicted in Fig. 4.9-5.1.

4.2.1 Experiment setup of uni-direction wave tank

To improve the practical application of the HSO-TENG, we've introduced an additional waterproof layer along with selecting optimal parameters as detailed in Section 4.1. The selected parameters for D , M , and L are set to 17cm, 540g, and 6cm, respectively. It's noteworthy that L is set at 6cm, not 7cm, to avoid friction during the swinging process.

The experimental setup overview is divided into two main sections, including the excitation and monitoring parts. In Fig. 4.9, the excitation setup displays the HSO-TENG positioned at the center of the wave tank, with its bottom closely situated to the still water level.

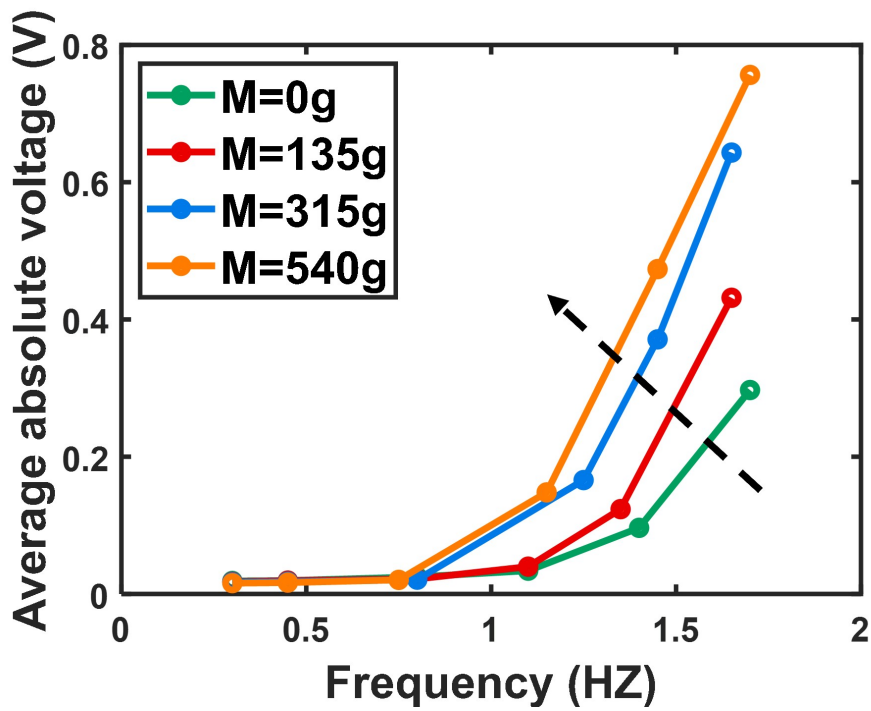


FIGURE 4.6: Absolute average voltage versus frequencies under varying weights of magnet mass.

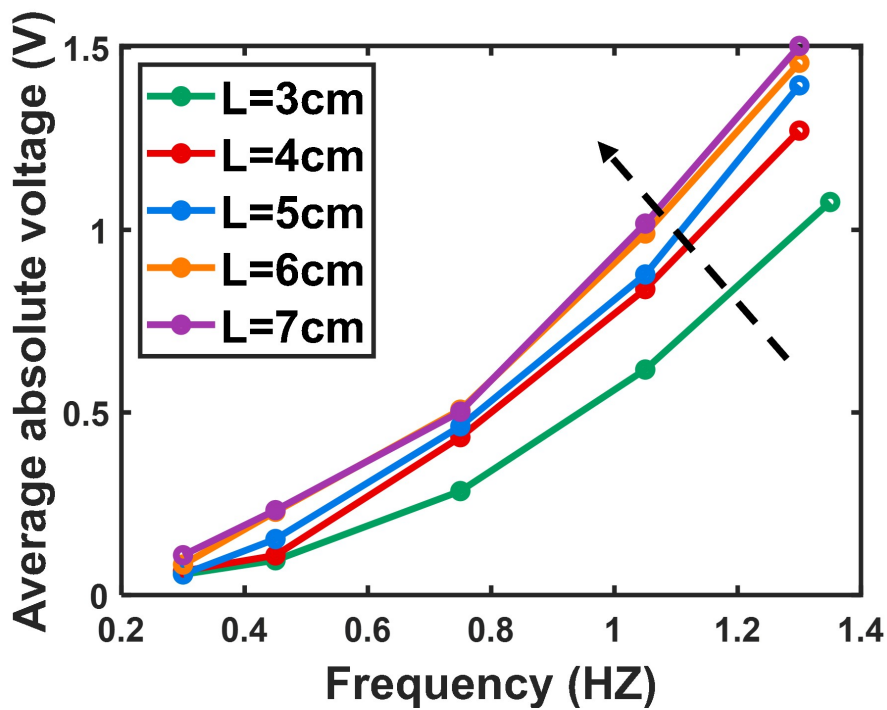


FIGURE 4.7: Absolute average voltage versus frequencies under varying heights of the hammer.

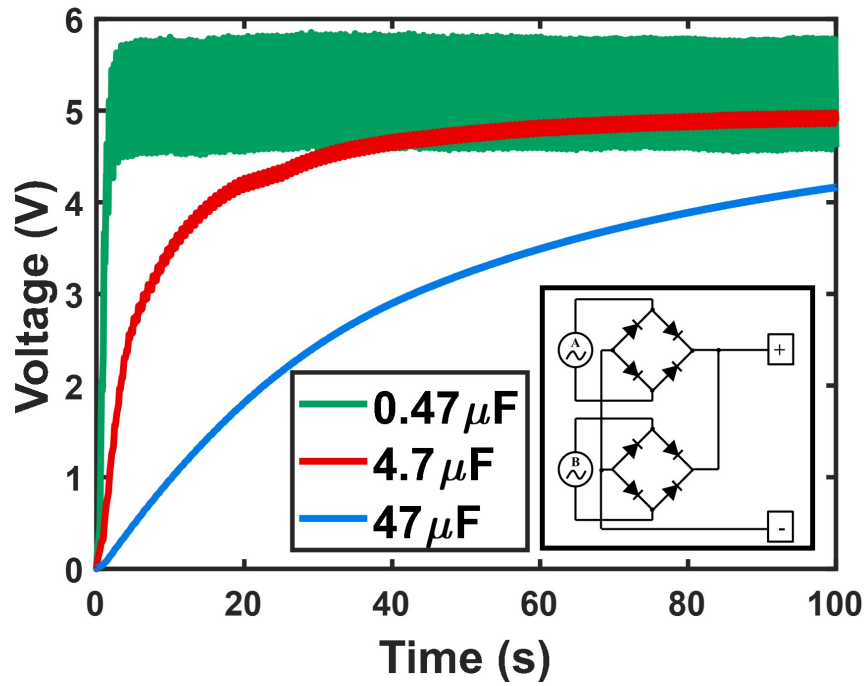


FIGURE 4.8: Charging curves using different capacitances.

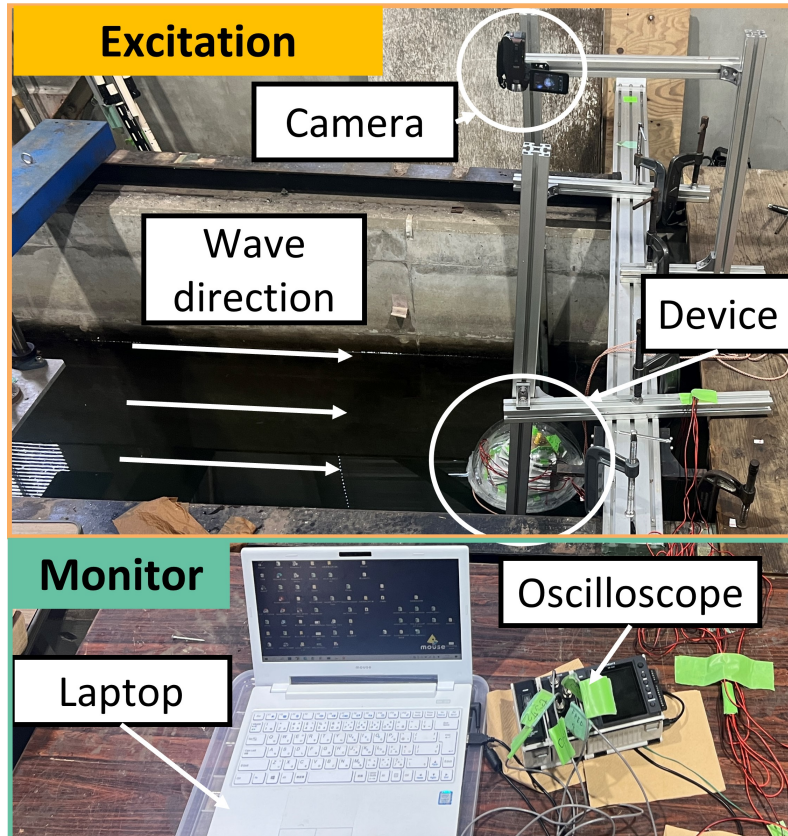


FIGURE 4.9: Overview of experimental uni-direction wave tank.

TABLE 4.1: Parameters of the wave tank in the experiment

| | |
|---------------|-------------------------------------------------------|
| Dimensions | 43m x 1.2m x 2.0m (Length x Breadth x Water Depth) |
| Wave period | 0.8s, 1s, 1.2s, and 1.5s |
| Wave height | 40, 60, 80, and 100mm |
| Driving motor | 6.17 KW x 1 |

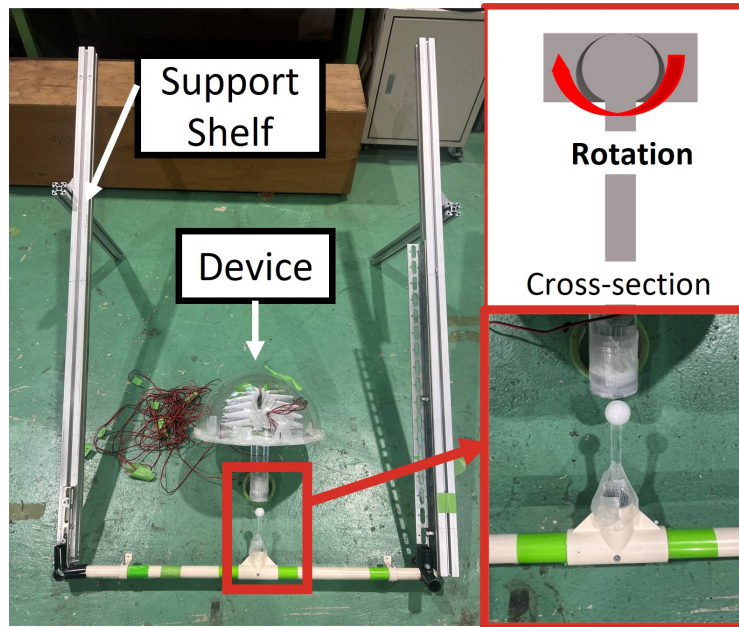


FIGURE 4.10: The connection part between the device and the support shelf.

The experimental parameters of the wave tank are detailed in Table 4.1. Throughout the experiments, the HSO-TENG is affixed to a support shelf. Fig. 4.10 depicts the connection between the HSO-TENG and the support shelf, utilizing a rotational structure similar to that shown in Fig. 4.11. Additionally, a camera is strategically positioned above the HSO-TENG to capture its motion, enabling comparison with the experimental outcomes. When the HSO-TENG faces upstream, meeting the incoming waves, the voltage generated by its four distinct SO-TENGs (identified as 'Part A', 'Part B', 'Part C', and 'Part D' in Fig. 4.11) is transmitted via four wires to an oscilloscope within the monitoring section. Subsequently, a laptop in Fig. 4.9 is employed for data analysis and ongoing monitoring.

4.2.2 Numerical conditions in uni-direction wave tank based on SPH method

Then, the numerical deep-water wave tank setup is depicted in Fig. 4.12-4.14. Fig. 4.12 offers both top and side views of the wave tank, and a detailed breakdown of its parameters is provided in Table 4.2. Specifically, the wave tank employs a flap-type wave generator, a designated water depth, and a damping zone to simulate deep-water wave conditions. In Fig. 4.13, the numerical HSO-TENG is positioned at the center of the uni-directional wave tank. Here, the SO-TENGs are represented using four simplified spring components, designed to capture their elastic properties. Typically, an origami spring is crafted from thin elastic plates connected via rotating straight line hinges. Hence, the primary source of the restoring force in the

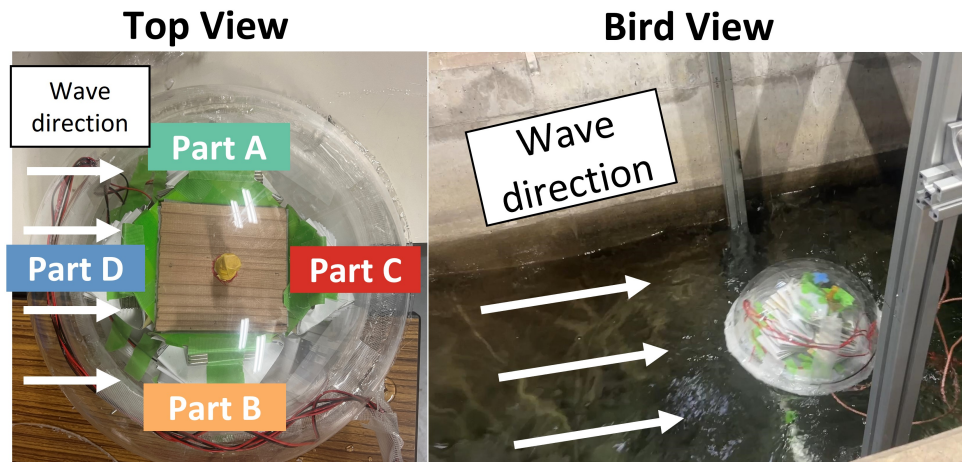


FIGURE 4.11: Illustration of four parts in one HSO-TENG device and its working details in wave tank. (Part C and D stretch and compress along the direction of the wave while Part A and B move perpendicular to the direction of the wave).

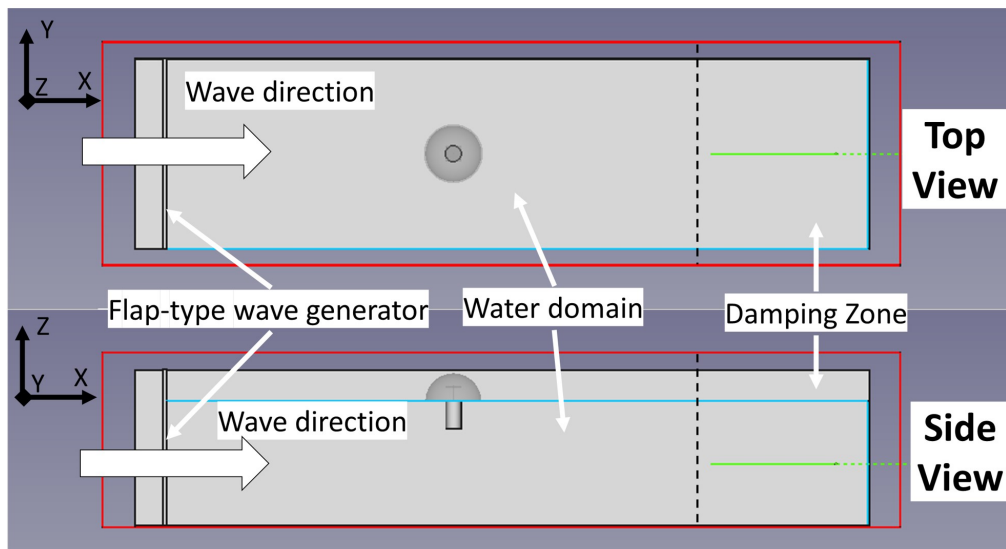


FIGURE 4.12: Top view and side view of numerical wave tank (including flap-type generator, water domain and damping zone).

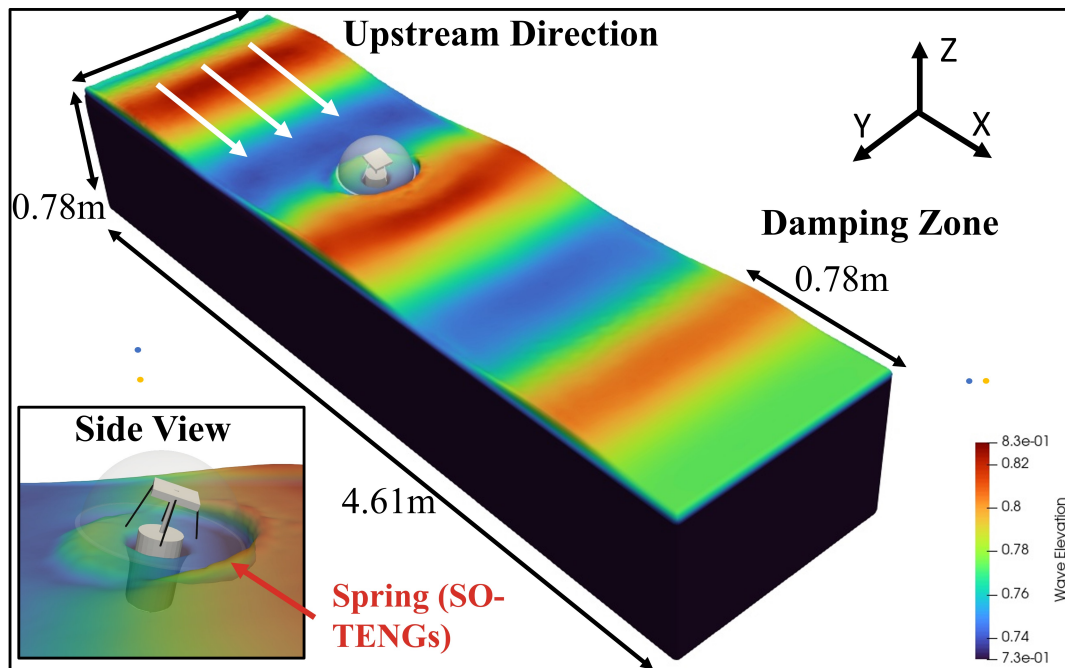


FIGURE 4.13: Bird view of numerical wave tank and side view of the HSO-TENG.

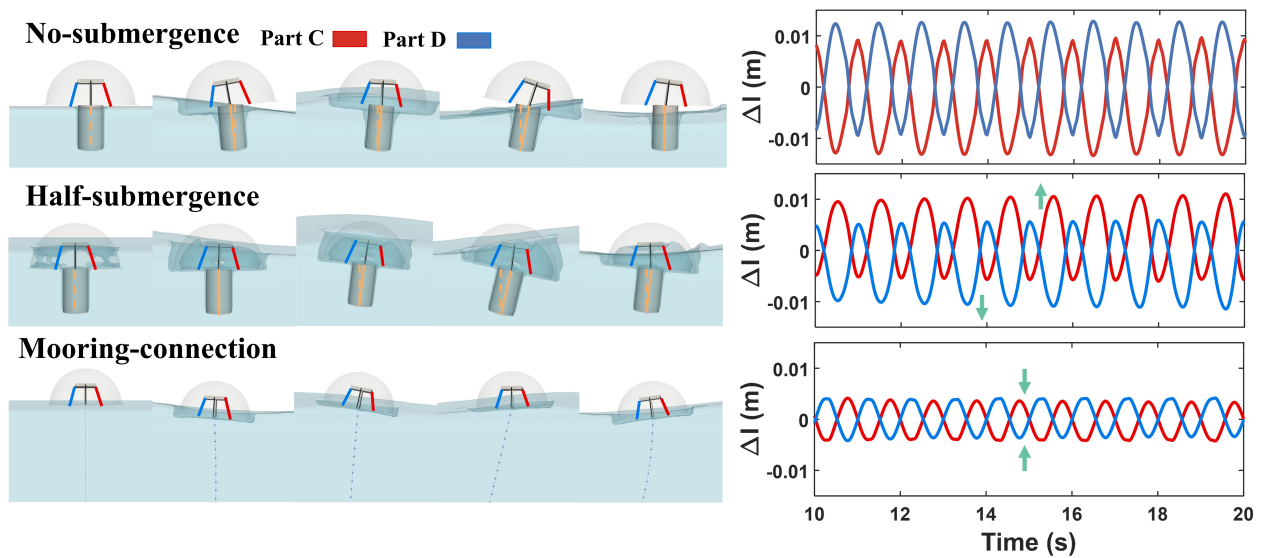


FIGURE 4.14: Comparison between the motions of the HSO-TENG and the change in length(Δl) of the springs under the three fixed conditions. (Non-submergence: the bottom of the hemisphere is flush with the horizontal level and the whole device can rotate around the fixed bottom of the cylinder. Half-submergence: half of the hemisphere is submerged in water and the whole device can rotate around the fixed bottom of the cylinder. Mooring-connection: the bottom of the hemisphere is flush with the horizontal level and its bottom is connected to the bottom of the wave tank through mooring.

TABLE 4.2: Setting parameters of the numerical uni-direction wave tank.

| | | |
|------------------|--------------------------|-----------------------------|
| Scale parameters | Distance of Particles | 0.01m |
| | Number of Particles | 4309646 |
| | Time of simulation | 15s |
| | Time step | 0.025s |
| | Tank depth | 0.78m |
| | Tank width | 1.2m |
| | Tank length | 4.61m |
| | Length of damping zone | 0.78m |
| | Diameter of the HSO-TENG | 0.37m |
| Wave parameters | Wave height | 40mm, 60mm, 80mm, and 100mm |
| | Wave period | 1s |

origami spring is predominantly derived from the bending and twisting elasticity of these individual plates. For further insights into the elastic responses of the origami spring, reference (Yoneda, Matsumoto, and Wada, 2019) provides relevant testing data

4.2.3 Selection of fixed conditions based on numerical model

This section investigates three distinct boundary conditions (no-submergence, half-submergence, mooring-connection) in the numerical model, as depicted in Fig. 4.14. The aim is to identify the most suitable condition among them. Alongside these conditions, the motions of the HSO-TENG in one period and the length variations of the springs over ten seconds are also presented for comparison. The comparison reveals that under the half-submergence condition, the HSO-TENG rotates towards the streamwise direction, causing insufficient compression in Part C and excessive tension in Part D. Conversely, the mooring-connection condition illustrates that the HSO-TENG follows the wave, resulting in a notable reduction in the compression and stretching range of the internal springs, accounting for only half the range observed in the no-submergence condition. Consequently, based on these observations, the subsequent experiments select the no-submergence fixed condition as the most suitable choice.

4.2.4 Validation of numerical model

In this section, we compare the numerical motion of the HSO-TENG under the no-submergence condition with the experimental data. To achieve this comparison, we track and analyze the trajectories of two key points—the top point of the hemisphere (indicated by the blue marker) and the hammer (indicated by the yellow marker)—as illustrated in Fig. 4.15 and Fig. 4.16. The experimental data is obtained using a camera positioned as shown in Fig. 4.9, capturing a top-view video. Image recognition software extracts the motion trajectories of these points from the videos, allowing us to calculate the distances moved by the blue and yellow points using the measured-to-pixel distance ratio.

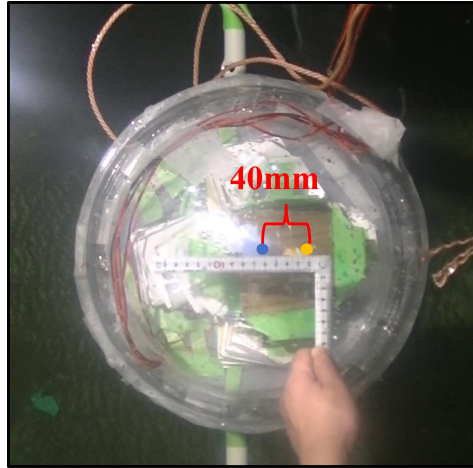


FIGURE 4.15: Validation points in experiment.

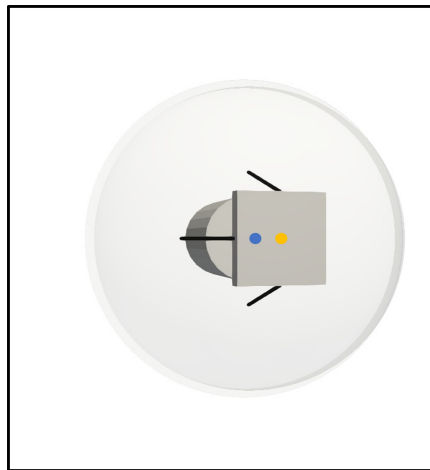


FIGURE 4.16: Validation points in numerical simulation.

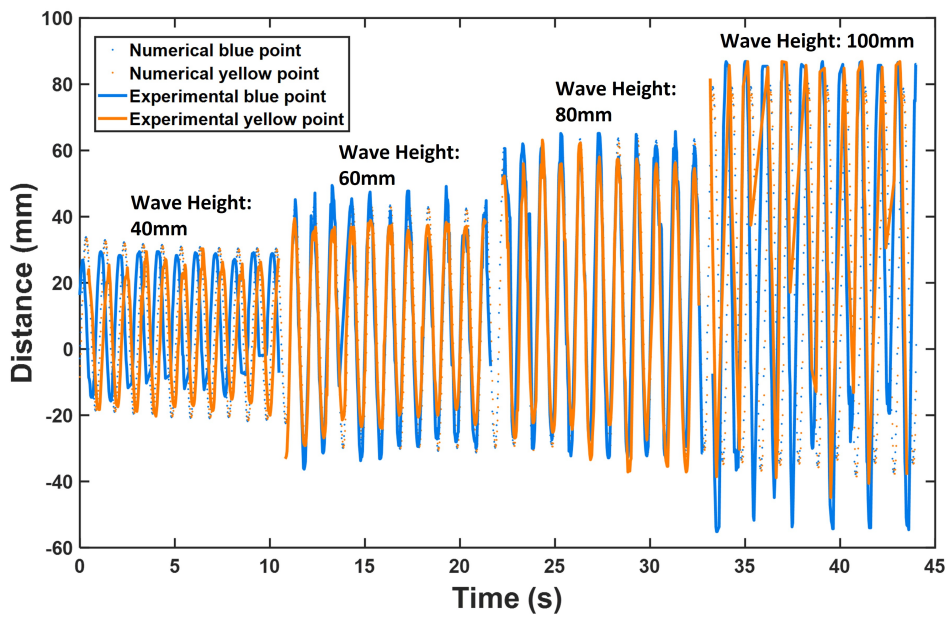


FIGURE 4.17: Comparison between the experimental and numerical moving distance of HSO-TENG.

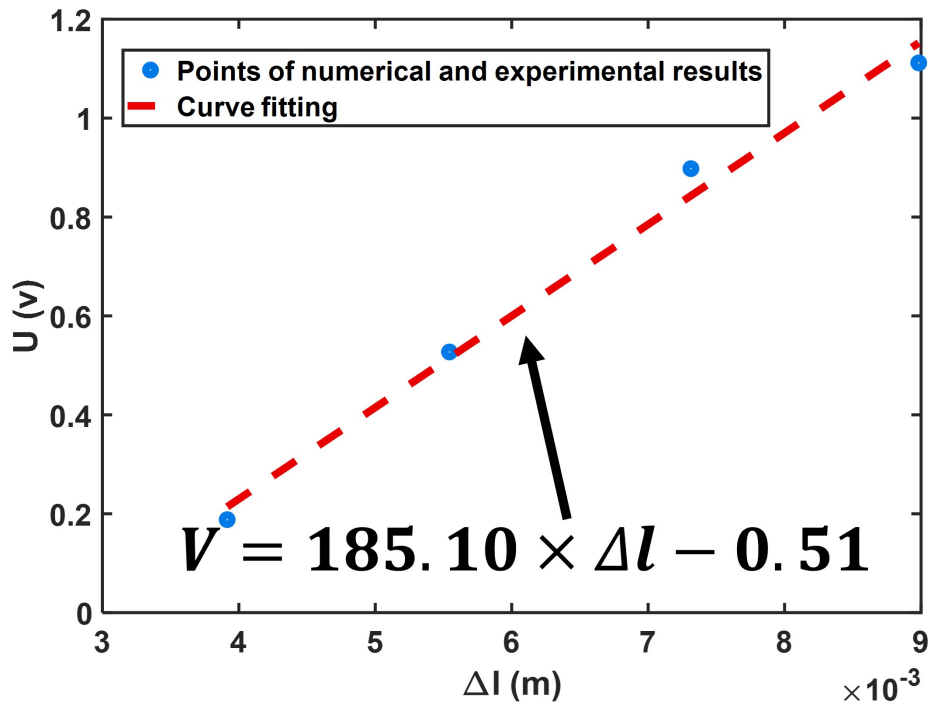


FIGURE 4.18: The relationship between numerical average changes in length and experimental average voltage (U: experimental average voltage (v), Δl : numerical average changes in Length (m)).

Fig. 4.17 displays a comparison between the experimental and numerical distances in the streamwise direction from their respective reference lines. Remarkably, both the blue and yellow points exhibit strong agreement between the experimental and numerical results, indicating the reliability of our numerical model.

Subsequently, we establish a predictive relationship between the average changes in length of the SO-TENG and the resultant average voltage, as depicted in Fig. 4.18. This relationship exhibits linearity, derived through curve fitting, allowing us to anticipate the voltage generated by the different parts of the SO-TENG based on their respective lengths.

4.2.5 Experimental results and discussion

This section introduces the response of the HSO-TENG to wave parameters and its capability in supplying power to sensors. To comprehensively compare the output voltage and motion of the HSO-TENG equipped with a double swing structure in the wave tank (Fig. 4.19), we contrast the inherent distinctions between liquid-solid coupling and swing machine simulations. The analysis reveals the HSO-TENG's response from the wave trough to the crest, wherein it deflects downstream, causing part C compression and part D stretching. This motion results in a prominent negative peak in the voltage curve (stage 1). Subsequently, the HSO-TENG rotates towards a horizontal position as it moves past the wave crest, inducing a minor wave peak (stage 2). It then deflects upstream, generating a small negative peak in part D's voltage curve (stage 3). As it returns to a horizontal position after passing through the trough, part D compresses (stage 4). The larger peaks during stages 1 and 4, influenced by the force accumulation at the wave crest, differentiate the wave's direction through the HSO-TENG's output curve. Notably, parts A and B

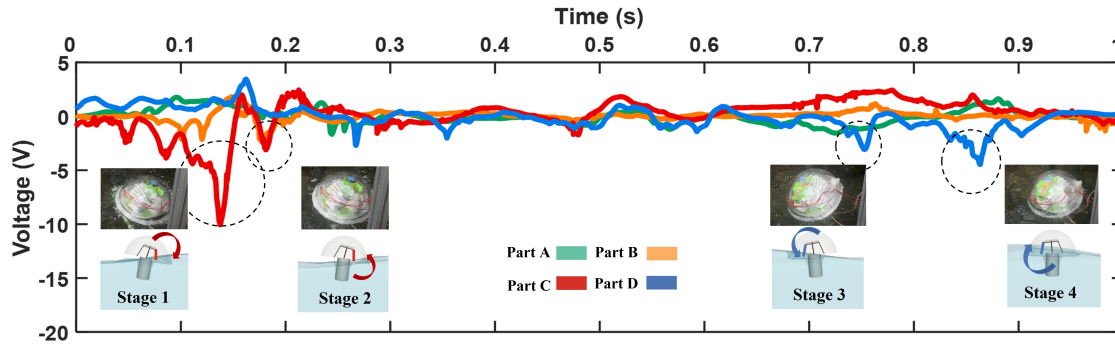


FIGURE 4.19: Four stages of output voltage and motion of HSO-TENG in one experimental wave period.

generate output voltage in the spanwise direction, facilitating stable power supply regardless of the wave direction faced by the HSO-TENG.

In Fig. 4.20 and 4.21, linear relationships between the voltage domain frequency and wave frequencies, as well as wave periods, indicate a fundamental basis for predicting wave characteristics. Fig. 4.22-4.23 exhibit the linear relationship between average absolute voltage, average maximum voltage, and different wave heights, demonstrating the potential to estimate wave heights using these voltage parameters.

Lastly, in Fig. 4.24, a sensor test shows the HSO-TENG's ability to power other sensors. The four HSO-TENG parts, interconnected in parallel, supply power to a temperature and humidity sensor through a rectifier circuit and a $47\mu F$ capacitor. At a wave height of 100mm and a wave period of 1s, the sensor operates continuously at 0.15mW, affirming the HSO-TENG's potential as a reliable power source for various sensors.

4.3 Numerical simulation in mul-direction circular wave tank

4.3.1 Introduction of numerical mul-direction circular wave tank

This section explores the operational characteristics of the devices when they are subjected to multi-directional waves through simulations within a circular numerical wave tank. The numerical circular wave tank is developed using the open-source program DualSPHysics (Domínguez et al., 2022). In Fig. 4.25, the HSO-TENG's numerical model is positioned at the center of the circular wave tank, equipped with 168 wave makers to generate multi-directional waves.

The reliability of this numerical circular wave tank has been rigorously validated at the FloWave tank at the University of Edinburgh, with comprehensive details available in (Kanehira et al., 2020). The parameters used in this study for the numerical wave tank and HSO-TENG are outlined in Table 4.3. By using this numerical wave tank, the HSO-TENG is tested in waves with four spreading parameters ($s=5, 10, 25,$ and $\text{infinity}(\text{inf})$) and four mean wave direction angles ($\text{Angle}=0^\circ, 15^\circ, 30^\circ,$ and 45°) in section 4.3.2.

4.3.2 Numerical results in sensing wave directions and parameters

In this section, we compare the voltage generated by the SO-TENG under different spreading parameters. Initially, we consider four distinct spreading parameters: $s=5,$

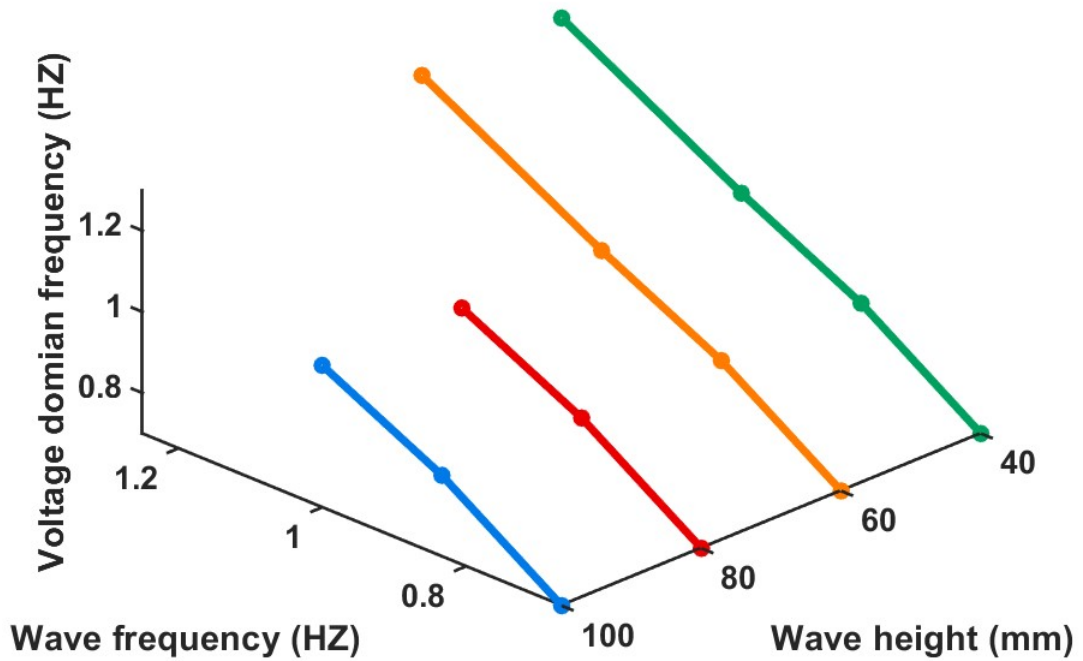


FIGURE 4.20: The relationships between the voltage domain frequency and wave frequencies.

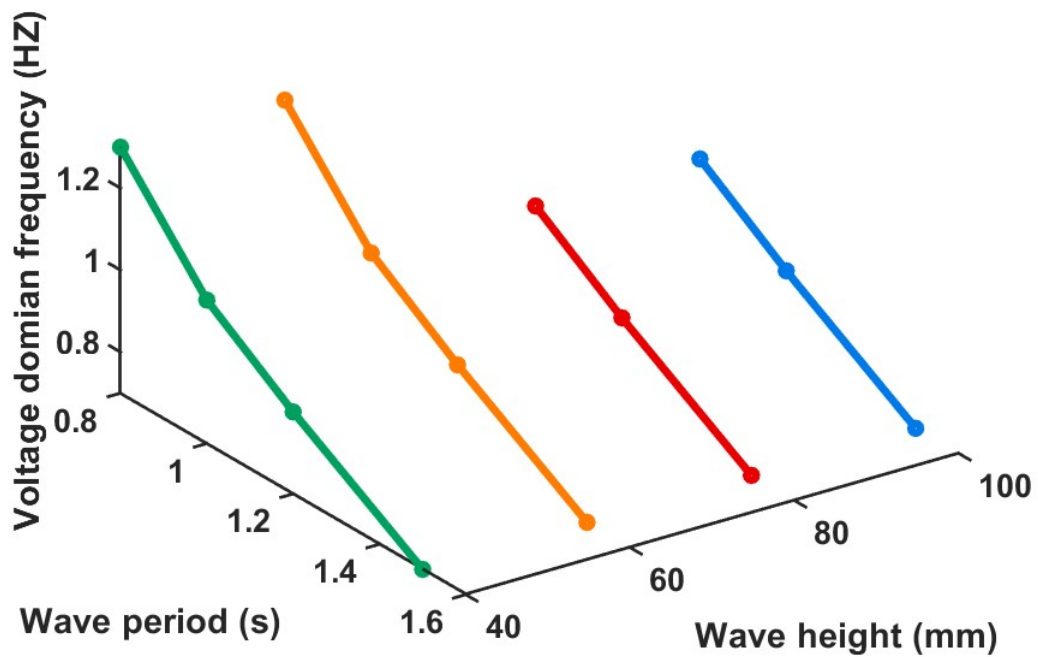


FIGURE 4.21: The relationships between the voltage domain frequency and wave periods.

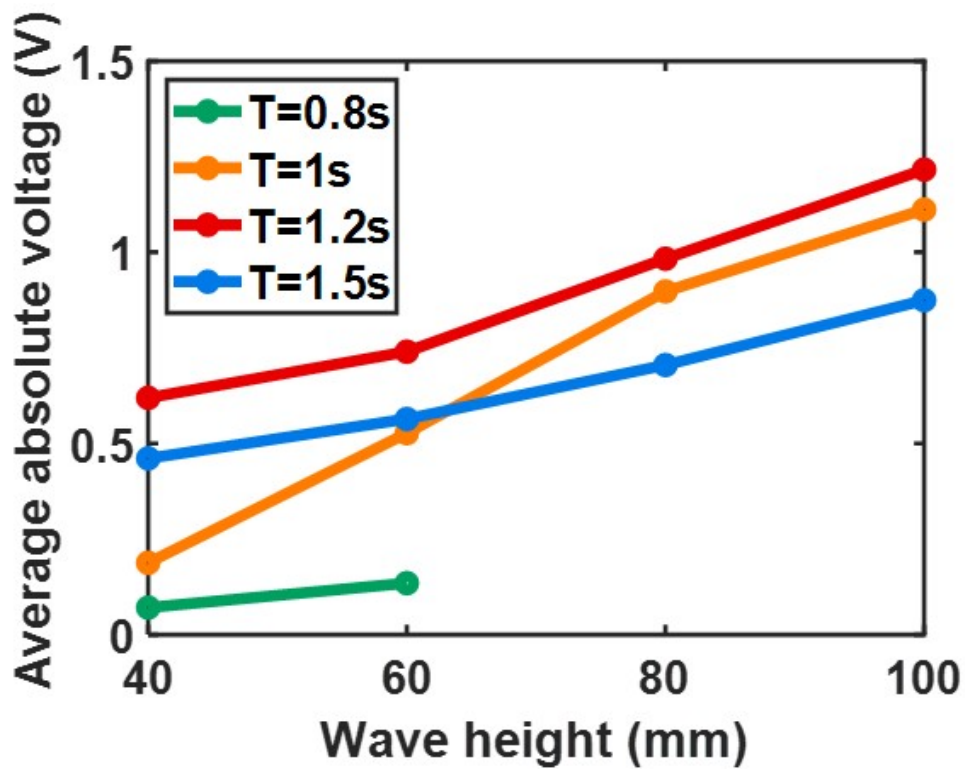


FIGURE 4.22: The average absolute voltage under different wave heights.

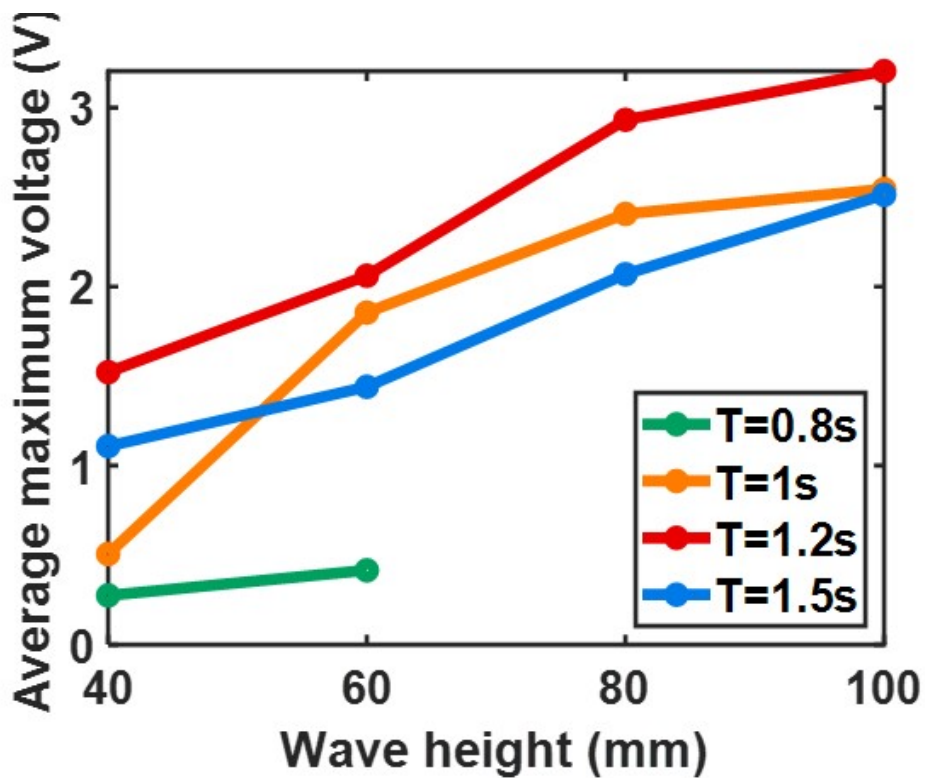


FIGURE 4.23: The average maximum voltage under different wave heights.

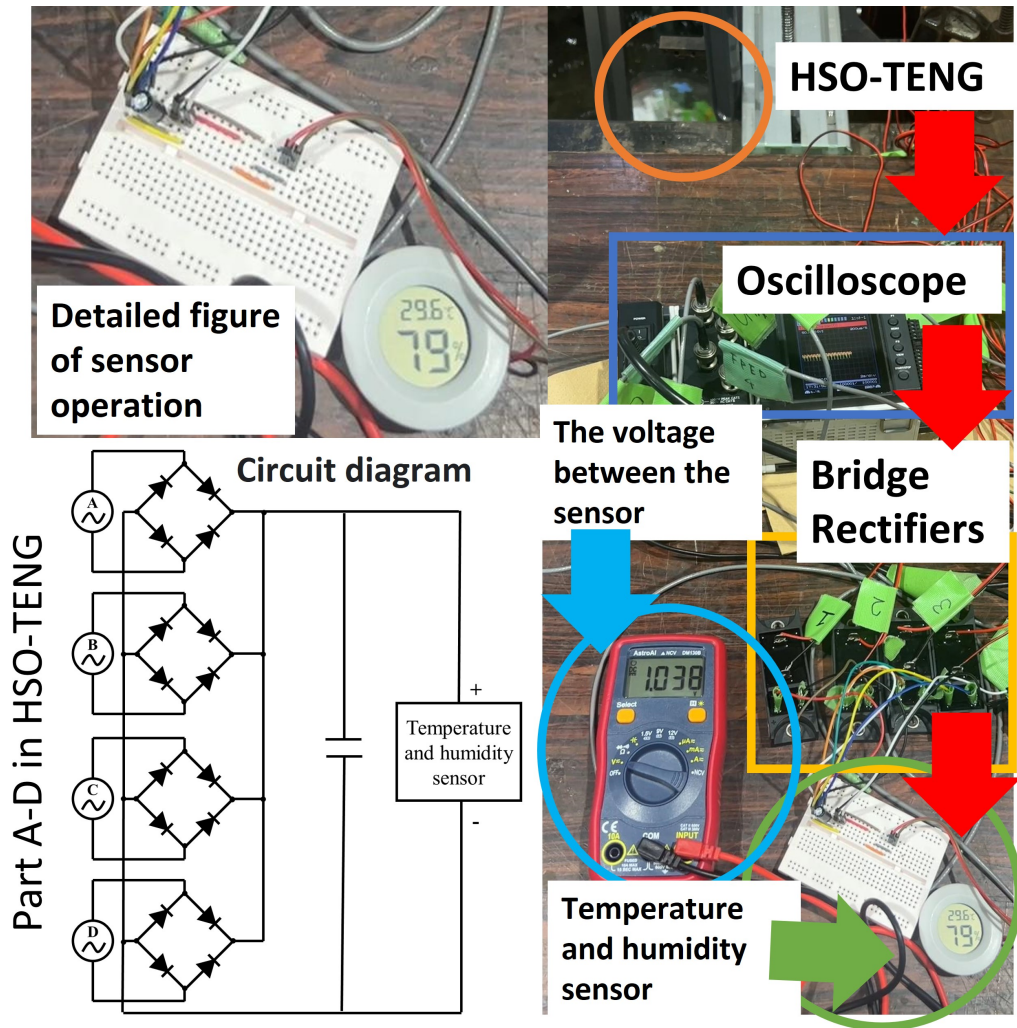


FIGURE 4.24: The test of supplying the temperature and humidity sensor continuously (The power of the sensor is 0.15mW).

TABLE 4.3: Setting parameters of the numerical mul-direction circular wave tank

| | | |
|------------------|------------------------------------|------------------------------|
| Scale parameters | Distance of particles | 0.07m |
| | Number of particles | 3278609 |
| | Time of simulation | 40s |
| | Time step | 0.1s |
| | Diameter of the circular wave tank | 25m |
| | Tank depth | 2m |
| | Diameter of the HSO-TENG | 1.11m |
| Wave parameters | Number of wave makers | 168 |
| | Wave period | 1.5s |
| | Wave height | 0.05m |
| | Spreading parameters (s) | 5, 10, 25 and infinite (inf) |
| | Wave direction angles | 0°, 15°, 30° and 45° |

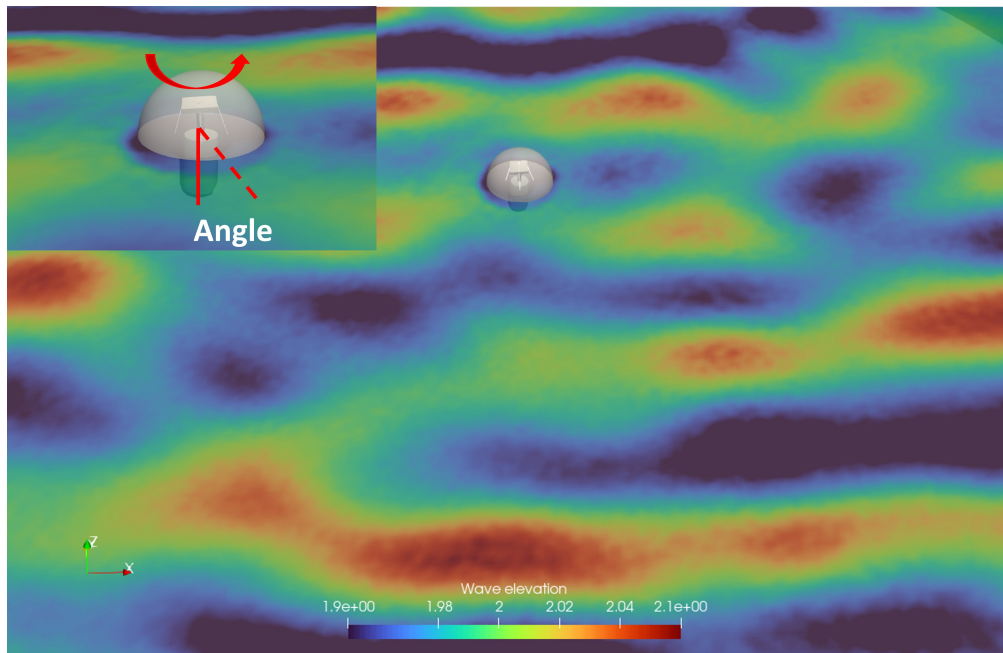


FIGURE 4.25: Overview of Numerical circular wave tank and the HSO-TENG.

10, 25, and ∞ , with the mean wave direction angle set at 0° . As illustrated in Fig. 4.26(i), the short-crested wave fields gradually diminish as s increases, ultimately resulting in solely long-crested waves when s approaches infinity. The HSO-TENG is positioned at the center of the wave tank, and the four SO-TENG parts are represented by spring modules, from which voltage is calculated based on the change in SO-TENG length (Δl) and the equation shown in Fig. 4.26(ii). Notably, when $s=5$, parts A and B exhibit high amplitude voltage fluctuations that decrease progressively as s decreases, nearly dissipating when s reaches infinity. Conversely, parts C and D, aligned with the mean wave direction, display more pronounced voltage fluctuations compared to parts A and B, which are oriented perpendicular to the mean wave direction.

Subsequently, the impact of varying mean wave direction angles (angle= 0° , 15° , 30° , and 45°) is explored, considering the HSO-TENG's symmetry with a fixed spreading parameter of 5. Fig. 4.26(ii) illustrates this analysis, where green, yellow, red, and blue represent the four SO-TENG parts. The voltage among these parts exhibits noticeable differences with varying angles. Particularly, as the angle increases up to 45° , voltage across all parts equalizes.

Consequently, the predicted average voltage of the four SO-TENG parts with different s and angle settings is showed in Fig. 4.27(i) and 4.27(ii) respectively. These results highlights the potential of using the HSO-TENG to monitor subtle changes in wave direction and ocean wave spreading parameters via the output voltage of each SO-TENG part.

In addition, based on voltage calculations derived from experiments and prediction models, the average power of an HSO-TENG device ranges from $0.06 \text{ w/m}^2/h$ to $1.07 \text{ w/m}^2/h$, and the maximum power ranges from $0.12 \text{ w/m}^2/h$ to $8.1 \text{ w/m}^2/h$. It can be inferred that one or more devices can charge the capacitor and supply small sensors or equipment, including lighting, temperature and humidity sensors, oxygen sensors, wind speed sensors, etc., to monitor the marine environment.

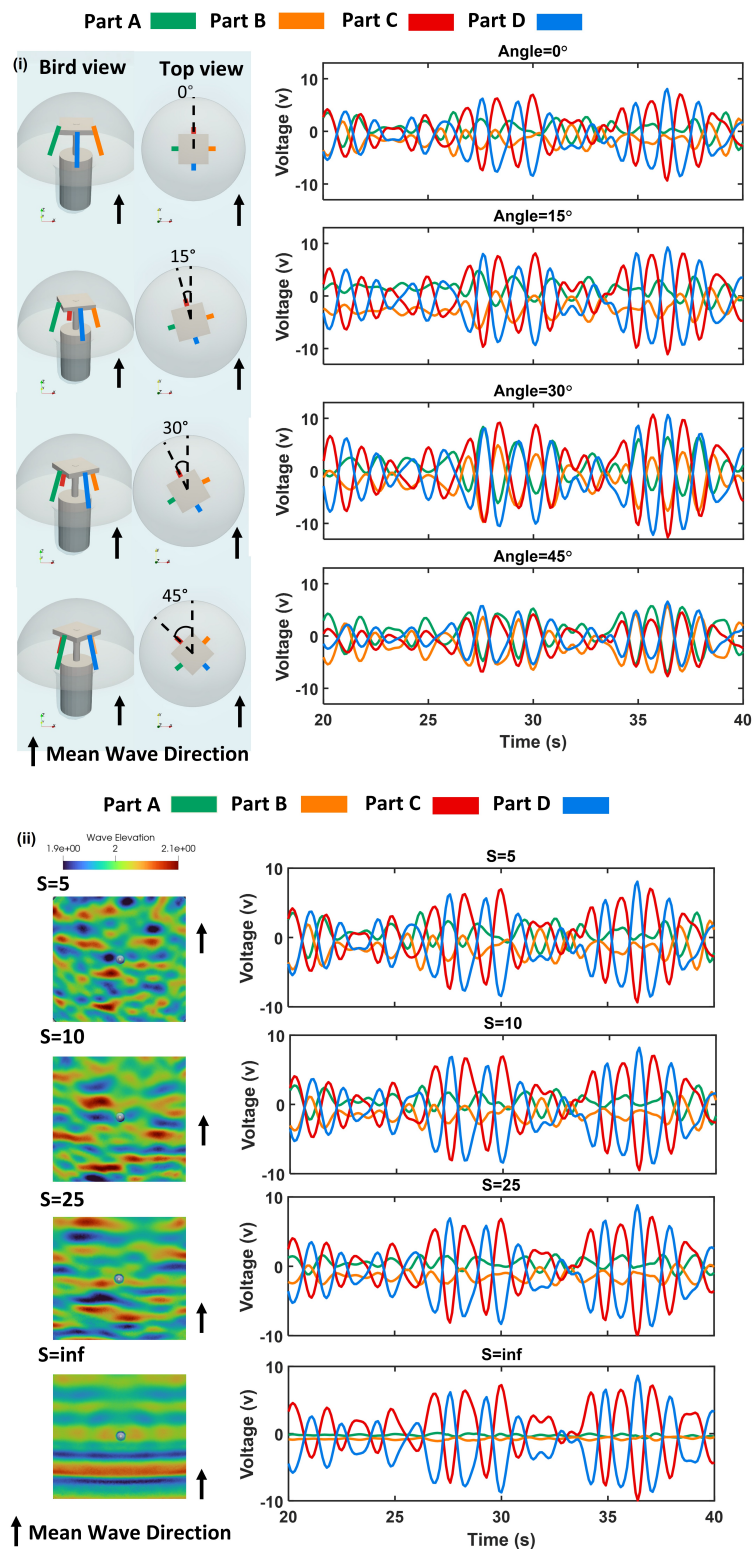


FIGURE 4.26: The voltage of HSO-TENG in circular wave tank. (i) Numerical simulation of HSO-TENG in circular wave tank and the voltage with four spreading parameters: $s=5, 10, 25$ and ∞ (mean wave direction angle $=0^\circ$). (ii) Numerical simulation of HSO-TENG in circular wave tank and the voltage with four mean wave direction angles: Angle $=0^\circ, 15^\circ, 30^\circ$ and 45° (spreading parameter $=5$).

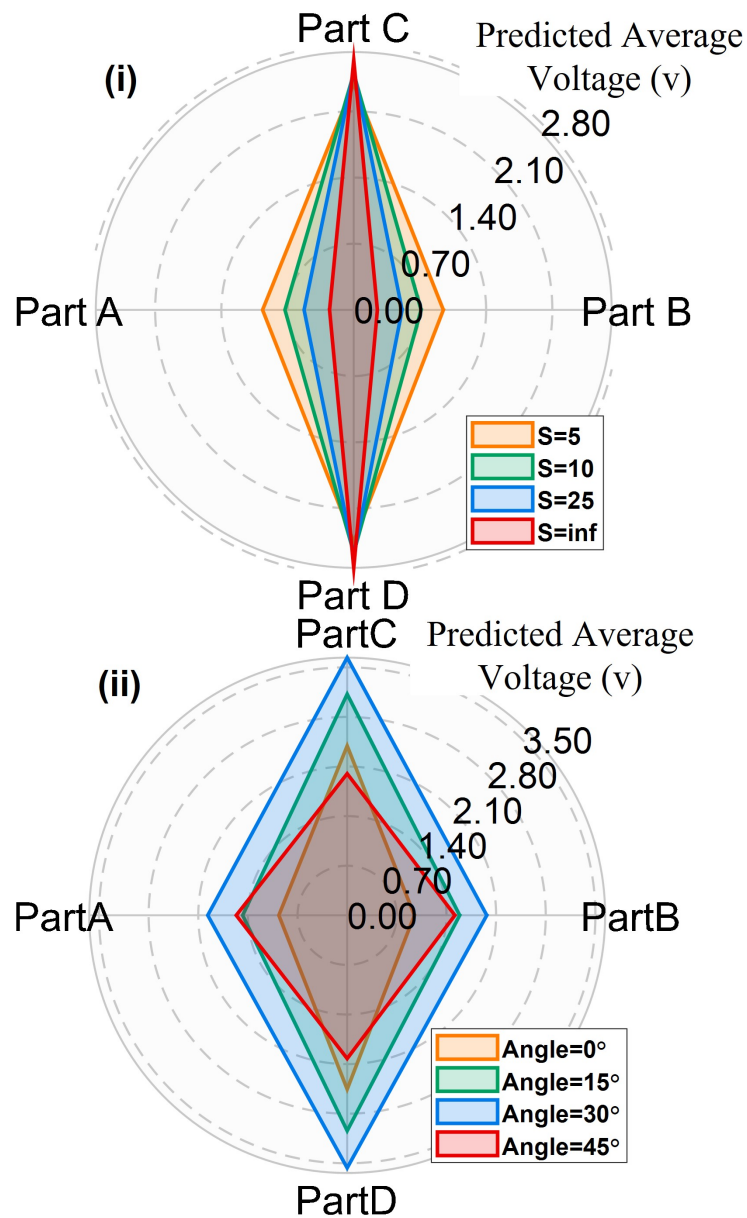


FIGURE 4.27: The predicted average voltage of the four SO-TENG parts. (i)The predicted average voltage of the four SO-TENG parts under different spreading parameters. (ii)The predicted average voltage of the four SO-TENG parts under different mean wave direction angles.

To further validate this numerical model, future work will involve tests of the HSO-TENG in real sea areas.

4.4 Conclusions

In summary, the HSO-TENG, proposed in this research, demonstrates robust power generation and effective wave monitoring capabilities following a series of optimizations, with key findings as outlined below:

- Optimization of three structural parameters (the weight of the magnet mass, the hammer's height, and the external swing arm's length) results in substantial enhancements in average voltage generation by 33%, 62%, and 50% respectively.
- Through numerical model comparison analysis, the 'no-submergence' condition is selected among three fixed conditions, allowing for complete compression and stretching of SO-TENGs.
- The optimized HSO-TENG exhibits impressive responses to various wave characteristics including wave height, period, frequency, direction, and spreading parameters, as evidenced by output voltage data obtained from large-scale wave tank experiments and numerical circular wave tank simulations.
- The maximum voltage output reaches 15V, and when the four SO-TENGs are connected in parallel, they sustainably power a temperature and humidity sensor.
- Using the SPH method proves effective in simulating HSO-TENG and similar energy harvesting devices in waves, offering valuable insights into device design and performance prediction.

Therefore, the HSO-TENG demonstrates efficient sensor capabilities, accurately responding to wave parameters, and simultaneously serves as an energy supply for other sensors. At the same time, the optimized methods can be applied for coupling similar self-powered ocean monitoring device with ocean wave.

Conclusively, the sensor capabilities of HSO-TENG are shown, accurately interpreting wave parameters while the ability of serving as an energy source for additional sensors are proved. Moreover, the optimized methodologies can be used for integrating such kind of self-powered ocean monitoring devices with ocean wave interaction.

Chapter 5

Numerical study on drag reduction and turbulence energy based on polymer coating

In this chapter, we focus on numerical simulation *DR* research using polymer coating. Considering the limitations of the experimental conditions and cost and time-effective, numerical simulation is a good method to explore the drag reduction mechanism of this type of viscoelastic fluid.

5.1 Numerical method based on DNS/LES-DPD

The numerical model used in this study includes two distinct components: the DNS/LES component and the DPD one. The DNS/LES part is specifically designed for modeling Newtonian fluids, while the DPD component represents polymer systems. To handle low Reynolds numbers, the DNS method is adeptly applied, whereas for cases involving high Reynolds numbers, the LES method is utilized. If precise simulation outcomes are required, the DNS method stands as the preferred choice, while for enhanced computational efficiency, the LES method offers a viable alternative.

5.1.1 Governing equations

DNS method

The governing equations for incompressible flows, the Navier-Stokes equations, are depicted in Eqs. [5.1] and [5.2]. Here, \mathbf{u} is the flow velocity, t represents time, ∇ denotes the divergence operator, ρ is fluid density, p denotes pressure, ν represents kinematic viscosity, Δ stands for the Laplacian operator, and \mathbf{f} is an external body force. Typically, the convective term is expressed as $\nabla \cdot (\mathbf{u}\mathbf{u})$, the pressure gradient as $-\frac{1}{\rho}\nabla p$, and the viscous term as $\nu\Delta\mathbf{u}$. Eq. [5.2] explains the continuity of the incompressible fluid, while Eq. [5.3] explains Poisson's equation for pressure derivation.

$$\frac{\partial \mathbf{u}}{\partial t} + \nabla \cdot (\mathbf{u}\mathbf{u}) = -\frac{1}{\rho}\nabla P + \nu\Delta\mathbf{u} + \mathbf{f} \quad (5.1)$$

$$\nabla \cdot \mathbf{u} = 0 \quad (5.2)$$

$$\Delta P = -\Delta \cdot (\mathbf{u}\mathbf{u}) \quad (5.3)$$

LES method

The governing equations for filtered turbulent flow used in the LES method are depicted in Eq. [5.4]

$$\frac{\partial \bar{\mathbf{u}}}{\partial t} + \nabla \cdot (\bar{\mathbf{u}} \bar{\mathbf{u}}) = -\frac{1}{\rho} \nabla \bar{P} + \nu \Delta \bar{\mathbf{u}} + \nabla \cdot \tau^{SGS} + \mathbf{f} \quad (5.4)$$

Here, SGS represents sub-grid-scale. τ^{SGS} represents the sub-grid-scale stress tensor, indicating the impact of sub-grid-scale flow phenomena on the overall grid-scale flow.

$$\tau^{SGS} = \bar{\mathbf{u}} \bar{\mathbf{u}} - \overline{\mathbf{u} \mathbf{u}} \quad (5.5)$$

In this research, the Smagorinsky model, initially proposed in 1963 by Smagorinsky (Smagorinsky, 1963), is selected and remains a prevalent choice in current studies. Similar to many contemporary subgrid models, the Smagorinsky model retains the eddy-viscous concept assumption. The τ^{SGS} component, representing the subgrid-scale part of the strain rate tensor $\bar{\mathbf{S}}$ associated with the solved velocity field, can be expressed as follows:

$$\tau^{SGS} - \frac{1}{3} \text{tr}(\tau^{SGS}) \mathbf{I} = -2\nu_{SGS} \bar{\mathbf{S}} \quad (5.6)$$

$$\bar{\mathbf{S}} = \frac{1}{2} (\nabla \bar{\mathbf{u}} + \nabla \bar{\mathbf{u}}^T) \quad (5.7)$$

Here, \mathbf{I} denotes the identity matrix.

DPD method

The main DPD equation, Eq[5.8], focuses on the interaction between nearby particles. Here, m signifies the mass of each DPD particle. The subscript i denotes the specific DPD particle, while ij represents the impact of the i th DPD particle on the j th DPD particle. The velocity of individual DPD particles is denoted as v_i . F_{ij}^C stands for the conservative force, acting as a soft repulsive force between particles. The dissipative force, F_{ij}^D , and the random force, F_{ij}^R , adhere to the fluctuation-dissipation theorem, their statistical values contingent upon the system's temperature.

$$m \frac{d\mathbf{v}_i}{dt} = \sum_{j \neq i} \mathbf{F}_{ij}^C + \sum_{j \neq i} \mathbf{F}_{ij}^D + \sum_{j \neq i} \mathbf{F}_{ij}^R \quad (5.8)$$

\mathbf{F}_{ij}^C is introduced in the following equation:

$$\mathbf{F}_{ij}^C = \alpha w_R(r_{ij}) \mathbf{e}_{ij} \quad (5.9)$$

where α represents the coefficient of repulsion between particles, r represents the position of the DPD particles, r_{ij} represents the distance between particle i and j , and \mathbf{e}_{ij} represents a unit vector that represents the direction from particle j to particle i . The term $w_R(r_{ij})$ represents the weight function of the random force, which depends on the distance:

$$w_R(r_{ij}) = \begin{cases} 1 - \frac{r_{ij}}{r_c} & \text{for } r_{ij} \leq r_c \\ 0 & \text{for } r_{ij} > r_c \end{cases} \quad (5.10)$$

Here, the variable r_c limits the scope of particle interaction. The dissipative force, accounting for viscosity effects, relies on both the relative positions and velocities of the particles. It's defined as:

$$\mathbf{F}_{ij}^D = -\gamma w_D(r_{ij}) (\mathbf{e}_{ij} \cdot \mathbf{v}_{ij}) \mathbf{e}_{ij} \quad (5.11)$$

In Eq[5.11], γ stands as a coefficient ($= \frac{\alpha}{10}$), while $w_D(r_{ij})$ denotes the distance-dependent weight function of the dissipative force. The random force, \mathbf{F}_{ij}^R , reflects thermal fluctuations' effects and is solely dependent on the relative positions of the particles. It's commonly expressed in the form:

$$\mathbf{F}_{ij}^R = \sigma w_R(r_{ij}) \mathbf{e}_{ij} \zeta_{ij} \quad (5.12)$$

Here, σ represents a coefficient controlling the dissipative force. ζ_{ij} represents a random fluctuation variation factor following a Gaussian distribution linked to the integral time element. Lastly, the position at the $(n+1)^{th}$ time step can be determined using the velocity from the n^{th} time step, \mathbf{v}^n , as shown in Eq[5.13].

$$\mathbf{r}^{n+1} = \mathbf{v}^n \times \Delta t \quad (5.13)$$

The mathematical model used in this study is outlined in Satoh et al.'s work(Satoh, 2014).

5.1.2 Coupling method

Re-transformation between two parts

As the equations proposed in (Satoh, 2014) show, the local shear stress τ_d is the sum of particle momentum and the forces of particle interaction, which encompass the dissipative force viscosity (v_{FD}) and conservative force (v_{FC}). Therefore, the local shear stress can be described as follows:

$$\tau_d = v_{mm} + v_{FD} + v_{FC} \quad (5.14)$$

$$v_{mm} = \mathbf{v}_y \times (\mathbf{v}_x + r_y \cdot \dot{\gamma}_{DPD}) \quad (5.15)$$

Here, v_{mm} is calculated using Eq[5.15]. \mathbf{v}_y represents the velocity of DPD particles in the wall-normal direction, while \mathbf{v}_x indicates the velocity in the streamwise direction.

By utilizing Eq[5.16] and Eq[5.17], the Reynolds number, Re_{DPD} , for each DPD particle can be determined, wherein δ equates to half the hydraulic diameter.

$$u_d = \sqrt{\frac{\tau_d}{\rho}} \quad (5.16)$$

$$Re_{DPD} = \frac{u_d \delta}{\nu} \quad (5.17)$$

In Fig.(5.1), a schematic representation illustrates the relationship between the Reynolds number in the DNS/LES (Re_{NF}) and the DPD simulation. In this depiction, x corresponds to the streamwise direction, while y represents the wall-normal direction. DPD particles are visible only in the light blue area, demarcated by H_{DPD} , signifying the height of the DPD particle region. Notably, Y_{NF} indicates the y position within the DNS/LES grid. The superscripts of Re_{NF} and Y_{NF} , represented as

j , denote the sequence number of the grid in the y direction. Meanwhile, k signifies the label of the k^{th} DPD particle. Additionally, $C0$ stands for the length of one DPD cell, while L^k denotes the distance between the position of the calculated y grid, Y^j_{NF} , and the k^{th} DPD point, r_y^k . The values of the DNS/LES Reynolds number are calculated using the expressions in Eq[5.18-5.19].

$$Re^j_{NF} = (1 - \Phi) \times coeff_{Re} \times \sum_{L^k < C0} Re^k_{DPD} \times \frac{L^k}{C0} + \Phi \times Re_{ini} \quad (5.18)$$

$$L^k = |r_y^k - Y^j_{NF}| \quad (5.19)$$

The discriminant value, Φ , distinguishes the DNS/LES-DPD method: $\Phi = 0$ denotes the light blue area when r_y^k is smaller than H_{DPD} , representing the association between DNS/LES and DPD methods. Conversely, when r_y^k exceeds H_{DPD} , $\Phi = 1$, representing the exclusive use of the DNS/LES method in the dark blue area. The coefficient of Reynolds number conversion, $coeff_{Re}$, relates to the initial Reynolds number, Re_{ini} . When $\Phi = 0$, Eq[5.18] transforms the Reynolds number from the DPD part to the DNS/LES part. Here, all Re_{DPD} values of the DPD points, for which L^k is less than $C0$, are collated to calculate Re_{NF} for the j^{th} grid in the y direction. This corresponds to the area delineated by the yellow dashed line in Fig.(5.1).

$Re_{NF}^1 - Re_{NF}^{N_y}$ denote the Reynolds numbers in the y direction, aligned with the y grids, with N_y representing the label of the maximum y position within the light blue area. The Reynolds number over the DPD region equates to the initial Reynolds number, Re_{ini} . Finally, to calculate the kinematic viscosity using Re_{NF} , the equation is utilized:

$$v = \frac{Re_{ini} \times v_{ini}}{Re_{NF}} \quad (5.20)$$

Here, v_{ini} represents the initial kinematic viscosity.

Shear velocity transformation between two parts

The DPD shear velocity is determined based on values obtained from the DNS/LES component. Initially, the DNS/LES shear velocity, denoted as $\dot{\gamma}_{NF}$, is calculated using Eq[5.21].

$$\dot{\gamma}_{NF} = \frac{\partial u}{\partial y} \quad (5.21)$$

$$\dot{\gamma}_{DPD} = \frac{coeff_{\dot{\gamma}}}{(Y_{NF}^{j+1} - Y_{NF}^j)} \times \begin{bmatrix} Y_{NF}^{j+1} - r_y & r_y - Y_{NF}^j \end{bmatrix} \cdot \begin{bmatrix} \dot{\gamma}_{NF}^j \\ \dot{\gamma}_{NF}^{j+1} \end{bmatrix} \left(Y_{NF}^j \leq r_y \leq Y_{NF}^{j+1}, j + 1 \leq N_y \right) \quad (5.22)$$

The conversion from DPD shear velocity to DNS/LES shear velocity is established by Eq[5.22]. Within this equation, $coeff_{\dot{\gamma}}$ represents the coefficient for shear velocity conversion. Additionally, Y_{NF}^j denotes the y position of the DNS grid, corresponding to $\dot{\gamma}_{NF}^j$. On the other hand, r_y signifies the y position of the DPD particle. In Fig. 5.2, the red lines illustrate the DNS/LES grid, while the green dots symbolize the DPD particles. A specific point is highlighted by the yellow circle, serving as a sample point to compute the DPD shear velocity. The calculation involves determining the shear velocity of this DPD particle by utilizing the Newtonian shear velocities, $\dot{\gamma}_{NF}^{j+1}$ and $\dot{\gamma}_{NF}^j$, as specified by Eq[5.22].

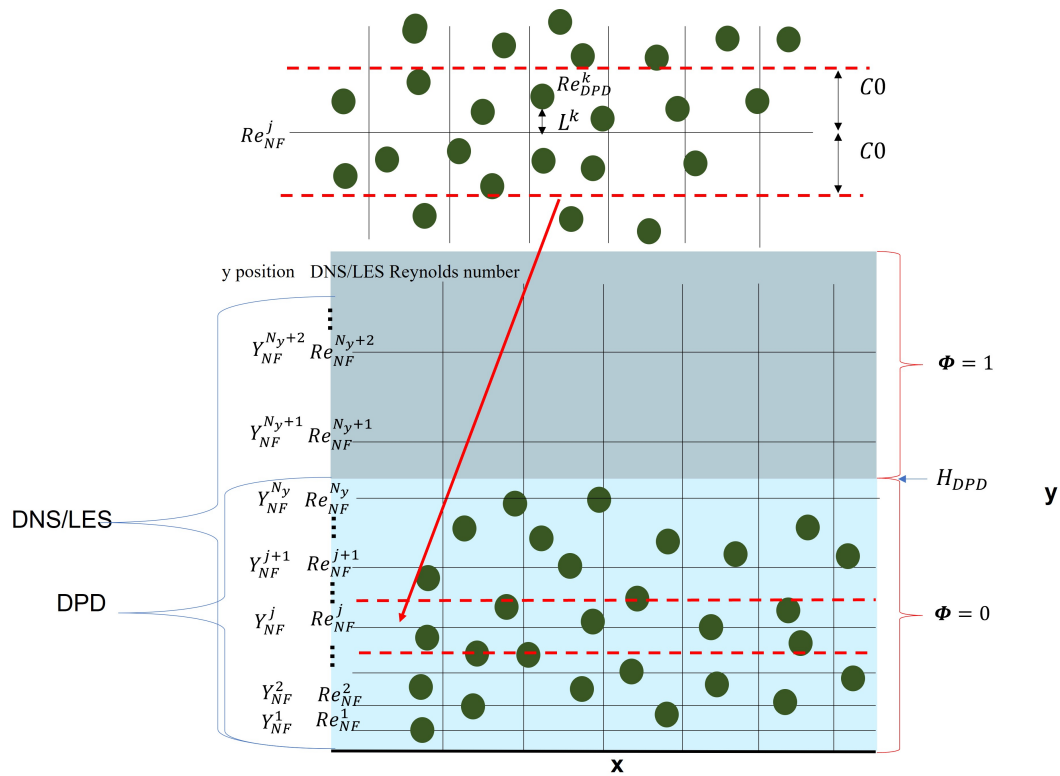


FIGURE 5.1: Schematic of the transformation from the DPD Reynolds number to the DNS/LES value

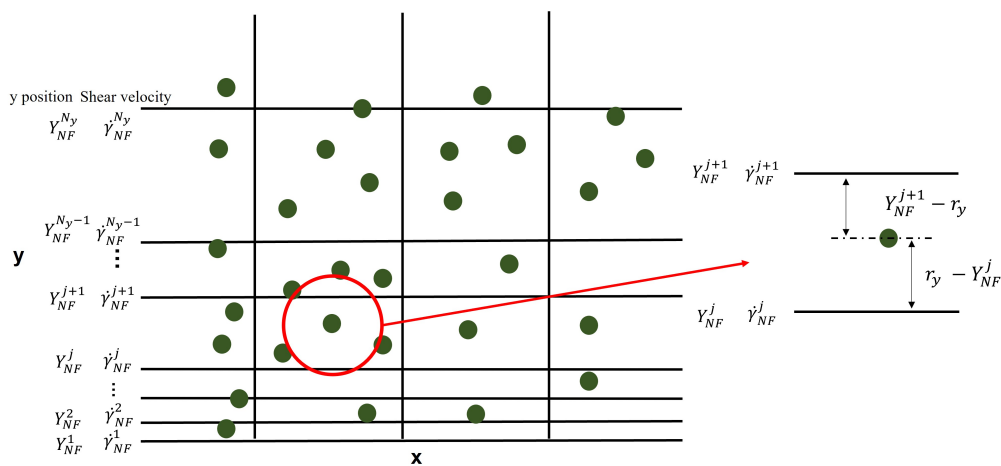


FIGURE 5.2: Schematic of the transformation from the DNS/LES shear velocity to the DPD one

5.1.3 Numerical algorithm

The time discretization of the DNS/LES component is the fourth-order Runge-Kutta 4 (RK4) method, characterized by classical coefficients in each substep: $b(1) = \frac{1}{6}$, $b(2) = \frac{1}{3}$, $b(3) = \frac{1}{3}$, and $b(4) = \frac{1}{6}$.

Within each substep, the Helmholtz theorem is applied to couple pressure and velocity. This approach allows for the separate calculation of the divergence-free and curl-free components using the intermediate velocity $\mathbf{u}^{n+\frac{1}{2}}$:

$$\mathbf{u}\mathbf{k} = (\nu\Delta\mathbf{u})^n - (\nabla \cdot (\mathbf{u}\mathbf{u}))^n + \mathbf{f} \quad (5.23)$$

The difference between the viscous term, $(\nu\Delta\mathbf{u})^n$, and the convective term, $(\nabla \cdot (\mathbf{u}\mathbf{u}))^n$, at the substep is defined as $\mathbf{u}\mathbf{k}$. Subsequently, the intermediate velocity $\mathbf{u}^{n+\frac{1}{2}}$ is computed using the velocity \mathbf{u}^n from the last time step and $\mathbf{u}\mathbf{k}$ with Eq[5.24].

$$\mathbf{u}^{n+\frac{1}{2}} = \mathbf{u}^n + \Delta t(\mathbf{b} \cdot \mathbf{u}\mathbf{k}) \quad (5.24)$$

Subsequently, the velocity \mathbf{u}^{n+1} at this particular time step is computed using $\mathbf{u}^{n+\frac{1}{2}}$, and the pressure gradient is then applied accordingly:

$$\mathbf{u}^{n+1} = \mathbf{u}^{n+\frac{1}{2}} + \mathbf{P} \quad (5.25)$$

At the fourth iteration of the RK4 method, the \mathbf{u}^{n+1} becomes the final velocity for that particular time step.

Numerical models are constructed in MATLAB based on the approach outlined above. The DNS program used in our CFD model is adapted from the approach detailed in reference (Vuorinen and Keskinen, 2016), chosen for its computational speed and memory efficiency. Figure 5.3 illustrates the schematic of the DNS/LES-DPD model applied in this study. The process initiates from Steps 1 and 2, where the velocity-pressure coupling is determined using Eq[5.1]-Eq[5.3]. During these steps, the DNS/LES velocity (u^n) and pressure (P^n) at the current-time step are derived from the values of the last-time step (u^{n-1} and P^{n-1}) and the DNS/LES kinematic viscosity (ν^{n-1}). Proceeding to Step 3, the DNS/LES shear velocity ($dot\gamma_{NF}^n$) at the current-time step is computed based on u^n , corresponding to Eq[5.21]. Step 4 involves updating the position of fluid grids (r^n) at the current-time step using Eq[5.13], in conjunction with the velocity of DPD particles at the last-time step (v^{n-1}). Subsequently, in Step 5, the velocity of DPD particles (v^n) is updated using the entire force from the last-time step (F^{n-1}) via Eq[5.8]. Step 6 computes the DPD shear velocity ($dot\gamma_{DPD}^n$) at the current-time step, utilizing Eq[5.22], based on r^n and $dot\gamma_{NF}^n$ obtained in Step 3. In Step 7, Eq[5.9]-[5.12] are employed to calculate the force of DPD particles at the current-time step (F^n), utilizing r^n , v^n , and $dot\gamma_{DPD}^n$. Step 8 calculates the DPD Reynolds number (Re_{DPD}^n) using v^n and $dot\gamma_{DPD}^n$ through Eq[5.14]-[5.17]. Then, in Step 9, the DNS/LES Reynolds number (Re_{NF}^n) is inferred from Re_{DPD}^n and r^n using Eq[5.18]. Finally, in Step 10, the DNS/LES kinematic viscosity (ν^n) at the current-time step is derived from Re_{NF}^n using Eq[5.20], ready for subsequent iterations.

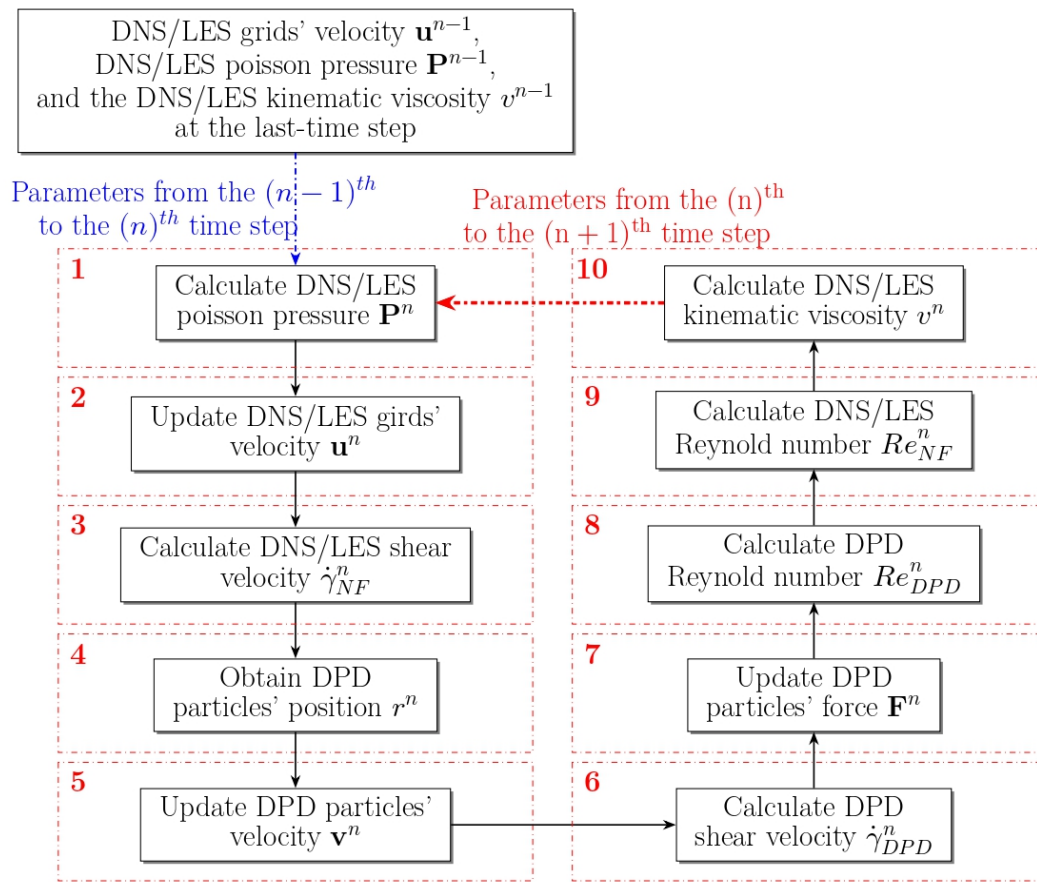


FIGURE 5.3: Schematic of the DNS/LES-DPD model

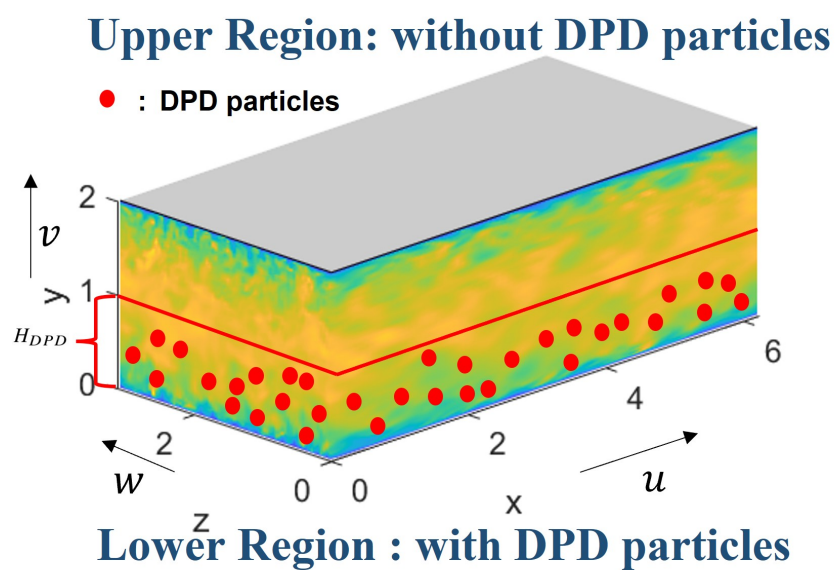


FIGURE 5.4: Schematic of the numerical domain

5.2 Results and discussion

5.2.1 Numerical domain and initial condition

Figure 5.4 depicts the numerical domain of the model, where the x -direction corresponds to the streamwise direction, the y -direction represents the wall-normal direction, and the z -direction signifies the spanwise direction, along with their respective velocities: u , v , and w . The red dots symbolize the polymer systems as represented by DPD particles. The height of the DPD particle region, denoted as H_{DPD} , aligns with that in Fig. 5.1. Essentially, the red line in Fig. 5.4 are the boundary between regions with and without DPD particles. The upper region signifies a Newtonian fluid simulated using the DNS or LES method, while the lower region indicates a polymer solution simulated via the DNS-DPD or LES-DPD method. It's important to note the consistency in the CFD methods employed in both the upper and lower regions. Tables 5.1 and 5.2 are a summary of operational parameters for nine distinct cases, segregating parameters for the lower and upper regions. Here, Re_b stands for the bulk Reynolds number, and Re_τ represents the friction Reynolds number, both calculated using Eq[5.26]-[5.27]:

$$Re_b = \frac{u_b(2\delta)}{\nu} \quad (5.26)$$

$$Re_\tau = \frac{u_\tau\delta}{\nu} \quad (5.27)$$

Here, u_b denotes the mean bulk velocity and u_τ is the friction velocity.

Den represents a particle density parameter calculated by Eq[5.28]:

$$Den = \gamma \times \frac{N_{DPD}}{V_{DPD}} \quad (5.28)$$

The parameter γ is calculated from Eq[5.11]. N_{DPD} signifies the total count of DPD particles, while V_{DPD} denotes the volume within which these particles are free to move. The computation of drag reduction rate ($DR(\%)$) is determined using Eq[5.29]:

$$DR\% = \frac{C_f - C_{f,N}}{C_{f,N}} \times 100\% \quad (5.29)$$

To ascertain the suitability of the LES-DPD method as an effective alternative to the DNS-DPD method, a comparison between Cases 2 and 7 is detailed in section 5.2.2b. In section 5.2.2c, the performances of Cases 1, 2, and 3, employing the LES-DPD method but with varying particle energy densities, are discussed and contrasted with the outcomes listed in Table 5.4. Section 4.3 examines and contrasts Cases 4, 5, 6, and 7 to determine the impact of H_{DPD} on the observed drag reduction (DR). Lastly, section 4.4 focuses on the comparison of Cases 2, 8, and 9, analyzing the model's performance under different Reynolds numbers while maintaining the same DR .

Before exploring the hybrid CFD and DPD model analysis, it's crucial to individually validate the results obtained from the DNS and LES algorithms by comparing them against previously published reference data. The roots of DNS simulations can be traced back to Orszag's work in 1971, which extensively explored channel flow problems. Typically, channel flow studies commence with low Reynolds numbers and incrementally increase them. Reynolds numbers lower than 300, especially 180, a commonly studied friction Reynolds number, have been extensively researched by

TABLE 5.1: Parameters of the nine cases in the lower region. Here H_{DPD} is the height of the DPD particles' region shown in Fig. 5.4, Re_b is the bulk Reynolds number based on the mean bulk velocity, Re_τ is the friction Reynolds number, Den is a particle density parameter calculated by Eq[5.28], and $DR(\%)$ is the rate of drag reduction calculated by Eq[5.29]

| Case | Method | H_{DPD} | Re_b | Re_τ | Den | $DR(\%)$ |
|------|---------|---------------------|--------|-----------|-------|----------|
| 1 | LES-DPD | δ | 3204 | 160 | 21.5 | 12.2 |
| 2 | LES-DPD | δ | 3204 | 154 | 43.0 | 21.1 |
| 3 | LES-DPD | δ | 3204 | 145 | 64.5 | 36.6 |
| 4 | DNS-DPD | $\frac{1}{3}\delta$ | 3204 | 169 | 387 | 1.2 |
| 5 | DNS-DPD | $\frac{1}{2}\delta$ | 3204 | 143 | 387 | 41.3 |
| 6 | DNS-DPD | δ | 3204 | 135 | 387 | 58.6 |
| 7 | DNS-DPD | δ | 3204 | 160 | 193.5 | 12.8 |
| 8 | LES-DPD | δ | 7505 | 335 | 193.5 | 22.0 |
| 9 | LES-DPD | δ | 12980 | 485 | 774.0 | 21.6 |

TABLE 5.2: Parameters of the nine cases in the upper region. Here H_{DPD} is the height of the DPD particle region shown in Fig. 5.4, Re_b is the bulk Reynolds number based on the mean bulk velocity, Re_τ is the friction Reynolds number, Den is a particle density parameter calculated by Eq[5.28], and $DR(\%)$ is the rate of drag reduction calculated by Eq[5.29]

| Case | Method | H_{DPD} | Re_b | Re_τ | Den | $DR(\%)$ |
|------|--------|-----------|--------|-----------|-------|----------|
| 1 | LES | 0 | 3204 | 170 | 0 | 0 |
| 2 | LES | 0 | 3204 | 170 | 0 | 0 |
| 3 | LES | 0 | 3204 | 170 | 0 | 0 |
| 4 | DNS | 0 | 3204 | 170 | 0 | 0 |
| 5 | DNS | 0 | 3204 | 170 | 0 | 0 |
| 6 | DNS | 0 | 3204 | 170 | 0 | 0 |
| 7 | DNS | 0 | 3204 | 170 | 0 | 0 |
| 8 | LES | 0 | 7505 | 370 | 0 | 0 |
| 9 | LES | 0 | 12980 | 535 | 0 | 0 |

various scholars like Kim (Kim, Moin, and Moser, 1987), Antonia (Antonia et al., 1992), Rutledge (Rutledge and Sleicher, 1993), Moser (Moser, Kim, and Mansour, 1999), Abe (Abe, Kawamura, and Matsuo, 2001), Alamo (Del Alamo et al., 2004), Tanahashi (Tanahashi et al., 2004), and Hu (Hu, Morfey, and Sandham, 2006), among others. Further investigations span Reynolds numbers from 300 to just below 1000, including values such as 300 (Spalart (Spalart, 1988)), 395 (Moser (Moser, Kim, and Mansour, 1999), Abe (Abe, Kawamura, and Matsuo, 2001)), 590 (Moser (Moser, Kim, and Mansour, 1999)), and 650 (Iwamoto (Iwamoto, Suzuki, and Kasagi, 2002)). As Reynolds numbers exceed 1000, studies tend to utilize progressively higher values: 1440 (Hu (Hu, Morfey, and Sandham, 2006)), 1901 (Juan (Del Alamo et al., 2004)), 2000 (Adrián (Lozano-Durán and Jiménez, 2014)), 2003 (Hoyas (Hoyas and Jiménez, 2006)), 4079 (Bernardini (Bernardini, Pirozzoli, and Orlandi, 2014)), 4200 (Adrian (Lozano-Durán and Jiménez, 2014)), and 5895 (Lee (Lee and Moser, 2015)). Table 5.3 presents a comparison between the characteristics of the grids used in the present study and those detailed in the reference papers for shear Reynolds numbers of 180, 395, and 590. The results from Moser ((Moser, Kim, and Mansour, 1999)) are employed for the comparative analysis in section 5.2.2.

TABLE 5.3: Characteristics of the grids in the current study and related literature. Re_τ is the friction Reynolds number, δ is the half height of the simulation domain, L_x , L_z , L_y are the length of the domain in the streamwise, spanwise, and wall-normal directions, respectively. N_x , N_z , and N_y are the grid number in the streamwise, spanwise, and wall-normal directions, respectively. Notably, the grids in the x and z directions are uniformly distributed, but the grids in the y direction are exponentially distributed from dense to sparse from the wall outward. More details can be found in (Vuorinen and Keskinen, 2016)

| Year | Author | Method | Re_τ | L_x | L_z | L_y | N_x | N_z | N_y |
|---------|---------------------------------------------|--------|-----------|----------------|------------------------|-----------|-------|-------|-------|
| 1987 | Kim (Kim, Moin, and Moser, 1987) | DNS | 180 | $4\pi\delta$ | $2\pi\delta$ | 2δ | 192 | 160 | 129 |
| 1999 | Moser (Moser, Kim, and Mansour, 1999) | DNS | 180 | $4\pi\delta$ | $\frac{4\pi\delta}{3}$ | 2δ | 128 | 128 | 129 |
| 2006 | Hu (Hu, Morfey, and Sandham, 2006) | DNS | 180 | 24 | 12 | 2 | 256 | 256 | 121 |
| Present | This study | DNS | 180 | $2\pi\delta$ | $\pi\delta$ | 2δ | 72 | 72 | 74 |
| Present | This study | LES | 180 | $2\pi\delta$ | $\pi\delta$ | 2δ | 36 | 36 | 38 |
| 1999 | Moser (Moser, Kim, and Mansour, 1999) | DNS | 395 | $2\pi\delta$ | $\pi\delta$ | 2δ | 256 | 192 | 193 |
| 2002 | Iwamoto (Iwamoto, Suzuki, and Kasagi, 2002) | DNS | 400 | $2.5\pi\delta$ | $\pi\delta$ | 2δ | 192 | 192 | 257 |
| 2004 | Tanahashi (Tanahashi et al., 2004) | DNS | 400 | $2\pi\delta$ | $\pi\delta$ | 2δ | 256 | 192 | 385 |
| Present | This study | DNS | 395 | $2\pi\delta$ | $\pi\delta$ | 2δ | 120 | 120 | 92 |
| Present | This study | LES | 395 | $2\pi\delta$ | $\pi\delta$ | 2δ | 72 | 72 | 74 |
| 1999 | Moser (Moser, Kim, and Mansour, 1999) | DNS | 590 | $2\pi\delta$ | $\pi\delta$ | 2δ | 384 | 384 | 257 |
| 2002 | Iwamoto (Iwamoto, Suzuki, and Kasagi, 2002) | DNS | 650 | $2.5\pi\delta$ | $\pi\delta$ | 2δ | 288 | 384 | 257 |
| 2003 | Alamo (Del Alamo et al., 2004) | DNS | 550 | $\pi\delta$ | $\frac{\pi\delta}{2}$ | 2δ | 192 | 192 | 257 |
| Present | This study | DNS | 590 | $2\pi\delta$ | $\pi\delta$ | 2δ | 200 | 200 | 102 |
| Present | This study | LES | 590 | $2\pi\delta$ | $\pi\delta$ | 2δ | 72 | 72 | 74 |

5.2.2 Validation and comparison

a) Comparison with DNS data

Referring to Table 5.3, the validation process begins with the separate assessment of the CFD part, using both DNS and LES methods. Figures 5.5, 5.6, and 5.7 show the validations for $Re_\tau=180, 395,$ and $590,$ respectively. In each figure set, (a), (c), and (e) represent results obtained through the DNS method, while (b), (d), and (f) denote outcomes derived from the LES method. Specifically, (a) and (b) exhibit the mean velocity profiles in wall coordinates, (c) and (d) depict root-mean-square (RMS) velocity profiles in wall coordinates, and (e) and (f) present Reynolds shear stress in wall coordinates. Upon comparison with the benchmark DNS results ((Moser, Kim, and Mansour, 1999)) across varying Re_τ values, this study's findings demonstrate notable consistency. However, in the LES method, an over-prediction in the peak value

of the stream-wise velocity fluctuation U^+ occurred in comparison to the benchmark DNS result. This discrepancy stems from the LES model's suboptimal optimization and insufficient grid refinement. Nonetheless, these LES results, when contrasted with other LES models ((Golshan et al., 2015)), meet the precision requisites, making them acceptable for this study's objectives. Considering the trade-off between computational resources and accuracy, these parameter settings in the CFD part of the subsequent hybrid method are acceptable and are employed for further analyses.

b) Comparison between DNS-DPD and LES-DPD

The comparison between DNS-DPD and LES-DPD results is depicted in Fig. 5.8. Case 1, utilizing the LES-DPD method, and Case 7, utilizing DNS-DPD, are detailed in Table 5.1. Both cases show nearly identical DR and Re_τ values. In Fig. 5.8 and 5.9, the polymer solutions employing the hybrid method are represented by open blue circles and red squares, while the Newtonian fluid using only the CFD method is depicted by solid black dots and black asterisks. From Fig. 5.8, the upper regions of Cases 1 and 7 demonstrate consistency. Notably, for the polymer solution influenced by DPD, similar upward shifts in the profiles are observed once y^+ surpasses 30. Fig. 5.9a-5.9c display rising RMS velocity fluctuations in the streamwise direction while demonstrating declines in the wall-normal and spanwise directions. This trend is consistently followed by both Cases 1 and 7, as evidenced by the Reynolds stress curves reported in Fig. 5.9d, emphasizing their identical $DR(\%)$.

c) Comparison between LES-DPD and FENE

In this section, we explore the relationship between Den and $DR(\%)$ using the

TABLE 5.4: Parameters for the cases using FENE method from reference (Dallas, Vassilicos, and Hewitt, 2010). Here, Re_τ is the friction Reynolds number, We_c is the Weissenberg number, We_{τ_0} is the friction Weissenberg number, and $DR(\%)$ is calculated by Eq[5.29]

| Case | Method | Re_τ | We_c | We_{τ_0} | $DR(\%)$ |
|------|--------|-----------|--------|---------------|----------|
| A | FENE | 167 | 2 | 15.4 | 14.2 |
| B | FENE | 147 | 3 | 30.8 | 33.8 |
| N2 | DNS | 181 | 0 | 0 | 36.6 |

FENE method. Table 5.4 summarizes the FENE method's features alongside several cases studied by Dallas et al. (Dallas, Vassilicos, and Hewitt, 2010). Parameters such as We_c and We_{τ_0} relate to the polymer relaxation time; further details can be found in (Dallas, Vassilicos, and Hewitt, 2010). Fig. 5.10 illustrates the results for the Newtonian fluid from Cases 1, 2, and 3 (denoted by black dots), employing the LES method as listed in Table 5.1. These results are close to those of Case N2, representing the Newtonian fluid across the entire region. Subsequently, attention is focused on the lower region of Cases 1, 2, and 3, representing the polymer solution using the LES-DPD method. Evidently, as the particle energy density increases, Re_τ decreases, $DR(\%)$ rises, and U^+ away from the wall exhibits a consistent upward trend. Notably, the shift distances for Cases A and 1, with identical DR and Re_τ , are close (the blue circle and asterisk in Fig. 5.10-5.11). Similarly, under the same DR and Re_τ , the profiles of Cases B and 3 exhibit identical and maximal shifts (the green star and multiplication sign in Fig. 5.10-5.11). Fig. 5.11 demonstrates a consistent trend in the results for RMS velocity and Reynolds shear stress, despite minor discrepancies

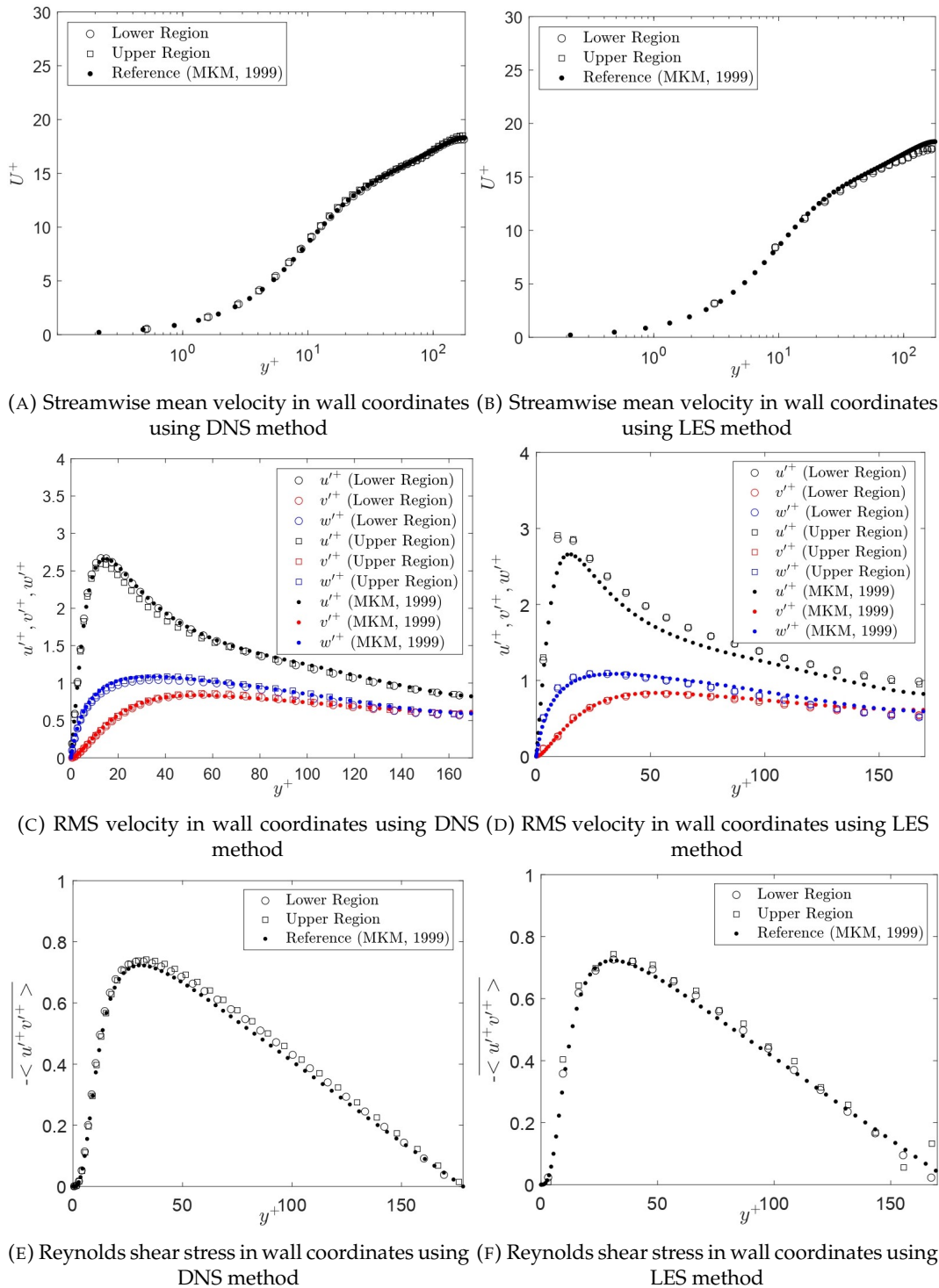


FIGURE 5.5: Comparison between results with $Re_\tau=180$ using DNS/LES method in this study with the reference (Moser, Kim, and Mansour, 1999)(DNS)

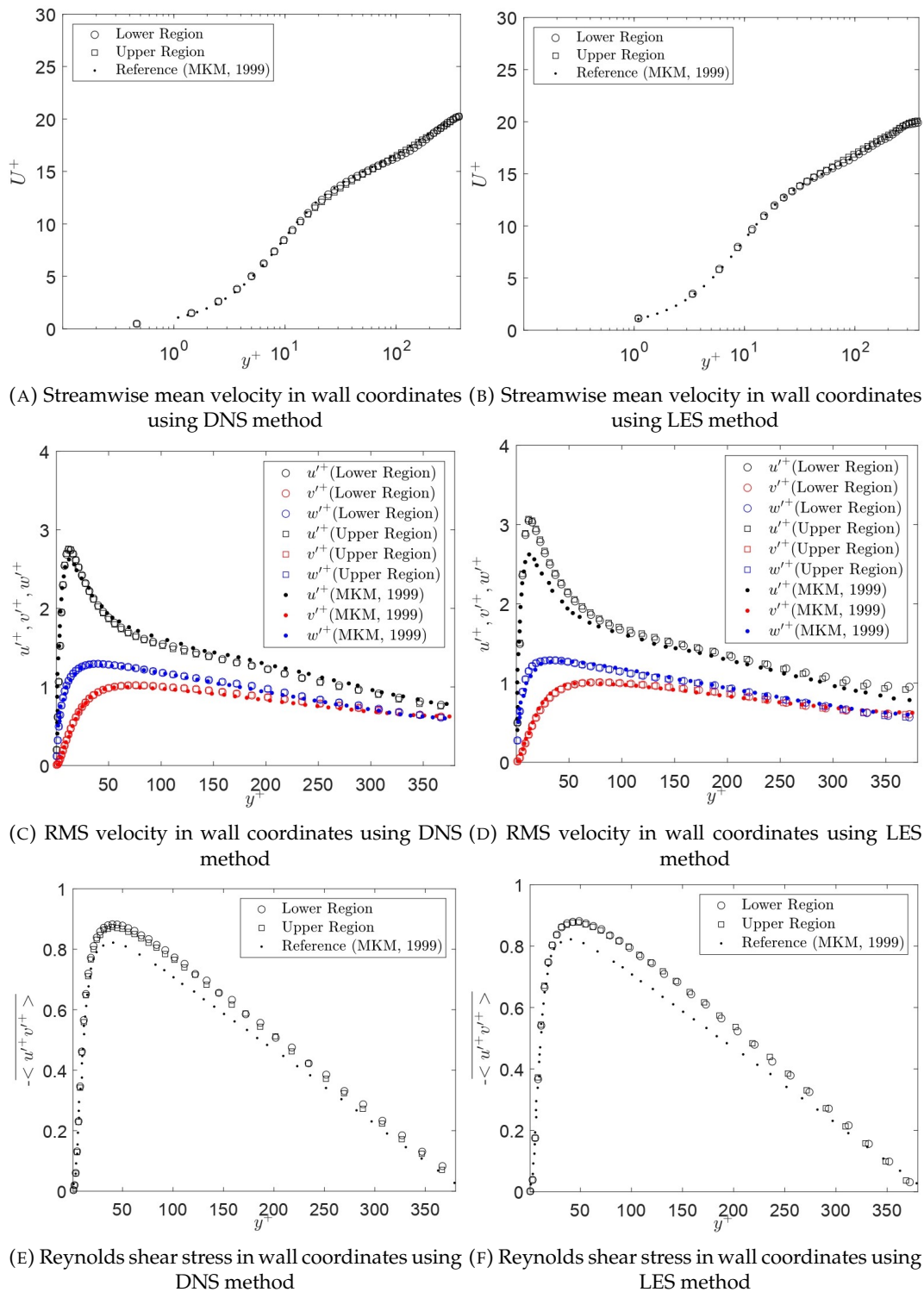


FIGURE 5.6: Comparison between results with $Re_\tau=395$ using DNS/LES method in this study with the reference (Moser, Kim, and Mansour, 1999)(DNS)

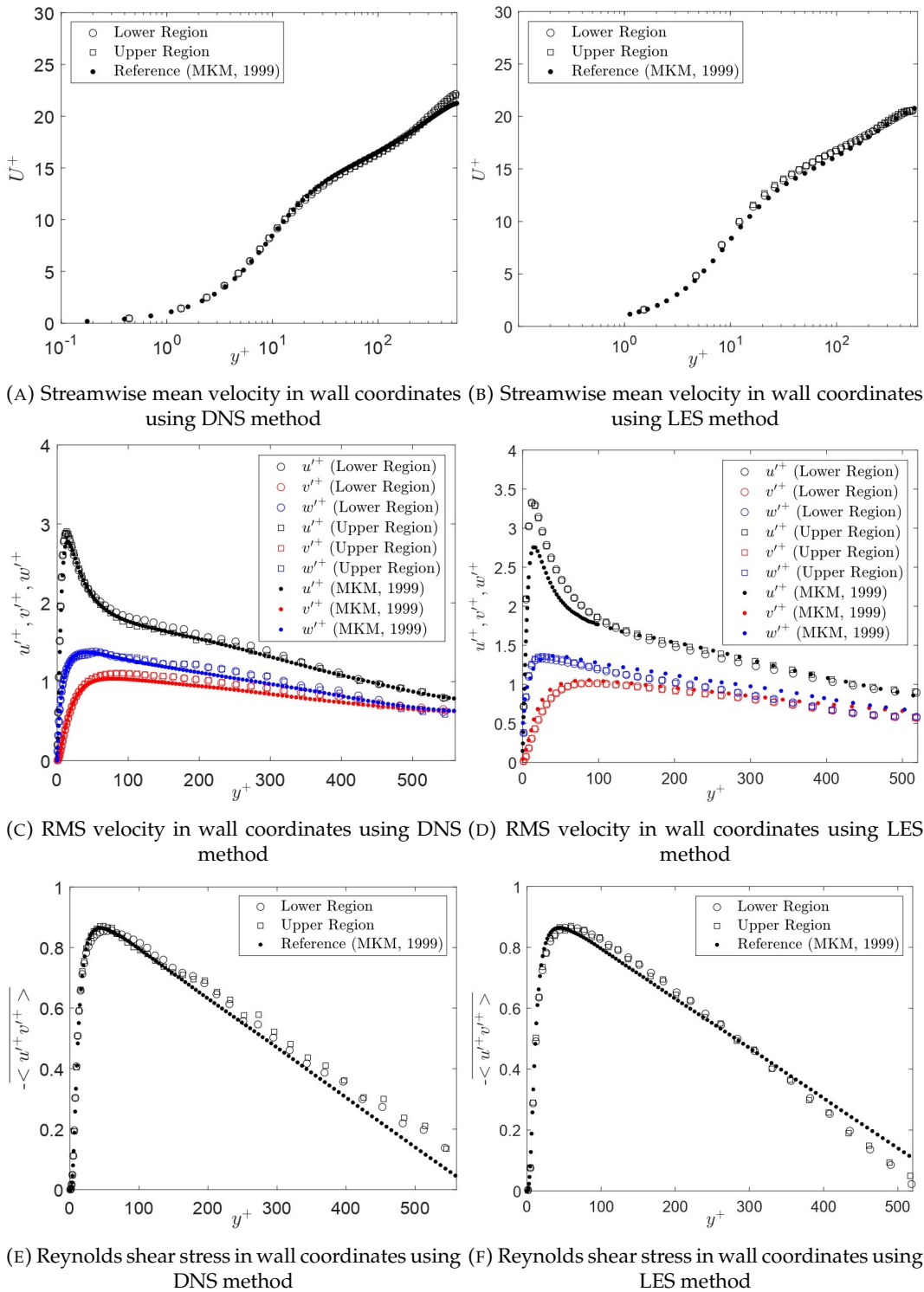


FIGURE 5.7: Comparison between results with $Re_\tau=590$ using DNS/LES method in this study with the reference (Moser, Kim, and Mansour, 1999)(DNS)

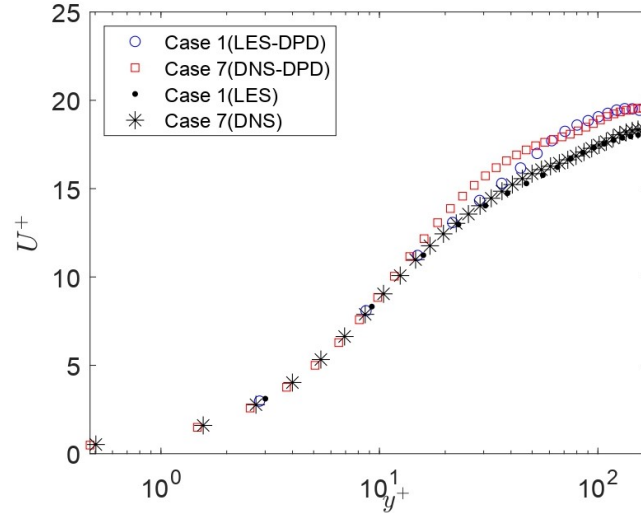


FIGURE 5.8: Comparison between Cases 1 and 7's profiles in wall coordinates of the streamwise mean velocity. Open blue circle: the polymer solution using LES-DPD method in the lower region of Case 1. Open red square: the polymer solution using DNS-DPD method in the lower region of Case 7. Solid black dot: the Newtonian fluid using LES method in the upper region of Case 1. Black asterisk: the Newtonian fluid using DNS method in the upper region of Case 7.

stemming from differences between the DNS and LES methodologies. With heightened DPD particle influence (Den), RMS velocity fluctuations in the wall-normal and spanwise directions decrease, while the Reynolds shear stress increases.

Comparatively, our model demonstrates the same capability as the FENE method in characterizing the DR of the polymer solution. Moreover, utilizing DPD particles to represent polymer properties doesn't impact the original fluid grids or algorithms, ensuring seamless integration into existing frameworks. Additionally, the DPD method, a coarse-grained molecular simulation algorithm, efficiently captures polymer molecular group properties while optimizing computational resources.

5.2.3 Effect of Reynolds number

This section explores the impact of Reynolds numbers, examining the performance of Cases 2, 8, and 9 as outlined in Table 5.1. Figures 5.12 to 5.14 offer a comparative analysis between the Newtonian fluid behavior of Case 9, modeled using the LES method, and the polymer solutions of Cases 2, 8, and 9, simulated via the LES-DPD method. The mean velocity profile for the Newtonian fluid of Case 9 adheres closely to the log-law profile. Comparatively, the profiles for Cases 2, 8, and 9 exhibit upward shifts and a slight reduction in their elevations with increasing Reynolds numbers. Notably, for $y^+ < 5$, these curves align, indicating no change in the thickness of the 'viscous sublayer'. However, the subsequent 'buffer layer' maintains consistent thickness among these three cases within the range of $5 < y^+ < 32$, which surpasses that of the Newtonian fluid within $5 < y^+ < 30$. This suggests that the buffer layer thickens with the introduction of DPD polymer, retaining the same thickness across different Re_τ when $DR(\%)$ remains constant. As velocity escalates in the buffer layer, the logarithmic layer maintains a consistent slope but exhibits lower intercepts; specifically, the intercepts (denoted by 'b') for Cases 2, 8, and 9 in Fig.

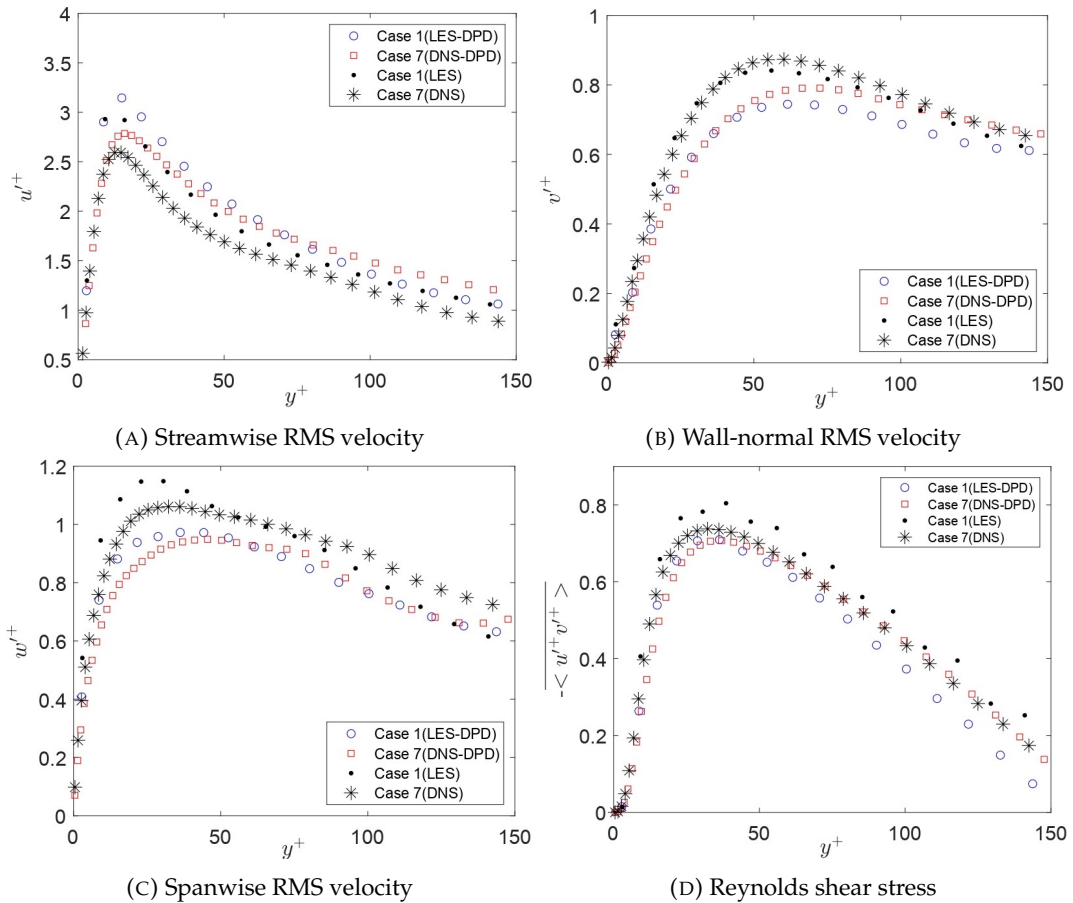


FIGURE 5.9: Comparison between the curves for Cases 1 and 7 in wall coordinates. Open blue circle: the polymer solution using LES-DPD method in the lower region of Case 1. Open red square: the polymer solution using DNS-DPD method in the lower region of Case 7. Solid black dot: the Newtonian fluid using LES method in the upper region of Case 1. Black asterisk: the Newtonian fluid using DNS method in the upper region of Case 7.

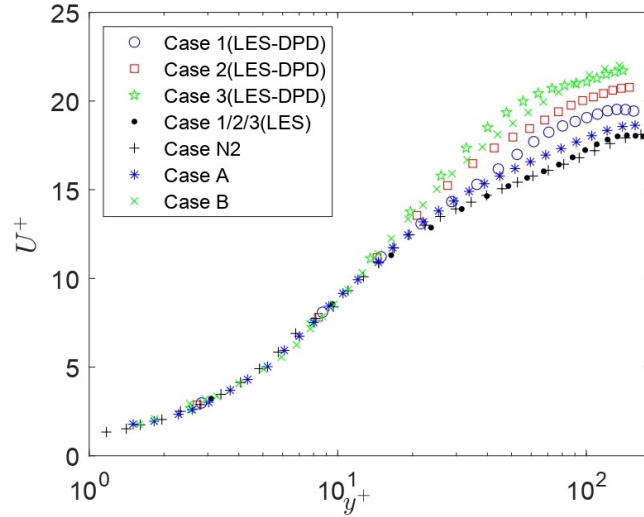


FIGURE 5.10: Comparison between Cases 1, 2 and 3's profiles of the streamwise mean velocity. Open blue circle: the polymer solution using LES-DPD method in the lower region of Case 1. Open red square: the polymer solution using LES-DPD method in the lower region of Case 2. Open green star: the polymer solution using LES-DPD method in the lower region of Case 3. Solid black dot: the Newtonian fluid using LES method in the upper region of Cases 1, 2 and 3. Details about Case N2, A and B can be seen in Table 5.4 and (Dallas, Vassilicos, and Hewitt, 2010)

5.12 are 4.8, 5.1, and 5.7, respectively. Figures 5.13 and 5.14 present the vortex cross-section and q-criterion for visualizing vortex behavior at various Reynolds numbers. The polymer solution in the lower region (Fig. 5.13) displays reduced vortex turbulence compared to the Newtonian fluid in the upper region (Fig. 5.14). Furthermore, the polymer solution exhibits more localized vortex dispersion. In summary, the numerical model effectively captures the impact of DR across diverse Reynolds values, demonstrating its robustness across varied flow conditions.

5.2.4 Effect of polymer layer

The subsequent examination focuses on the impact of varying heights of the DPD particle region on DR . Specifically, Cases 4, 5, and 6, featuring H_{DPD} at $\frac{1}{3}\delta$, $\frac{1}{2}\delta$, and δ , are chosen while maintaining a consistent Den across these cases. The distribution of DPD particles for these three cases is presented in Fig. 5.15. A noteworthy observation is the positive correlation between H_{DPD} and $DR(\%)$. This correlation becomes apparent when examining the mean velocity profile in Fig. 5.16, which demonstrates an increasing trend as H_{DPD} increases. Interestingly, despite Case 5 having only half the H_{DPD} of Case 6, its mean streamwise velocity profile and DR closely resemble those of Case 6. In particular, Case 5 stands out with the highest DR efficiency, calculated as $\frac{DR}{H_{DPD}}$, at 82.6%, surpassing Cases 4 and 6, which record values of 3.6% and 58.6% respectively. This highlights the efficiency of Case 5 in achieving substantial drag reduction relative to its polymer region height.

As H_{DPD} increases, a decrease in velocity fluctuation in both the wall-normal and spanwise directions is evident in Fig. 5.17b and 5.17c. This suggests a reduced redistribution of momentum in these directions. Concurrently, the Reynolds shear stress in both the 'viscous sublayer' and 'buffer layer' diminishes as H_{DPD} increases,

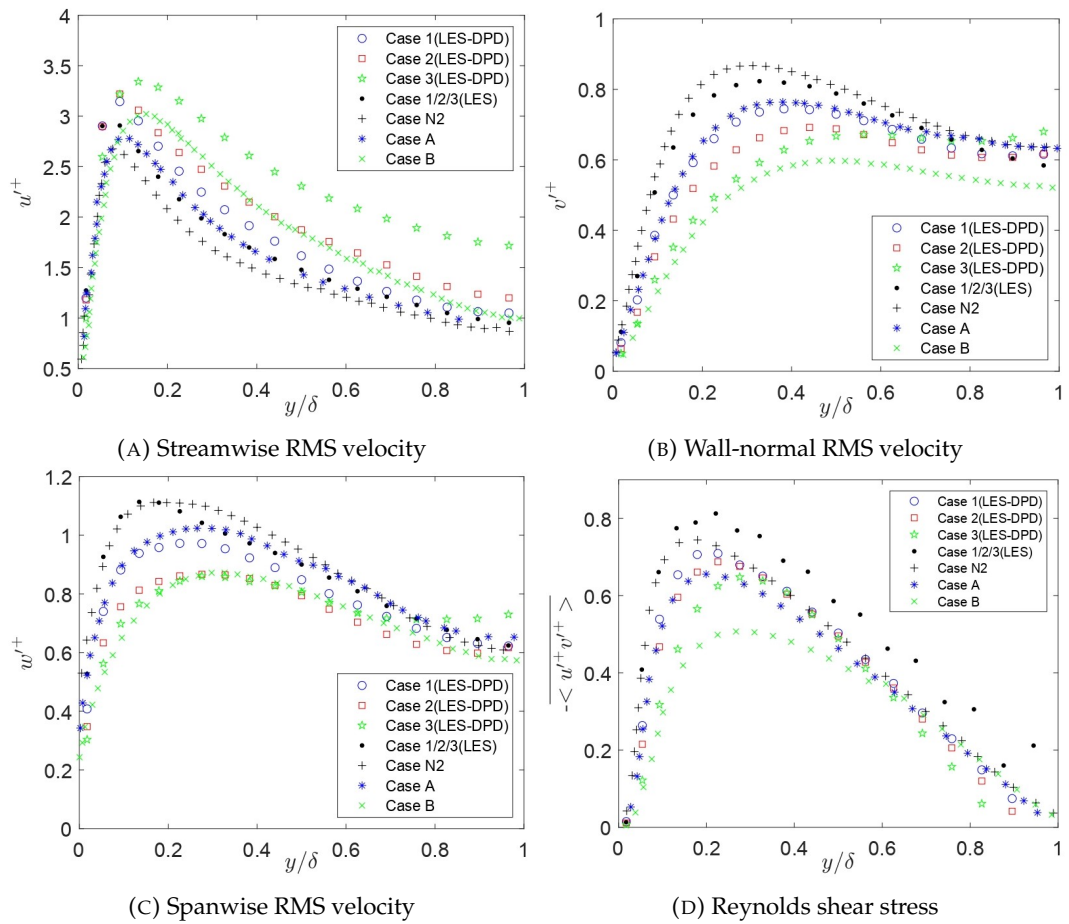


FIGURE 5.11: Comparison of turbulent intensity and Reynolds stress among Case 1, 2 and 3. Open blue circle: the polymer solution using LES-DPD method in the lower region of Case 1. Open red square: the polymer solution using LES-DPD method in the lower region of Case 2. Open green star: the polymer solution using LES-DPD method in the lower region of Case 3. Solid black dot: the Newtonian fluid using LES method in the upper region of Case 1, 2 and 3. Details about Case N2, A and B can be seen in Table 5.4 and (Dallas, Vassilicos, and Hewitt, 2010)

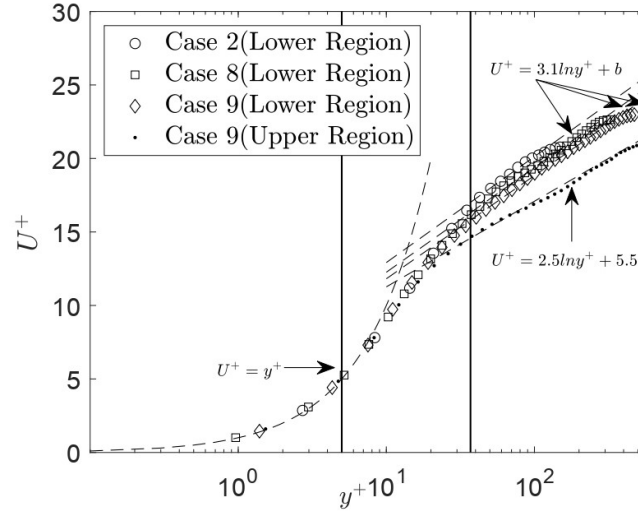


FIGURE 5.12: Comparison of streamwise mean velocity in wall coordinates for Cases 2, 8 and 9. Open circle: the polymer solution with $Re_\tau=180$. Open square: the polymer solution with $Re_\tau=395$. Open diamond: the polymer solution with $Re_\tau=590$. Solid dot: Newtonian fluid using LES method in the upper region of Case 9. Dotted line: Linear viscous relation and logarithmic overlap layer. 'b' of cases 2, 8 and 9 is 4.8, 5.1 and 5.7, separately.

as depicted in Fig. 5.17d. Conversely, there's a more effective transport of streamwise momentum with the escalating H_{DPD} , as shown in Fig. 5.17a. An important observation in Fig. 5.17b is the reduction in velocity fluctuations in the wall-normal direction within the range less than H_{DPD} . However, beyond H_{DPD} , these fluctuations increase slightly or even surpass those of the Newtonian liquid. This phenomenon occurs because the vortex regenerates and grows at the critical surface, a phenomenon intuitively observed in Fig. 5.18-5.19.

Fig. 5.18 and 5.19 show the vortex according to the Q criterion. Fig. 5.18, derived from the DNS-DPD method, and Fig. 5.19, from the DNS method, represent the instantaneous outcomes of the same simulation domain at the final time step. Top and side perspectives are displayed for all three cases. Comparing the top views in Fig. 5.18a, 5.18c, and 5.18e to those without DPD particles in Fig. 5.19a, 5.19c, and 5.19e, the vortex appears smaller and more localized in the former. In the side view of Case 4 (Fig. 5.18b), the vortex initiates growth from the wall, with a less pronounced reduction. However, in Case 5's side view (Fig. 5.18d), the vortex near the wall vanishes. From $y^+ = 40$, the vortex gradually reappears, a pattern observed in Case 6 (Fig. 5.18f), where the vortex starts at $y^+ = 100$ and quickly diminishes. This demonstrates the ability of DPD particles to locally control the vortex and reduce velocity fluctuations in both the wall-normal and spanwise directions. Additionally, this study's model can effectively explore the impact of polymers on DR in various regions. This exploration includes understanding the influence of concentration distribution on DR due to the polymer solution's position of incidence, as well as the DR effects of polymer coatings.

5.2.5 Estimation and harvesting of turbulent energy

Based on the results above, We can analyze the mechanism behind the phenomenon of drag reduction from the perspective of turbulence production and dissipation. In

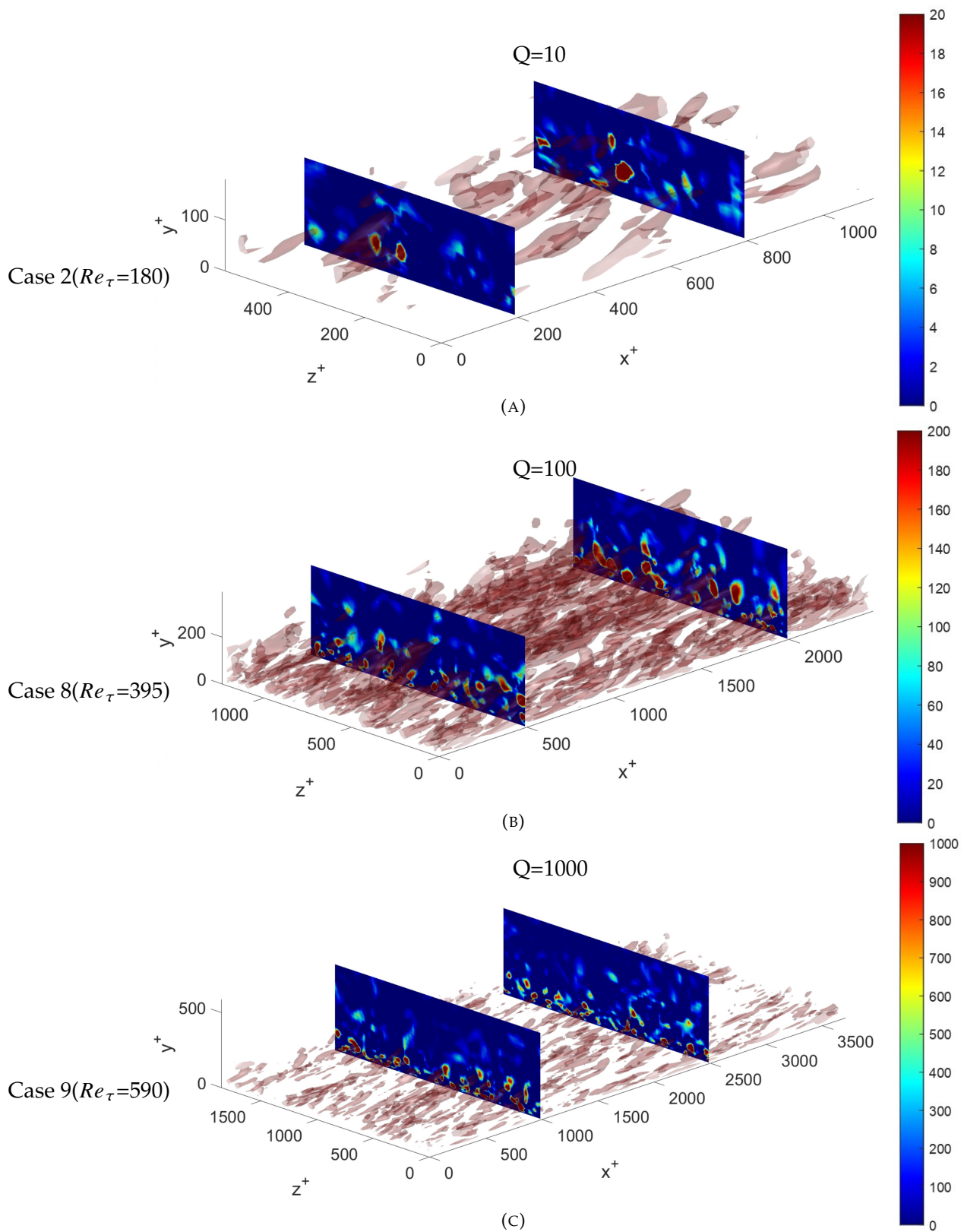


FIGURE 5.13: Q-criterion for vortex visualisation at different Reynolds numbers using LES-DPD

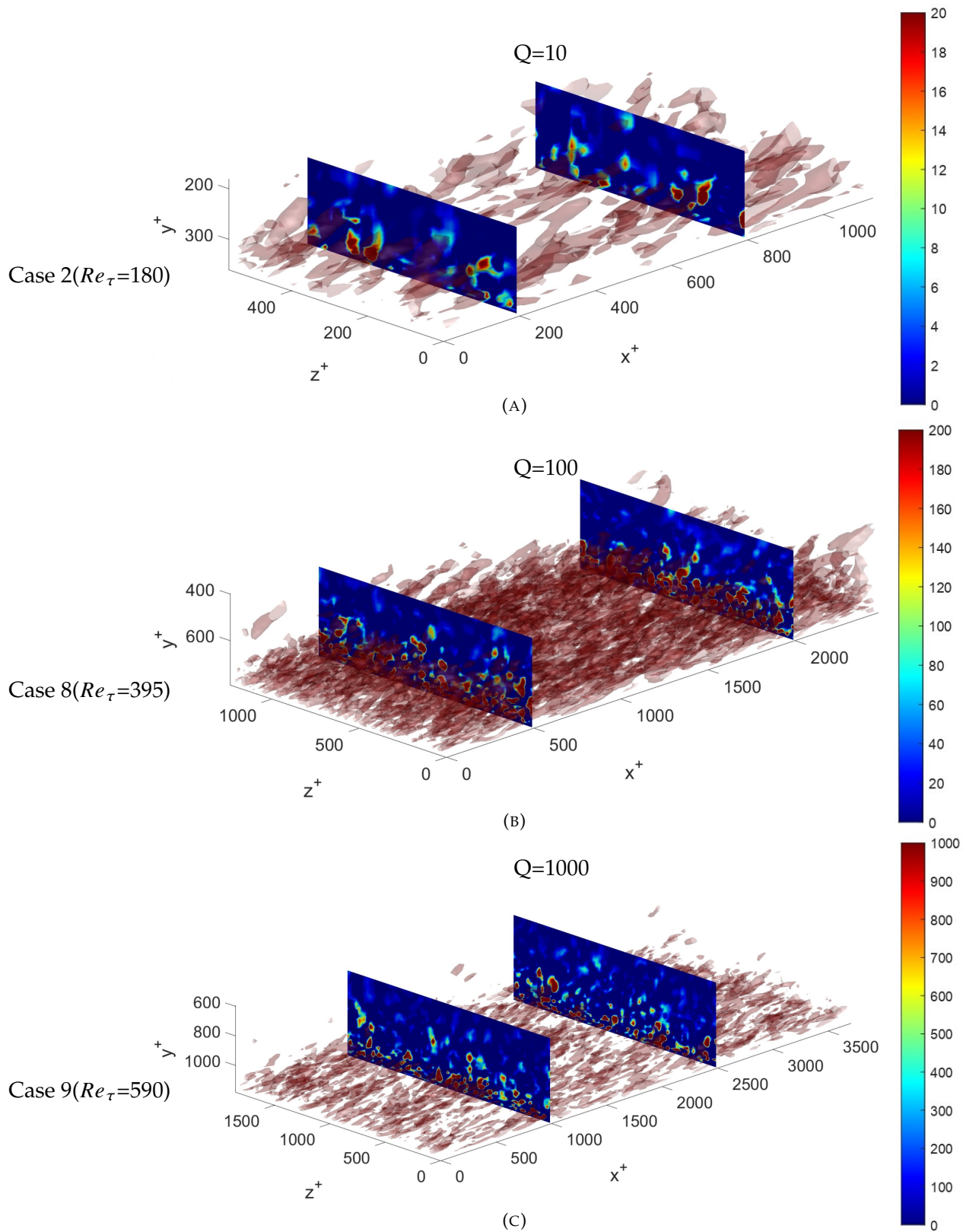
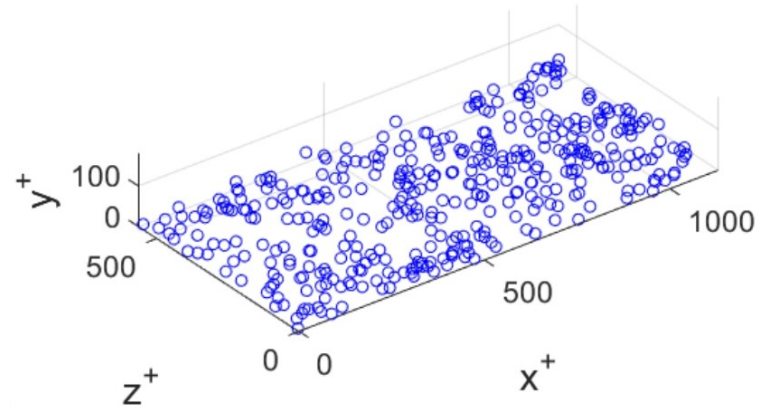
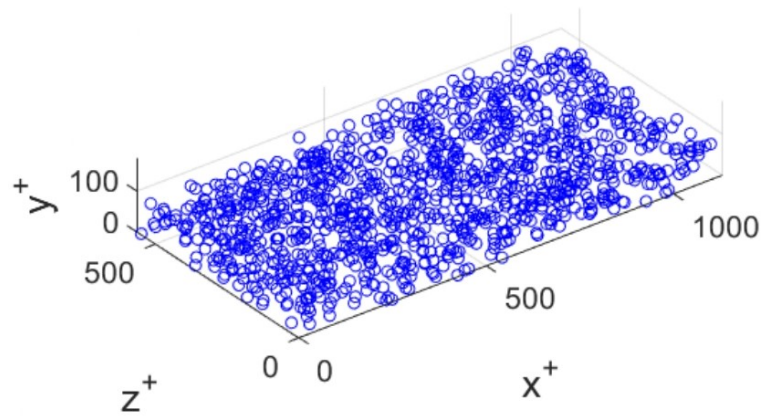


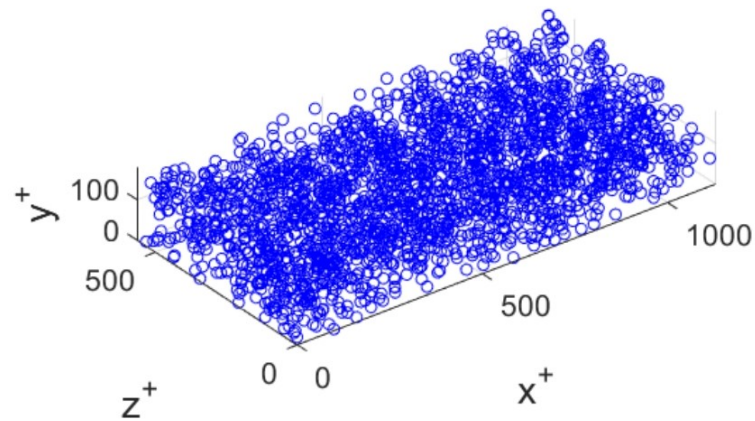
FIGURE 5.14: Q-criterion for vortex visualisation at different Reynolds numbers using LES



(A) Case $4(\frac{1}{3}\delta)$



(B) Case $5(\frac{1}{2}\delta)$



(C) Case $6(\delta)$

FIGURE 5.15: Distribution of DPD particles in Cases 4, 5 and 6

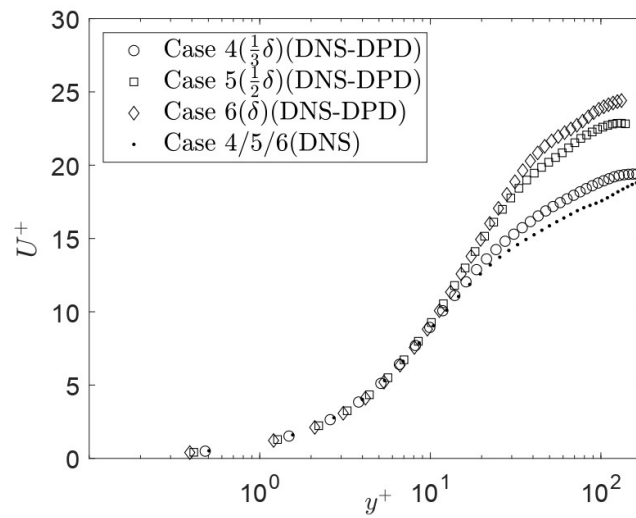


FIGURE 5.16: Comparison of the vertical distribution of streamwise mean velocity in wall coordinates in Cases 4, 5 and 6

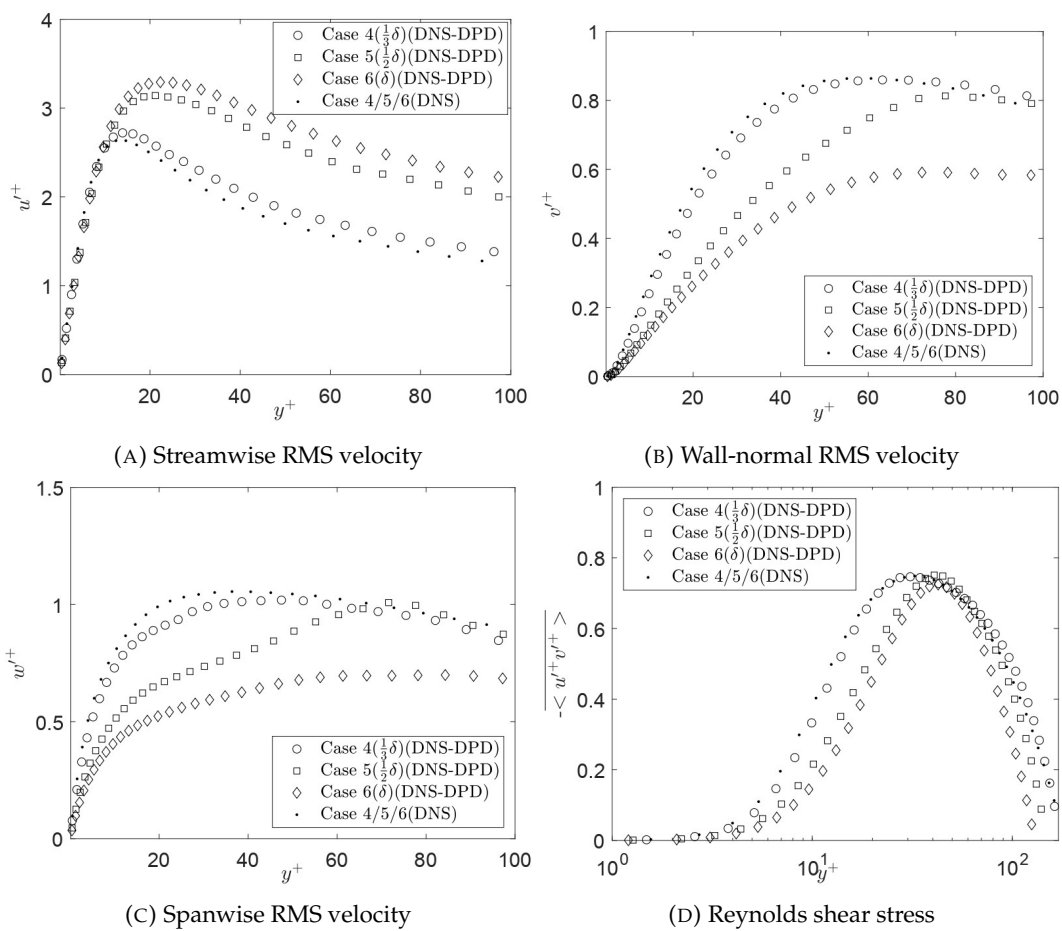


FIGURE 5.17: Comparison of RMS and Reynolds shear stress in Cases 4, 5 and 6

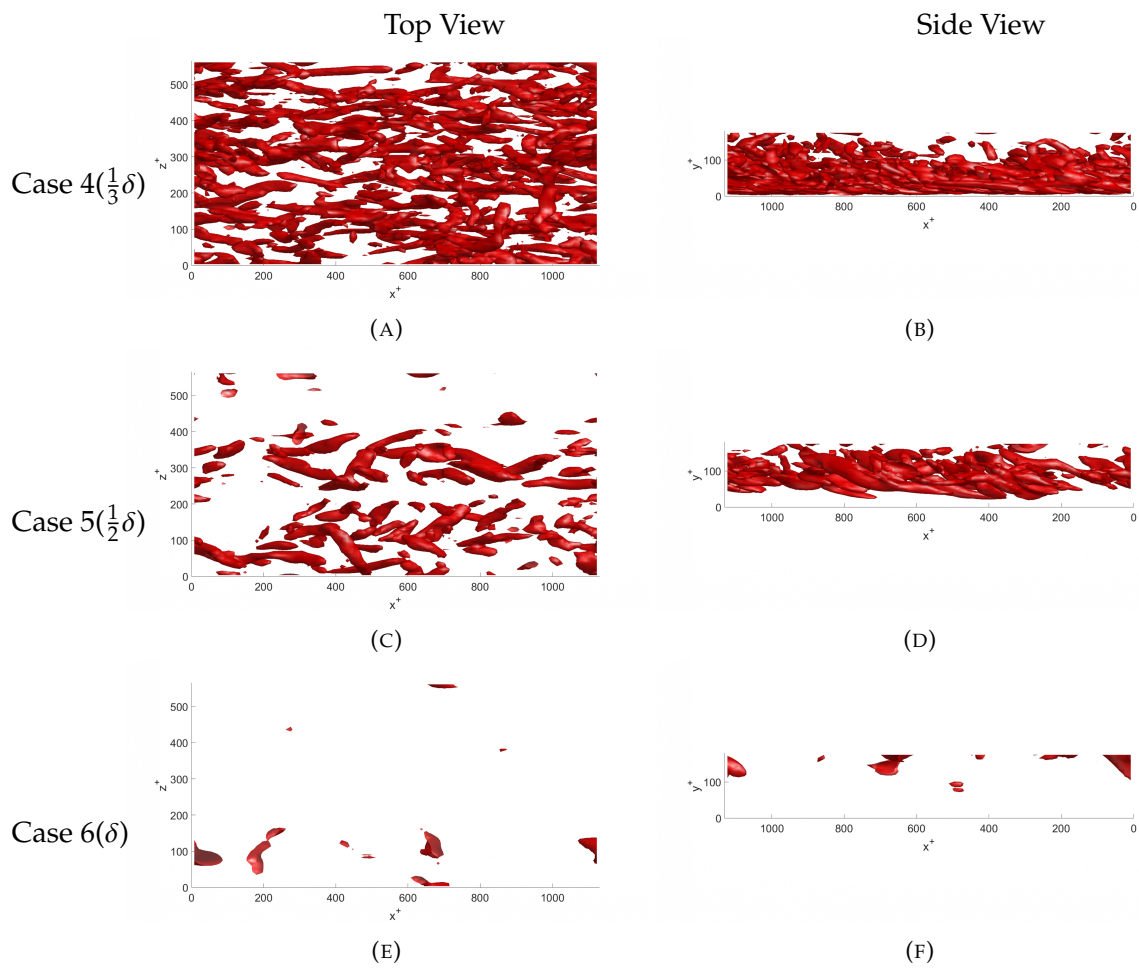


FIGURE 5.18: Vortex of the Q criterion using the DNS-DPD method

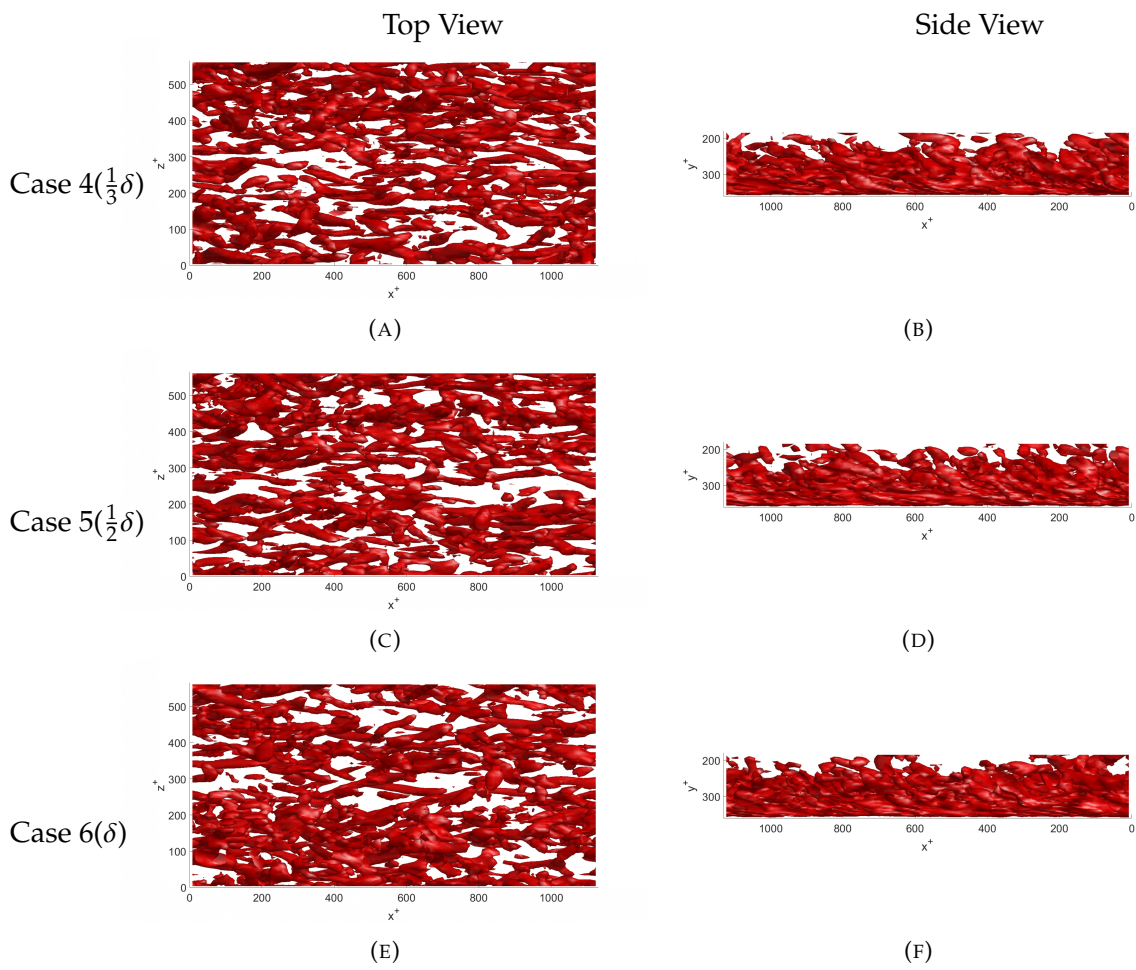


FIGURE 5.19: Vortex of the Q criterion using the DNS method

addition, several prospects for combining with energy harvesting devices are proposed. By controlling flow field with polymer coating, PENG/TENG can be motivated to the maximum extent.

Firstly, in Fig. 5.20, the turbulence generation and dissipation are depicted for Cases 4, 5, and 6 utilizing the hybrid DNS-DPD approach. Conversely, the Newtonian fluid is represented by black dots only using the DNS method. Fig. 5.20a reveals a distinct declining trend in the peak of turbulence generation profiles as H_{DPD} increases. This trend is notably apparent in the peak values, which shift rightwards along the x -axis. For instance, in Case 4, the peak occurs at $y^+ = 16$, deviating from the Newtonian Case, which peaks at $y^+ = 10$. Similarly, Cases 5 and 6 also display a rightward shift of the peak to $y^+ = 19$ and 22 , respectively. Examining the region proximal to the wall in Fig. 5.20b, the turbulent dissipation for the three cases demonstrates a consistent and steady decline, with Cases 5 and 6 exhibiting more significant drops. As referenced, the dissipation of turbulent energy occurs due to the polymer viscosity, while the elasticity of the particles absorbs it. This demonstrates the model's capability to explain the polymer particles' drag reduction in terms of energy, viscosity, and elasticity simultaneously.

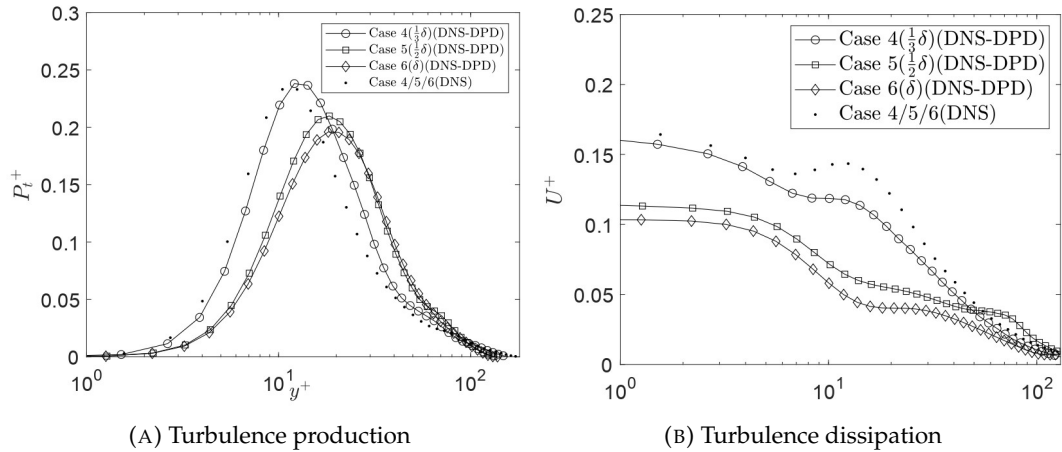


FIGURE 5.20: Comparison of turbulence production and dissipation in Cases 4, 5, and 6

In Fig. 5.22, notably high fluid dissipation is observed in regions of intense turbulence. The red isosurface indicates the vortex ($Q=10$), while the blue isosurface marks areas with a significant component of viscous dissipation fluctuation ($\epsilon_t^+=0.3$). Consistent with the formatting in Fig. 5.18 and 5.19, Fig. 5.22 presents the vortex, based on the Q criterion, and turbulence dissipation outcomes employing the DNS-DPD method. Conversely, Fig. 5.23 illustrates the results achieved through the DNS method. These represent instantaneous outcomes derived from identical simulation domains at the final time step. The figures display three distinct cases from oblique and side perspectives. From the oblique viewpoint depicted in 5.23a, 5.23c, and 5.23e, the turbulence within the Newtonian fluid shows extensive turbulence dissipation. Conversely, with an increased H_{DPD} in the polymer solution, the intense turbulence dissipation area diminishes and becomes more concentrated across the entire channel, as evidenced in 5.22a, 5.22c, and 5.22e. From the side view in 5.22b, 5.22d, and 5.22f, high dissipation occurs proximal to the wall and diminishes as H_{DPD} increases. This trend is consistent with the vortex illustrated by the Q criterion.

It can be seen that by adjusting the position and height of the polymer coating, the distribution of turbulence in all directions can be effectively controlled. This is critical for PENGs or TENGs that harvest turbulent energy. As shown in the Fig. 5.18, the piezoelectric device is placed perpendicular to the wall, and the rocking motion of the piezoelectric device under the action of turbulence can be observed through flow visualization. So when the turbulence and intensity near the wall in each direction are controlled by polymers coating as we analysed in the previous section, the vortex frequency can be designed more closely to the natural frequency of the PENGs' or TENGs' beams. Then a suitable flow field can be design for PENGs or TENGs to improve their power generation efficiency. The flow control using polymer coating can be used not only for the wall surface, but also for the interference cylinder. As Fig. 1.7 shows, the working principle of the fluid induced vibration PENG focus on the frequency of vortex shedding. By application of polymer coating and estimation of DNS/LES-DPD method, suitable vortex-induced vibration without structural change of cylinder can be designed for the different structure of PENGs/TENGs.

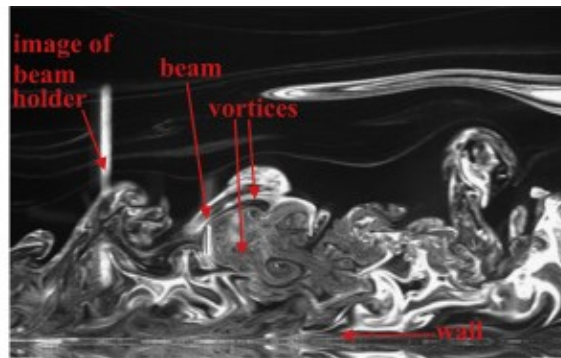


FIGURE 5.21: Flow visualization of turbulent energy harvesting using a PENG (Goushcha et al., 2015).

5.3 Conclusions

In this study, we introduce the DNS/LES-DPD method to simulate polymer distribution within the fluid, enabling the examination of Drag Reduction (DR) on vehicle surfaces in a numerical environment. This approach contributes to research on energy conservation and drag reduction in various marine applications like marine transmission pipelines, marine vehicles, and submarines. To validate our model, we undertook three key steps: (1) We verified the DNS/LES results against established reference data, demonstrating the accuracy and reliability of the CFD aspect in our hybrid model. (2) Comparisons between the DNS-DPD and LES-DPD methods were conducted to determine the suitability of the Large Eddy Simulation (LES) approach in specific conditions. (3) We compared the results of the LES-DPD model against findings from the FENE model to validate the accuracy and effectiveness of our proposed approach. Following validation, we explored the model's suitability for different Reynolds numbers and assessed the performance of the models at three Reynolds numbers under identical DR conditions. Finally, to investigate the DR capability of polymer coatings, we examined the impact of polymer layer thickness. The key findings are summarized as follows:

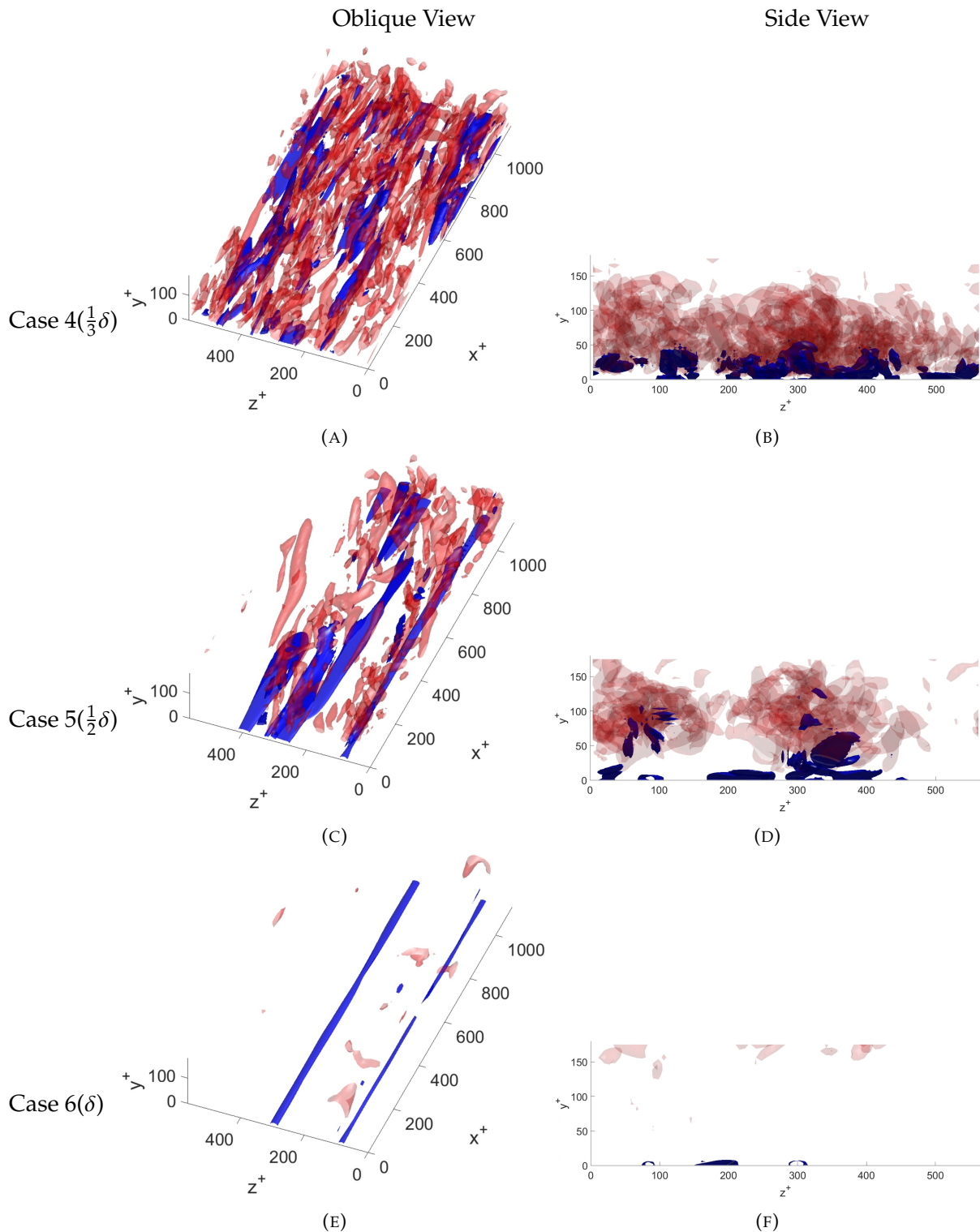


FIGURE 5.22: Vortex of the Q criterion and turbulence dissipation using the DNS-DPD method. Red isosurface: the vortex ($Q=10$). Blue isosurface: turbulence dissipation ($\epsilon_t^+=0.3$).

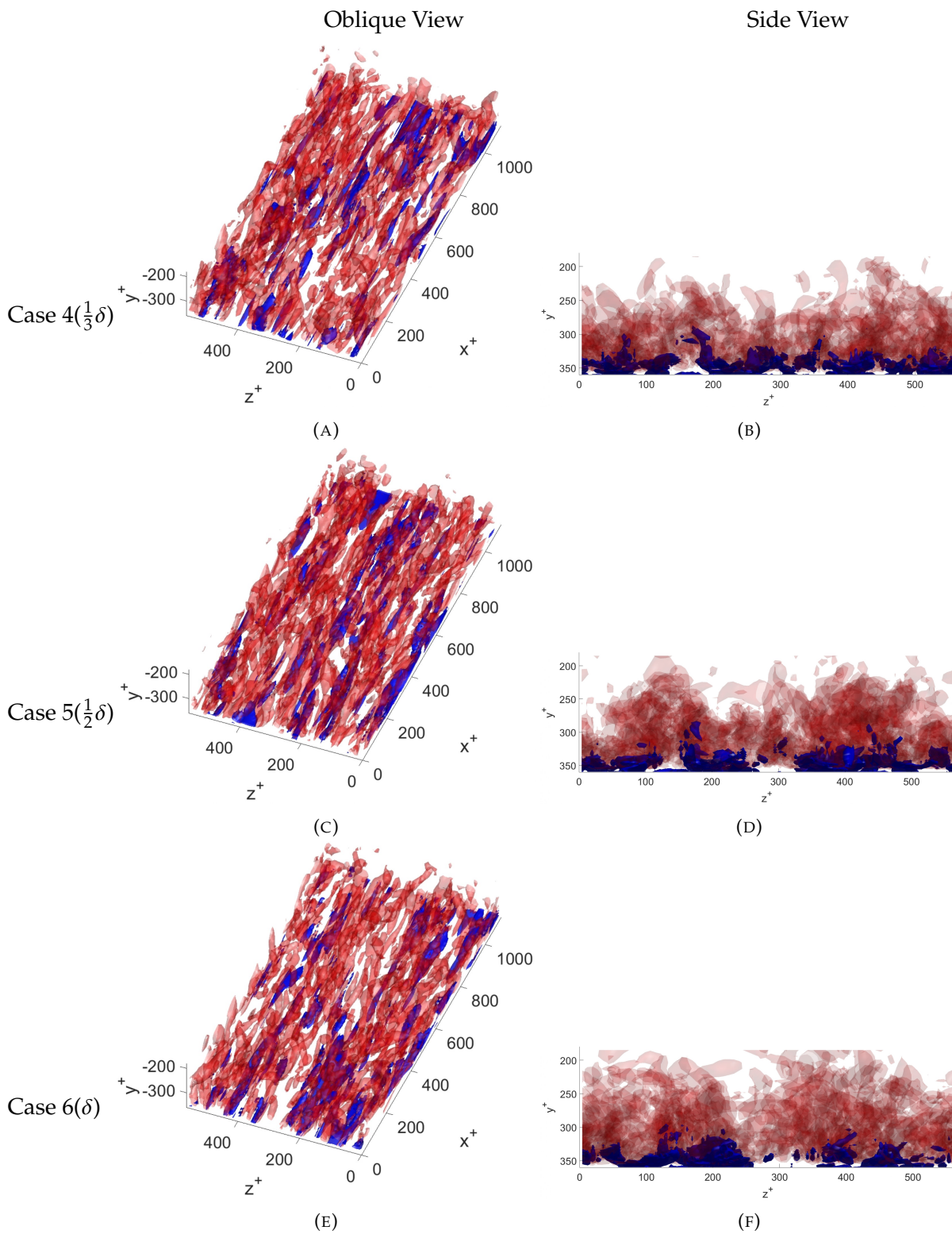


FIGURE 5.23: Vortex of the Q criterion and turbulence dissipation using the DNS method. Red isosurface: the vortex ($Q=10$). Blue isosurface: turbulence dissipation ($\epsilon_t^+=0.3$).

- The model, whether only based on the DNS/LES method or the DNS/LES-DPD method, shows good agreement with results in previous reference, validating its reliability.
- The LES-DPD method exhibits comparable performance to the DNS-DPD method, even with a smaller grid count. This versatility in precision and efficiency is leveraged by employing both DNS-DPD and LES-DPD methods complementarily.
- With an increase in numerical Den , there's a corresponding improvement in DR . Simultaneously, mean velocity, RMS velocity fluctuations, and Reynolds shear stress demonstrate consistent trends.
- The model demonstrates suitability across various Reynolds numbers. The buffer layer thickens with the addition of DPD polymer and maintains its thickness across different Re_τ , ensuring constant DR
- The process of DR shows a shift in high energy dissipation, transitioning from dispersion to concentration.
- When comparing polymer region heights of $\frac{1}{2}\delta$ and δ , their mean streamwise velocity profile and DR exhibit close similarities. Notably, the case with a $\frac{1}{2}\delta$ height demonstrates the highest drag reduction efficiency when evaluating the ratio of DR to the polymer region's height. Simultaneously, near the wall, the vortex diminishes and gradually reappears toward the region without polymer. This suggests the localized control and reduction of velocity fluctuations by DPD particles in both wall-normal and spanwise directions.
- Based on the DNS/LES-DPD method, the specific relationship between polymer coating distribution, turbulence field, and PENG/TENG power generation performance will be explored.

Chapter 6

Conclusions and future works

In the context of the energy crisis, the economy, politics and environment of both developed and developing countries have been significantly affected, which forces people to transform energy as quickly as possible. Like most things, the current methods to face the energy crisis are nothing more than increasing revenue. The ocean has an important impact on it. On the one hand, the ocean is rich in huge renewable energy, which can be converted and utilized through appropriate devices. On the other hand, ocean transportation accounts for a high proportion and product a lot of turbulence energy. How to recycle the turbulent energy based on fluid control has become a major challenge. Therefore, studies about different types of fluid-structure coupling in the ocean has great potential to energy harvesting exploration.

In terms of utilizing ocean energy, this study focuses on the study of wave energy that can be used sustainably at all times. However, due to its variability and strong relationship with people's lives in coastal areas, there is an urgent need to develop a variety of offshore self-powered wave energy collection devices. By reviewing the devices developed by people in the previous research, we found that TENG and PENG are very suitable for use in wave energy harvesting devices because they are not affected by the weather environment and have good response to the low-frequency of wave.

Among many flow control methods, polymer coating is very popular due to its excellent DR and energy absorption effect. However, adding polymers to the solution is not suitable for marine transportation equipment, so this study considers the use of polymer coatings. However, the numerical method for flow control of polymer coatings has not been clear yet, so this research will propose a numerical algorithm that can be used for local flow control and DR . In this chapter, the conclusions and recommended future works in the presented work are summarized:

6.1 Conclusions

6.1.1 Experimental and numerical research about the selection of working parameter of FPED attached to FAD

- FPEDs are developed and evaluated in this study to supply power to data collection and marine monitoring in FAD.
- Some key parameters including submerged depth and the support-type are selected. The maximum output voltage notably increases with the steepness, especially evident when utilizing cantilever support, because of the substantial deformation and strain rates within the piezoelectric material.
- For the submerged depth, the maximum output voltages are nearly double or triple those observed at $d/L = 0.5$, compared with higher wave steepness

(H/λ) at a depth of $d/L = 1.0$. This substantial increase is due to pronounced deformation of the painted FPED at $d/L = 1.0$, experiencing a larger area of impact from wave forces.

- For the thickness, a thickness of $50 \mu\text{m}$ exhibits significantly higher maximum output voltage due to the relatively lower rigidity of the FPED. This facilitates easier deformation by waves. Hence, determining piezo material thickness should factor in its flexibility against wave-induced stresses.
- To compute fluid-structure interaction directly between the FPED and waves using iterative coupled solutions, an IBM-based theoretical model is devised. The IBM-based computational model successfully predicts the electrical power generated by the painted FPED. Generally, computational outcomes align well with experimental results, showing an almost linear relationship between the maximum output voltage and wave steepness (H/λ) .
- Painted FPEDs show good performance when experiencing extreme weathering, bending, and fatigue endurance. A remote WiFi access monitoring system measures the painted FPED's output voltage, showing that the most substantial power obtained aligns with observations from experimental data.

6.1.2 Experimental and numerical studies on the optimization of HSO-TENGs

- The HSO-TENG, proposed in this research, demonstrates robust power generation and effective wave monitoring capabilities following a series of optimizations.
- Optimization of three structural parameters, including the weight of the magnet mass, the hammer's height, and the external swing arm's length, results in substantial enhancements in average voltage generation by 33%, 62%, and 50%.
- Uni-directional and multi-directional numerical wave tanks are built using the SPH method to find the most suitable fixed condition of the HSO-TENGs for sensing wave changes, and its ability to monitor the wave direction and spreading parameters.
- The optimized HSO-TENG exhibits impressive responses to various wave characteristics including wave height, period, frequency, direction, and spreading parameters, as evidenced by output voltage data obtained from large-scale wave tank experiments and numerical circular wave tank simulations.
- The maximum voltage output reaches 15V, and when the four SO-TENGs are connected in parallel, they sustainably power a temperature and humidity sensor.

6.1.3 Numerical study on drag reduction and turbulence energy based on polymer coating

- The DNS/LES-DPD method is developed successfully to simulate polymer distribution within the fluid, enabling the examination of DR on surfaces in a numerical environment, which can be applied to marine transmission pipelines, marine vehicles, and submarines.

- The results of the DNS/LES or the DNS/LES-DPD method are validated by established reference data, demonstrating the accuracy and reliability of the hybrid model.
- Comparisons between the DNS-DPD and LES-DPD methods were conducted to determine the suitability of the LES approach in specific conditions. The LES-DPD method exhibits comparable performance to the DNS-DPD method, even with a smaller grid count. This versatility in precision and efficiency is leveraged by employing both DNS-DPD and LES-DPD methods complementarily.
- With an increase in numerical Den , there's a corresponding improvement in DR . Simultaneously, mean velocity, RMS velocity fluctuations, and Reynolds shear stress demonstrate consistent trends.
- The model demonstrates suitability across various Reynolds numbers. The buffer layer thickens with the addition of DPD polymer and maintains its thickness across different Re_τ , ensuring constant DR
- The process of DR shows a shift in high energy dissipation, transitioning from dispersion to concentration.
- When comparing polymer region heights of $\frac{1}{2}\delta$ and δ , their mean streamwise velocity profile and DR exhibit close similarities. Notably, the case with a $\frac{1}{2}\delta$ height demonstrates the highest DR efficiency when evaluating the ratio of DR to the polymer region's height. Simultaneously, near the wall, the vortex diminishes and gradually reappears toward the region without polymer. This suggests the localized control and reduction of velocity fluctuations by DPD particles in both wall-normal and spanwise directions.

6.2 Recommended future work

- For the future studies of FPED, enhancing the IBM-based computational model through the integration of two-way coupling techniques is recommended to optimize FPED performance. Further exploration of multiple factors encompassing various wave directions is essential to identify conditions that yield maximum voltage output across diverse wave conditions. Subsequently, with the investigation's outcomes, a suitable control model can be proposed to enhance power generation by facilitating real-time device adjustments. A comprehensive feasibility study during at least a year is imperative to evaluate its efficacy as an ocean environmental monitoring device, assess safety levels, establish warning signal mechanisms, and ascertain its contribution to energy supply.
- The future studies of HSO-TENG needs to conduct real-sea area tests for the HSO-TENG to further validate the numerical model's accuracy. Additionally, the estimation of electric power, based on both experimental and numerical results, will be further refined and developed to enhance accuracy and reliability.
- For the future studies of DNS/LES-DPD method, In forthcoming research, the focus should persist on high-Reynolds number DR investigations while considering computational resource constraints. Planned experimental studies

aim to evaluate the efficacy of polymer coatings on rough-surfaced plates in reducing drag as we deeply explore refining *DR* techniques. The objective is to furnish valuable insights for devising more efficient *DR* strategies and optimizing polymer applications within practical engineering systems.

- Based on the DNS/LES-DPD method, the specific relationship between polymer coating distribution, turbulence field, and PENG/TENG power generation performance will be explored.

Bibliography

- Abe, Hiroyuki, Hiroshi Kawamura, and Yuichi Matsuo (2001). "Direct numerical simulation of a fully developed turbulent channel flow with respect to the Reynolds number dependence". In: *J. Fluids Eng.* 123.2, pp. 382–393.
- Ahmadzadehtalatapeh, Mohammad and Majid Mousavi (2015). "A review on the drag reduction methods of the ship hulls for improving the hydrodynamic performance". In: *International Journal of Maritime Technology* 4, pp. 51–64.
- Ahmed, Najma, Noor Muhammad, and FD Zaman (2022). "CFD-based simulation of heat transfer in a rectangular channel". In: *International Journal of Modern Physics B*, p. 2350133.
- Altaf, Alaman, Ashraf A Omar, and Waqar Asrar (2014). "Review of passive drag reduction techniques for bluff road vehicles". In: *IIUM Engineering Journal* 15.1.
- Andres, Adrian de et al. (2017). "Beyond LCOE: A study of ocean energy technology development and deployment attractiveness". In: *Sustainable Energy Technologies and Assessments* 19, pp. 1–16.
- Antonia, RA et al. (1992). "Low-Reynolds-number effects in a fully developed turbulent channel flow". In: *Journal of Fluid mechanics* 236, pp. 579–605.
- Awan, Ahmad Bilal and Zeeshan Ali Khan (2014). "Recent progress in renewable energy—Remedy of energy crisis in Pakistan". In: *Renewable and Sustainable Energy Reviews* 33, pp. 236–253.
- Baghbani Kordmahale, Sina et al. (2021). "A hybrid structure of piezoelectric fibers and soft materials as a smart floatable open-water wave energy converter". In: *Micromachines* 12.10, p. 1269.
- Banks, R and M Zaharia (2020). "Characterization of the costs and benefits related to lost and/or abandoned Fish Aggregating Devices in the Western and Central Pacific Ocean". In: *Report produced by Poseidon Aquatic Resources Management Ltd for The Pew Charitable Trusts*.
- Benzi, Roberto and Emily S.C. Ching (2018). "Polymers in Fluid Flows". In: *Annual Review of Condensed Matter Physics* 9.1, pp. 163–181. DOI: 10 . 1146 / annurev - conmatphys - 033117 - 053913.
- Bergsma, Erwin WJ et al. (2022). "Wave variability along the world's continental shelves and coasts: Monitoring opportunities from satellite Earth observation". In: *Advances in Space Research* 69.9, pp. 3236–3244.
- BERMAN, NEIL S (1986). "Velocity fluctuations in non-homogeneous drag reduction". In: *Chemical Engineering Communications* 42.1-3, pp. 37–51.
- Bernardini, Matteo, Sergio Pirozzoli, and Paolo Orlandi (2014). "Velocity statistics in turbulent channel flow up to". In: *Journal of Fluid Mechanics* 742, pp. 171–191.
- Bird, Robert Byron et al. (1987). *Dynamics of polymeric liquids, volume 2: Kinetic theory*. Wiley.
- Birol, F (2017). "International Energy Agency". In: *Key World Energy statistics*.
- Browser, Energy Statistics Data (2022). IEA, Paris.
- Cao, Chuanchuan et al. (2022). "Spatiotemporal variability and climate teleconnections of global ocean wave power". In: *Frontiers in Marine Science* 9, p. 900950.

- Cao, Hao et al. (2021). "A hybrid wind and rainwater energy harvesting system for applications in sea-crossing bridges". In: *Ocean Engineering* 234, p. 109267.
- Cao, Hao et al. (2023). "A hybrid self-powered system based on wind energy harvesting for low-power sensors on canyon bridges". In: *International Journal of Precision Engineering and Manufacturing-Green Technology* 10.1, pp. 167–192.
- Chen, Shao-En et al. (2021). "A piezoelectric wave energy harvester using plucking-driven and frequency up-conversion mechanism". In: *Energies* 14.24, p. 8441.
- Cheng, Ping et al. (2019). "Largely enhanced triboelectric nanogenerator for efficient harvesting of water wave energy by soft contacted structure". In: *Nano Energy* 57, pp. 432–439.
- Conti, John et al. (2016). *International energy outlook 2016 with projections to 2040*. Tech. rep. USDOE Energy Information Administration (EIA), Washington, DC (United States . . .
- Coyle, Eugene D and Richard A Simmons (2014). *Understanding the global energy crisis*. Purdue University Press.
- Dallas, Vassilios, J Christos Vassilicos, and Geoffrey F Hewitt (2010). "Strong polymer-turbulence interactions in viscoelastic turbulent channel flow". In: *Physical Review E* 82.6, p. 066303.
- Davies, Tim K, Chris C Mees, and EJ Milner-Gulland (2014). "The past, present and future use of drifting fish aggregating devices (FADs) in the Indian Ocean". In: *Marine policy* 45, pp. 163–170.
- de Leeuw, Lawrence W. et al. (2022). "Modulating pipe-soil interface friction to influence HPHT offshore pipeline buckling". In: *Ocean Engineering* 266, p. 112713. ISSN: 0029-8018. DOI: <https://doi.org/10.1016/j.oceaneng.2022.112713>. URL: <https://www.sciencedirect.com/science/article/pii/S0029801822019965>.
- Del Alamo, Juan C et al. (2004). "Scaling of the energy spectra of turbulent channels". In: *Journal of Fluid Mechanics* 500, pp. 135–144.
- Domínguez, Jose M et al. (2022). "DualSPHysics: from fluid dynamics to multi-physics problems". In: *Computational Particle Mechanics* 9.5, pp. 867–895.
- Du, Peng et al. (2017). "Maintenance of air layer and drag reduction on superhydrophobic surface". In: *Ocean Engineering* 130, pp. 328–335.
- Endo, Takahide, Nobuhide Kasagi, and Yuji Suzuki (2000). "Feedback control of wall turbulence with wall deformation". In: *International journal of heat and fluid flow* 21.5, pp. 568–575.
- Escudier, MP, AK Nickson, and RJ Poole (2009). "Turbulent flow of viscoelastic shear-thinning liquids through a rectangular duct: Quantification of turbulence anisotropy". In: *Journal of non-newtonian fluid mechanics* 160.1, pp. 2–10.
- Espanol, Pep and Patrick B Warren (2017). "Perspective: Dissipative particle dynamics". In: *The Journal of chemical physics* 146.15, p. 150901.
- Farghali, Mohamed et al. (2023). "Strategies to save energy in the context of the energy crisis: a review". In: *Environmental Chemistry Letters*, pp. 1–37.
- Fazelianov, EM (2022). "The Energy Crisis in Europe and Russian Gas Supplies". In: *Herald of the Russian Academy of Sciences* 92.Suppl 9, S902–S907.
- Gârdan, Iuliana Petronela et al. (2023). "Consumers' attitude towards renewable energy in the context of the energy crisis". In: *Energies* 16.2, p. 676.
- Golshan, Roozbeh et al. (2015). "Large-eddy simulation with near-wall modeling using weakly enforced no-slip boundary conditions". In: *Computers & Fluids* 118, pp. 172–181.
- Goushcha, O et al. (2015). "Energy harvesting prospects in turbulent boundary layers by using piezoelectric transduction". In: *Journal of Fluids and Structures* 54, pp. 823–847.

- Gu, Yunqing et al. (2014). "Experimental and numerical investigation on drag reduction of non-smooth bionic jet surface". In: *Ocean Engineering* 81, pp. 50–57. ISSN: 0029-8018. DOI: <https://doi.org/10.1016/j.oceaneng.2014.02.015>. URL: <https://www.sciencedirect.com/science/article/pii/S0029801814000535>.
- Hoogerbrugge, PJ and JMVA Koelman (1992). "Simulating microscopic hydrodynamic phenomena with dissipative particle dynamics". In: *EPL (Europhysics Letters)* 19.3, p. 155.
- Hoyas, Sergio and Javier Jiménez (2006). "Scaling of the velocity fluctuations in turbulent channels up to $Re \tau = 2003$ ". In: *Physics of fluids* 18.1, p. 011702.
- Hoyer, K and A Gyr (1996). "Turbulent velocity field in heterogeneously drag reduced pipe flow". In: *Journal of non-newtonian fluid mechanics* 65.2-3, pp. 221–240.
- Hu, Zhiwei W, Christopher L Morfey, and Neil D Sandham (2006). "Wall pressure and shear stress spectra from direct simulations of channel flow". In: *AIAA journal* 44.7, pp. 1541–1549.
- Huang, Cenling et al. (2022). "Origami dynamics based soft piezoelectric energy harvester for machine learning assisted self-powered gait biometric identification". In: *Energy Conversion and Management* 263, p. 115720.
- Imzilen, Taha et al. (2019). "Fish aggregating devices drift like oceanographic drifters in the near-surface currents of the Atlantic and Indian Oceans". In: *Progress in oceanography* 171, pp. 108–127.
- Iwamoto, Kaoru, Yuji Suzuki, and Nobuhide Kasagi (2002). "Reynolds number effect on wall turbulence: toward effective feedback control". In: *International journal of heat and fluid flow* 23.5, pp. 678–689.
- J. Carlton, J. Aldwinkle and J. Anderson (2013). "FUTURE SHIP POWERING OPTIONS: Exploring Alternative Methods of Ship Propulsion". In: *Royal Academy of Engineering*. URL: https://raeng.org.uk/media/klonlmyx/future_ship_powering_options_report.pdf.
- Jiao, Pengcheng et al. (2022). "Magnetically circular layers triboelectric nanogenerators (MCL-TENG) for velocity sensing and damage detection". In: *Sustainable Energy Technologies and Assessments* 53, p. 102644.
- Kanehira, Taiga et al. (2020). "Numerical re-creation of multi-directional waves in a circular basin using a particle based method". In: *Ocean Engineering* 209, p. 107446.
- Kim, John, Parviz Moin, and Robert Moser (1987). "Turbulence statistics in fully developed channel flow at low Reynolds number". In: *Journal of fluid mechanics* 177, pp. 133–166.
- Koelman, JMVA and PJ Hoogerbrugge (1993). "Dynamic simulations of hard-sphere suspensions under steady shear". In: *EPL (Europhysics Letters)* 21.3, p. 363.
- Kuang, Yonghong et al. (2016). "A review of renewable energy utilization in islands". In: *Renewable and Sustainable Energy Reviews* 59, pp. 504–513.
- Lai, Jung-Pin et al. (2020). "A survey of machine learning models in renewable energy predictions". In: *Applied Sciences* 10.17, p. 5975.
- Lee, Changhoon, John Kim, and Haecheon Choi (1998). "Suboptimal control of turbulent channel flow for drag reduction". In: *Journal of Fluid Mechanics* 358, pp. 245–258.
- Lee, Keun H et al. (2001). "Application of reduced-order controller to turbulent flows for drag reduction". In: *Physics of Fluids* 13.5, pp. 1321–1330.
- Lee, Myoungkyu and Robert D Moser (2015). "Direct numerical simulation of turbulent channel flow up to". In: *Journal of fluid mechanics* 774, pp. 395–415.
- Liang, Xi et al. (2021). "Spherical triboelectric nanogenerator based on spring-assisted swing structure for effective water wave energy harvesting". In: *Nano Energy* 83, p. 105836.

- Liu, Liqiang et al. (2021). "Nodding duck structure multi-track directional freestanding triboelectric nanogenerator toward low-frequency ocean wave energy harvesting". In: *ACS nano* 15.6, pp. 9412–9421.
- Liu, MB et al. (2015). "Dissipative particle dynamics (DPD): an overview and recent developments". In: *Archives of Computational Methods in Engineering* 22.4, pp. 529–556.
- Liu, Renwen et al. (2023). "A review of collecting ocean wave energy based on piezoelectric energy harvester". In: *Sustainable Energy Technologies and Assessments* 59, p. 103417.
- Lozano-Durán, Adrián and Javier Jiménez (2014). "Effect of the computational domain on direct simulations of turbulent channels up to $Re \tau = 4200$ ". In: *Physics of Fluids* 26.1, p. 011702.
- Lu, Dengjun et al. (2023). "Wearable triboelectric visual sensors for tactile perception". In: *Advanced Materials* 35.7, p. 2209117.
- Mawignon, Fagla Jules et al. (2023). "The optimization of biomimetic sharkskin riblet for the adaptation of drag reduction". In: *Ocean Engineering* 275, p. 114135.
- McGranahan, Gordon, Deborah Balk, and Bridget Anderson (2007). "The rising tide: assessing the risks of climate change and human settlements in low elevation coastal zones". In: *Environment and urbanization* 19.1, pp. 17–37.
- Moeendarbary, E, TY Ng, and M Zangeneh (2010). "Dissipative particle dynamics in soft matter and polymeric applications—A review". In: *International Journal of Applied Mechanics* 2.01, pp. 161–190.
- Morison, JR, Joseph W Johnson, and Samuel A Schaaf (1950). "The force exerted by surface waves on piles". In: *Journal of Petroleum Technology* 2.05, pp. 149–154.
- Moser, Robert D, John Kim, and Nagi N Mansour (1999). "Direct numerical simulation of turbulent channel flow up to $Re \tau = 590$ ". In: *Physics of fluids* 11.4, pp. 943–945.
- Motozawa, Masaaki et al. (2010). "Turbulent Drag Reduction by Polymer Containing Paint: Simultaneous Measurement of Skin Friction and Release Rate". In: *International Heat Transfer Conference*. Vol. 49378, pp. 787–795.
- Muhammad, Noor, Maha MA Lashin, and Soliman Alkhatib (2022). "Simulation of turbulence flow in OpenFOAM using the large eddy simulation model". In: *Proceedings of the Institution of Mechanical Engineers, Part E: Journal of Process Mechanical Engineering* 236.5, pp. 2252–2265.
- Muhammad, Noor, Saif Ullah, and Umair Khan (2022). "Energy recovery mechanism of air injection in higher methane cut reservoir". In: *International Journal of Modern Physics B* 36.24, p. 2250153.
- Muhammad, Noor, FD Zaman, and MT Mustafa (2022). "OpenFOAM for computational combustion dynamics". In: *The European Physical Journal Special Topics* 231.13, pp. 2821–2835.
- Muhammad, Noor et al. (2022). "The shortfall and rise in energy deposition and combustion via OpenFOAM". In: *Case Studies in Thermal Engineering* 40, p. 102563.
- MUNEKATA Co., Ltd. (2019a). "Japanese patent number 2013-188667." In.
- (2019b). "Japanese patent number 4868475." In.
- Mutsuda, Hidemi et al. (2017a). "A painting type of flexible piezoelectric device for ocean energy harvesting". In: *Applied Ocean Research* 68, pp. 182–193.
- Mutsuda, Hidemi et al. (2017b). "Harvesting flow-induced vibration using a highly flexible piezoelectric energy device". In: *Applied Ocean Research* 68, pp. 39–52.
- Nabavi, Seyedeh Fatemeh et al. (2019). "An ocean wave-based piezoelectric energy harvesting system using breaking wave force". In: *International Journal of Mechanical Sciences* 151, pp. 498–507.

- Nef, John U (1977). "An early energy crisis and its consequences". In: *Scientific American* 237.5, pp. 140–151.
- Neumann, Barbara et al. (2015). "Future coastal population growth and exposure to sea-level rise and coastal flooding-a global assessment". In: *PloS one* 10.3, e0118571.
- Omer, Abdeen Mustafa (2012). "The energy crisis, the role of renewable and global warming". In: *Greener Journal of Environment Management and Public Safety* 1.1, pp. 038–07.
- Ozili, Peterson K and Ercan Ozen (2023). "Global energy crisis: impact on the global economy". In: *The Impact of Climate Change and Sustainability Standards on the Insurance Market*, pp. 439–454.
- Pang, Yafeng et al. (2022). "Waterbomb-origami inspired triboelectric nanogenerator for smart pavement-integrated traffic monitoring". In: *Nano Research* 15.6, pp. 5450–5460.
- Patel, R, S McWilliam, and AA Popov (2014). "Optimization of piezoelectric cantilever energy harvesters including non-linear effects". In: *Smart Materials and Structures* 23.8, p. 085002.
- Peskin, Charles S (2002). "The immersed boundary method". In: *Acta numerica* 11, pp. 479–517.
- Pietrosemoli, Licia and Carlos Rodriguez-Monroy (2019). "The Venezuelan energy crisis: Renewable energies in the transition towards sustainability". In: *Renewable and Sustainable Energy Reviews* 105, pp. 415–426.
- Pimentel, David et al. (1973). "Food production and the energy crisis". In: *Science* 182.4111, pp. 443–449.
- Plaza Bonilla, Daniel et al. (2019). "No-tillage systems linked to reduced soil N₂O emissions in Mediterranean agroecosystems". In: *Science for Environment Policy*, 2019, vol. 519.
- Ptasinski, PK et al. (2001). "Experiments in turbulent pipe flow with polymer additives at maximum drag reduction". In: *Flow, Turbulence and Combustion* 66.2, pp. 159–182.
- Qi, Lingfei et al. (2021). "A hybrid piezoelectric-electromagnetic wave energy harvester based on capsule structure for self-powered applications in sea-crossing bridges". In: *Renewable Energy* 178, pp. 1223–1235.
- Ramos, Ana and Abel Rouboa (2022). "Life cycle thinking of plasma gasification as a waste-to-energy tool: Review on environmental, economic and social aspects". In: *Renewable and Sustainable Energy Reviews* 153, p. 111762.
- Reguero, Borja G, Iñigo J Losada, and Fernando J Méndez (2019). "A recent increase in global wave power as a consequence of oceanic warming". In: *Nature communications* 10.1, p. 205.
- Richardson, Harry Ward (1975). "Economic aspects of the energy crisis". In: G. Moreno, L. Dagorn, M. Capello, J. Lopez, J. Filmalter, F. Forget, I. Sancristobal, K. Holland (2016). "Fish aggregating devices (FADs) as scientific platforms". In: *Fisheries Research* 178, pp. 122–129. DOI: 10.1016/j.fishres.2015.09.021.
- Y. Baidai, L. Dagorn, M. J. Amade, D. Gaertner, M. Capello (2020). "Machine learning for characterizing tropical tuna aggregations under Drifting Fish Aggregating Devices (DFADs) from commercial echosound buoys data". In: *Fisheries Research* 229, p. 105613. DOI: 10.1016/j.fishres.2020.105613.
- Rowin, Wagih Abu et al. (2021). "A novel approach for drag reduction using polymer coating". In: *Ocean Engineering* 240, p. 109895.
- Rutledge, Jeffrey and Charles A Sleicher (1993). "Direct simulation of turbulent flow and heat transfer in a channel. Part I: smooth walls". In: *International journal for numerical methods in fluids* 16.12, pp. 1051–1078.

- Satoh, Akira (2014). "Introduction to molecular simulation with sample simulation programs". In.
- Semenov, BN (1991). "The pulseless injection of polymeric additives into near-wall flow and perspectives of drag reduction". In: *Recent Developments in Turbulence Management*. Springer, pp. 293–308.
- Smagorinsky, Joseph (1963). "General circulation experiments with the primitive equations: I. The basic experiment". In: *Monthly weather review* 91.3, pp. 99–164.
- Small, Christopher and Robert J Nicholls (2003). "A global analysis of human settlement in coastal zones". In: *Journal of coastal research*, pp. 584–599.
- Soleimani, Kaveh, Mohammad Javad Ketabdari, and Farzan Khorasani (2015). "Feasibility study on tidal and wave energy conversion in Iranian seas". In: *Sustainable Energy Technologies and Assessments* 11, pp. 77–86.
- Song, Changhui et al. (2022). "Recent advances in ocean energy harvesting based on triboelectric nanogenerators". In: *Sustainable Energy Technologies and Assessments* 53, p. 102767.
- Spalart, Philippe R (1988). "Direct simulation of a turbulent boundary layer up to $Re_\theta = 1410$ ". In: *Journal of fluid mechanics* 187, pp. 61–98.
- Sthel, Marcelo S, José GR Tostes, and Juliana R Tavares (2013). "Current energy crisis and its economic and environmental consequences: Intense human cooperation". In.
- Sureshkumar, R, Antony N Beris, and Robert A Handler (1997). "Direct numerical simulation of the turbulent channel flow of a polymer solution". In: *Physics of Fluids* 9.3, pp. 743–755.
- Takahashi, Chiyo et al. (2019). "A Comparison of Remotely Operated Vehicle (ROV) and Time Lapse Camera Techniques for Investigating Fish Fauna Around an Anchored Fish Aggregating Device (aFAD)". In: *Journal of Fisheries Engineering* 56.2, pp. 75–83.
- Tamano, Shinji et al. (2007). "Direct numerical simulation of the drag-reducing turbulent boundary layer of viscoelastic fluid". In: *Physics of Fluids* 19.7, p. 075106.
- Tanahashi, M et al. (2004). "Scaling law of fine scale eddies in turbulent channel flows up to $Re_\tau = 800$ ". In: *International Journal of Heat and Fluid Flow* 25.3, pp. 331–340.
- Tao, Kai et al. (2020a). "Miura-origami-inspired electret/triboelectric power generator for wearable energy harvesting with water-proof capability". In: *Microsystems & Nanoengineering* 6.1, p. 56.
- Tao, Kai et al. (2020b). "Origami-inspired electret-based triboelectric generator for biomechanical and ocean wave energy harvesting". In: *Nano Energy* 67, p. 104197.
- Tiederman, William G, Thomas S Luchik, and DG Bogard (1985). "Wall-layer structure and drag reduction". In: *Journal of Fluid Mechanics* 156, pp. 419–437.
- Toms, Be A (1949). "Some observations on the flow of linear polymer solutions through straight tubes at large Reynolds numbers". In: *Proc. First Int. Conger. on Rheology* 2, pp. 135–141.
- Torres-Irineo, Edgar et al. (2014). "Changes in fishing power and fishing strategies driven by new technologies: The case of tropical tuna purse seiners in the eastern Atlantic Ocean". In: *Fisheries Research* 155, pp. 10–19.
- Turner, Louis (1974). "The politics of the energy crisis". In: *International Affairs (Royal Institute of International Affairs 1944-)* 50.3, pp. 404–415.
- U.Epa (2020). "Sources of Greenhouse Gas Emissions". In: *U.S. Environ. Prot. Agency (2020)*. DOI: <https://www.epa.gov/ghgemissions/inventory-us-greenhouse-gas-emissions-and-sinks>.

- Von Homeyer, Ingmar, Sebastian Oberthür, and Claire Dupont (2022). "Implementing the European Green Deal during the evolving energy crisis". In: *JCMS-JOURNAL OF COMMON MARKET STUDIES* 60, pp. 125–136.
- Vuorinen, Ville and K Keskinen (2016). "DNSLab: A gateway to turbulent flow simulation in Matlab". In: *Computer Physics Communications* 203, pp. 278–289.
- Wang, Hanwen, Kaiying Wang, and Guohua Liu (2022). "Drag reduction by gas lubrication with bubbles". In: *Ocean Engineering* 258, p. 111833. ISSN: 0029-8018. DOI: <https://doi.org/10.1016/j.oceaneng.2022.111833>. URL: <https://www.sciencedirect.com/science/article/pii/S0029801822011763>.
- Wang, Huaizhi et al. (2019). "A review of deep learning for renewable energy forecasting". In: *Energy Conversion and Management* 198, p. 111799.
- Wang, Xiaoning et al. (2022). "A double-float structured triboelectric nanogenerator for wave hydrological monitoring". In: *Sustainable Energy Technologies and Assessments* 54, p. 102824.
- Wardhana, Ede Mehta et al. (2020). "Harvesting contact-separation-compression vibrations using a flexible and compressible triboelectric generator". In: *Sustainable Energy Technologies and Assessments* 42, p. 100869.
- Wardhana, Ede Mehta et al. (2022). "Characteristics of electric performance and key factors of a hybrid piezo/triboelectric generator for wave energy harvesting". In: *Sustainable Energy Technologies and Assessments* 50, p. 101757.
- White, Christopher M and M Godfrey Mungal (2008). "Mechanics and prediction of turbulent drag reduction with polymer additives". In: *Annu. Rev. Fluid Mech.* 40, pp. 235–256.
- Widyatmoko, Ahmad Catur, Britta Denise Hardesty, and Chris Wilcox (2021). "Detecting anchored fish aggregating devices (AFADs) and estimating use patterns from vessel tracking data in small-scale fisheries". In: *Scientific reports* 11.1, pp. 1–11.
- Xi, Li (2019). "Turbulent drag reduction by polymer additives: Fundamentals and recent advances". In: *Physics of Fluids* 31.12, p. 121302.
- Xia, Kequan et al. (2023). "A self-powered bridge health monitoring system driven by elastic origami triboelectric nanogenerator". In: *Nano Energy* 105, p. 107974.
- Xu, Guobao et al. (2019). "Internet of things in marine environment monitoring: A review". In: *Sensors* 19.7, p. 1711.
- Yang, Jeong Woo et al. (2014). "Development and performance at high Reynolds number of a skin-friction reducing marine paint using polymer additives". In: *Ocean Engineering* 84, pp. 183–193.
- Yasuda, Shugo and Ryoichi Yamamoto (2008). "A model for hybrid simulations of molecular dynamics and computational fluid dynamics". In: *Physics of Fluids* 20.11, p. 113101.
- Yoneda, Taiju, Daichi Matsumoto, and Hirofumi Wada (2019). "Structure, design, and mechanics of a paper spring". In: *Physical Review E* 100.1, p. 013003.
- Yu, Bo and Yasuo Kawaguchi (2004). "Direct numerical simulation of viscoelastic drag-reducing flow: a faithful finite difference method". In: *Journal of Non-Newtonian Fluid Mechanics* 116.2-3, pp. 431–466.
- Zhao, Daoli et al. (2021). "Hydrokinetic piezoelectric energy harvesting by wake induced vibration". In: *Energy* 220, p. 119722.
- Zhao, Xiaojie and Zhi Zong (2022). "Experimental and numerical studies on the air-injection drag reduction of the ship model". In: *Ocean Engineering* 251, p. 111032. ISSN: 0029-8018. DOI: <https://doi.org/10.1016/j.oceaneng.2022.111032>. URL: <https://www.sciencedirect.com/science/article/pii/S0029801822004528>.

-
- Zhao, Xue Jiao et al. (2018). "Highly adaptive solid–liquid interfacing triboelectric nanogenerator for harvesting diverse water wave energy". In: *ACS nano* 12.5, pp. 4280–4285.
- Zhu, Guang et al. (2014). "Harvesting water wave energy by asymmetric screening of electrostatic charges on a nanostructured hydrophobic thin-film surface". In: *ACS nano* 8.6, pp. 6031–6037.

Acknowledgements

At the end of the article, I would like to thank many people who have helped my research and life over the past few years.

Firstly, I would like to express my gratitude to my supervisor Prof. Hidemi MUTSUDA for affirming my efforts, cultivating my interest, and always pointing out my many mistakes in the most patient way. His great support on my research for five and half years gives me the opportunity to complete this doctor thesis. His careful guidance, rigorous and innovative scientific research style, high emotional intelligence communication skills, and the principle of gentle and warm reception of everyone no matter how tired he is will be what I will always learn from in my future career. I am also very grateful to Prof. Takuji NAKASHIMA for his great help in my research. He is always able to point out the problems in my research and give very helpful suggestions, which promotes my progress. His rigor and love for research inspire me.

Then, I want to thank all the classmates and friends I have met at Hiroshima University over the years. I want to thank the seniors who have left this laboratory (Yasuaki Doi sensei, Taiga KANEHIRA sensei, Eri HARADA san, ARUNI DINAN HANIFA san, Taichi YAMADA san, Takeshi KUBOTA san, Yuya Wasada san, Qingyu Wang san, Chao Yan san, Ede Mehta Wardhana san, Hao Cao san) for their great help and support. I want to thank the doctoral Course students (Andi Dian Eka ANGGRIANI, Akihiro NAKATA, Dimas Bahtera ESKAYUDHA, Muhammad Akbar ASIS), the M2 students (Masahiro NAMATAME, Hayato SAKAGUCHI, Kan ZHOU, Taishi NAKASHIMA, Sota NOBUKI, Chiharu HASEGAWA, Atsuhiro MAEDA, Motoki MIZUNARU, Oliver Sungcuan SANTOS, Feiyi CHEN), the M1 students (Yuto SUMIYA, Sota NAKAMURA, Zewei HAO, Kazuma BESSHO, Koki HOSOKAWA, Ryota MIZOGUCHI, Yusuke YAMASHITA, Haochen SHUANG), B4 students (Yushi HAKAMATA, Taizo OHISHI, Taichi OKAMOTO, Shogo NAKATA, Hikaru NISHIKOKURA, Shuta HIRAI, Shunki YAMAMOTO), and special research student Peng ZHENG for encouragement and support. I also want to thank my friends in this department (Shiling Song, Andi Nadia Himaya, Thin Thin Htut, Ryusuke Okuda) for their accompanying you from courses to research.

Next, I want to thank my parents for always supporting and believing in my choices. I would like to express my gratitude to my boyfriend for listening to my sharing about life and study all the time, and for being a witness to many moments in my life. I want to thank my little sister for giving me a new perspective from young people on the world. And thanks to my roommates during my undergraduate studies. Chatting with you every day online is like going back to those previous days and nights, which makes me never lonely.

Finally, I would like to thank the CSC scholarship for bringing me financial independence, which allows me to devote myself wholeheartedly to scientific research.

I wish me and everyone mentioned above all the best in their future lives and work.